

UNIVERSITY OF GENEVA

MASTER'S DEGREE IN PHYSICS

**Thesis**

---

**Time resolution of a monolithic  
silicon pixel sensor prototype**

---

*Author:*

C. MILETO

*Supervisors:*

Prof. G . IACOBUCCI  
Prof. L . PAOLOZZI

9<sup>th</sup> June 2021

This dissertation is submitted for the degree of Master in Particle Physics.



**UNIVERSITÉ  
DE GENÈVE**

---

**FACULTÉ DES SCIENCES**  
Section de physique

# Contents

<b>1</b>	<b>Introduction</b>	<b>1</b>
<b>2</b>	<b>Interactions of charged particles with matter</b>	<b>2</b>
2.1	Examples of interactions . . . . .	2
2.2	Energy loss per unit distance: the Bethe formula . . . . .	3
2.3	Behaviour of the Bethe formula versus velocity . . . . .	4
2.4	The energy loss for electrons . . . . .	5
2.5	Stopping power in different materials . . . . .	6
<b>3</b>	<b>Radioactive sources used and their decay modes</b>	<b>8</b>
3.1	Source $^{109}\text{Cd}$ and electron capture . . . . .	8
3.2	Source $^{90}\text{Sr}$ and Beta decay . . . . .	9
<b>4</b>	<b>History of detectors for ionizing radiation</b>	<b>13</b>
4.1	Cloud chambers . . . . .	13
4.2	Bubble chambers . . . . .	14
4.3	Drift chambers . . . . .	15
4.4	Semiconductor detectors . . . . .	17
4.5	Some industrial pixels applications . . . . .	19
<b>5</b>	<b>Semiconductors</b>	<b>21</b>
5.1	Why choose Silicon ? . . . . .	21
5.2	Semiconductors Theory . . . . .	21
5.3	Band structure . . . . .	22
5.4	Silicon doping . . . . .	23
5.5	PN-junction . . . . .	25
5.5.1	PN-junction in thermal equilibrium . . . . .	26
5.5.2	PN-junction with external current . . . . .	27
5.6	Particle detection with semiconductors . . . . .	28
5.6.1	Shockley-Ramo theorem . . . . .	29
<b>6</b>	<b>Electronics</b>	<b>32</b>
6.1	Diode . . . . .	32
6.2	Bipolar Junction Transistor . . . . .	33
6.3	The current gain $\beta$ . . . . .	36
6.4	Noise sources . . . . .	38
6.4.1	The thermal noise . . . . .	38
6.4.2	The shot noise . . . . .	39
6.4.3	Flicker Noise . . . . .	39
6.5	Noise Characteristics and Equivalent noise charge . . . . .	39
6.6	Heterojunction bipolar transistor - SiGe . . . . .	41
6.6.1	Crystalline structure and bandgap of SiGe . . . . .	41



6.6.2	Energy Bands in HBT-SiGe . . . . .	43
<b>7</b>	<b>The prototype (ATTRACT project)</b>	<b>46</b>
7.1	Characteristic form of the chip . . . . .	47
7.2	Stabilisation of a transistor by reaction of the collector . . . . .	50
7.3	The amplifier . . . . .	52
7.4	Capacitors . . . . .	53
7.5	Drivers . . . . .	54
7.6	Assembly . . . . .	55
<b>8</b>	<b>Experimental setup</b>	<b>57</b>
8.1	Unige GPIO . . . . .	58
8.2	DAC settings . . . . .	59
8.3	Lecroy oscilloscope . . . . .	60
8.3.1	The potential resolution . . . . .	60
8.3.2	The time resolution - sampling . . . . .	61
8.4	The LGAD . . . . .	63
<b>9</b>	<b>Signal processing for precise timing measurement</b>	<b>65</b>
9.1	Signal characteristics . . . . .	65
9.2	Time-Walk and jitter . . . . .	66
9.3	Resolution of a detector . . . . .	67
<b>10</b>	<b>Analysis method</b>	<b>68</b>
10.1	Binary conversion . . . . .	68
10.2	Pre-analysis . . . . .	69
10.3	Events selection . . . . .	71
10.4	Time-Walk correction . . . . .	73
<b>11</b>	<b>Results</b>	<b>75</b>
11.1	Results for the events selection . . . . .	75
11.2	Results for the pre-analysis . . . . .	76
11.2.1	Working points chosen . . . . .	80
11.3	TOF - Time resolution measurement . . . . .	81
<b>12</b>	<b>Conclusion and Outlook</b>	<b>86</b>
<b>13</b>	<b>Acknowledgements</b>	<b>88</b>
<b>14</b>	<b>Annexes</b>	<b>94</b>
14.1	Oscillation effect results . . . . .	94
14.2	TOF Results - $I_{Preamp} = 7$ DAC . . . . .	96
14.3	TOF Results - $I_{Preamp} = 150$ DAC . . . . .	97

# Chapter 1

## Introduction

When we observe the night sky, what do we see? First of all, we see the impressive black nothingness with which we perpetually cohabit. Stars and planets can be seen shining due to their reflection of the Sun's rays and for some fortunate people, they may even see galaxies. In reality, few people realize that they have the result of the Universe's entire history in front of their eyes. The most curious will wonder to themselves about its origin, its destiny, what it is made of, the reasons for its creation, how it holds together or even about its size. Whether they are, the Church in the Middle Ages, philosophers, scientists or physicists of today, they have all tried to find personal answers to these questions which, thanks to science, have evolved over time with the aim of finding the laws of nature.

Nowadays, several research centres have emerged. One of the most famous is, without doubt, the *centre europeen de recherche nucleaire* (CERN). With its Large Hadron Collider (LHC), CERN collides highly energetic proton bunches to test and study in details the Standard Model predictions for elementary particles and their interactions. This led, in July 2012, to the discovery of the Higgs boson whose elementary particles pull their masses in its associated field [1]. Several questions about and beyond the Standard Model remain open as the hierarchy of the four fundamental forces or astronomical observations such as the dark matter via exotic scenarios such as WIMPs, Susy, etc... [2]. However, all the discoveries made in particle physics could not have happened without the parallel development of accelerators and particle detectors.

In this thesis, a new generation of monolithic pixels detectors (called the ATTRACT prototype) will be studied and its temporal resolution will be measured. The document is divided into three parts: - The first part will be a theoretical approach flying over the concepts of particle's interactions with matter (Chapter 2) as well as the decay modes of the sources used (Chapter 3). It continues with an historical approach to the operation of the main detectors that have made CERN famous and leads to the actual tracking technology based on Silicon Pixel detectors (Chapter 4). - The second part will be largely devoted to pixel detectors and more specifically, on the ATTRACT prototype. The physical concepts of semiconductors (Chapter 5), as well as basic electronic components such as transistors (Chapter 6) , will be explained in order to understand the operation of the ATTRACT prototype (Chapter 7). - The third part is more experimental, with a description of the experimental set-up used for data acquisition (Chapter 8) followed by the signal processing (Chapter 9) and the analysis method used (Chapter 10) . It will conclude with a presentation of the results obtained in terms of time resolution with the prototype studied (Chapter 11).

# Chapter 2

## Interactions of charged particles with matter

The interactions of particles with matter is the basis of particle detection and the fundamental process to study particles in physics. The interaction process depends on the incoming particle and the type of matter in which it is moving through. The particles will interact with it by losing its energy in various ways. Some examples are [3]:

- In solids, liquids and gases, the charged particle will ionize the atoms of the material.
- In semiconductors, the charged particle will produce some electrons and holes pairs.
- In scintillator, the charged particle will lead to a light production.
- In superheated liquid: the charged particle will leave a trail of bubbles.

For a high-energy photon ( $\gamma$  radiation), three processes take place. At energy lower than  $E_\gamma \leq 0.1$  MeV, the photoelectric effect is dominant. At a range of  $0.1 \leq E_\gamma \leq 10$  MeV, it is the Compton scattering effect while the pair production effect starts at energy  $E_\gamma > 1.022$  MeV and will be dominant only over a range of  $E_\gamma \geq 10$  MeV. However, the interaction of charged particles involve other processes. At low energy, the ionisation effect and excitation of the matter are the main contributors to energy loss while the Bremsstrahlung effect takes over only at very high energy and is, for example, the main process for electrons above 100 MeV.

### 2.1 Examples of interactions

The simplest examples of particles interactions with matter are shown in Figure 2.1. From the left to the right, the ionisation process, the pair production and the Compton scattering processes. The first row illustrates each mode of interaction with a Feynman diagram and the second with a subatomic representation. Depending on the energy, the charge and the type (lepton, hadron or photon) of the incoming particle as well as the type of the target material, one or more types of interactions will be dominant. At low energy, interactions with the orbital electrons of the matter will be favoured (excitation and ionisation processes). At high energy, deep interactions with the nuclei become important. Most tracking detectors use ionisation of its atoms caused by the passage of the charged particle to track them. Some examples would be charged leptons, photons and hadrons such as  $e^-$ ,  $\mu$ ,  $\gamma$ ,  $\pi$ , K, p, n .... The electrons and holes produced by ionisation can then be collected to obtain some information on the particle such as its position or its deposition energy. The next section goes deeper in the understanding of photons and electrons interactions with matter.

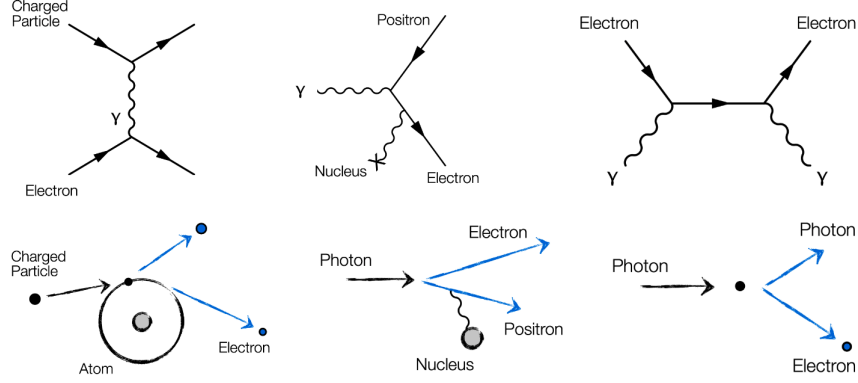


FIGURE 2.1 – Representation of particles interactions with matter. From the left to right: by ionization, pair production and Compton scattering [4]. Ionization is the process used to track particles by collecting electrons and holes that are generated by the particle's energy loss passing through the matter.

## 2.2 Energy loss per unit distance: the Bethe formula

When passing inside an absorbing matter, charged particles will deposit a part of their energy by interacting via many scattering process with matter's electrons. Figure 2.2 shows the most famous representation of heavy and charged particles (as the muon) energy deposit in matter (e.g. average energy lost per unit of length  $\langle \frac{dE}{dx} \rangle$ ). In this range of interactions <sup>[a]</sup>, electromagnetic (EM) interactions are the main interactions for particles with the orbital electrons of the matter and it refers to the electric and magnetic field which behave as  $\frac{1}{r^2}$  <sup>[b]</sup>. A circular expansion of  $\vec{E}$  and  $\vec{B}$  around the travelling particle is generated leading to many collisions and resulting on a loss of its initial amount of energy. The general Equation 2.1 shown in Figure 2.2 is called the *Bethe-Block Equation* <sup>[c]</sup> [5].

$$\langle \frac{dE}{dx} \rangle = -Kz^2 \frac{Z}{A} \frac{1}{\beta^2} \left[ \frac{1}{2} \ln \left( \frac{2m_e c^2 \beta^2 \gamma^2 T_{max}}{I^2} \right) - \beta^2 - \frac{\delta(\beta\gamma)}{2} \right] \quad (2.1)$$

$\langle \frac{dE}{dx} \rangle$  has units of  $\frac{eV}{g/cm^2}$ .  $K$  is a constant equal to  $4\pi N_A r_e^2 m_e c^2 = 0.307075 \text{ MeV cm}^2$  and  $z$  represents the charge of the incoming particle in units of the electron charge.  $Z$  is the atomic number and  $A$  is the atomic mass of the absorbing matter. For silicon,  $Z$  is equal to 14 and  $A$  to 28.  $m_e c^2$  represents the rest energy of the electron which is equal to 0.511 MeV.  $\beta$  is the velocity of the incoming particle in unit of speed of light where  $\beta = \frac{v}{c}$  and  $\gamma = \sqrt{1 - \beta^2}$  is the Lorentz factor.  $I$  is the excitation energy and is 137 eV for silicon. Finally,  $\delta$  is the correction for the charge density due to the polarisation of the material. This correction is necessary because the incoming particles polarize the atoms that are close to their trajectories and reduce the electric field on more distant electrons

<sup>[a]</sup> Here, only elastic collisions are assumed meaning that no interaction with the nucleus is considered and so only electromagnetic interactions are taken into account.

<sup>[b]</sup> EM field can be seen as an circular field expansion around the particle with a radius defined by  $r$ .

<sup>[c]</sup> For more information, the reader can refer to the Particles Data Group (PDG).

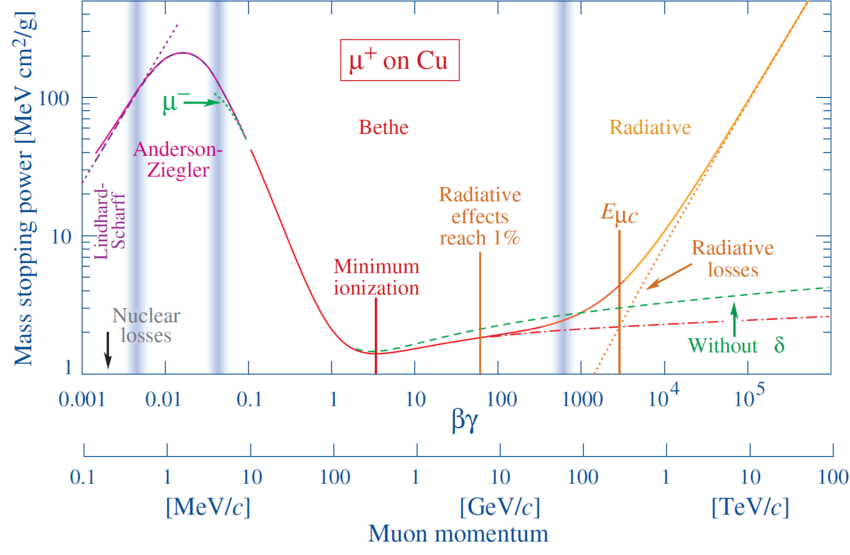


FIGURE 2.2 – Average of the mass stopping power  $\langle \frac{dE}{dx} \rangle$  for muons as a function of  $\beta\gamma = pMc$  in copper. The three processes involved in charged particles interactions with matter are represented. [6]

thus reducing the loss of energy.  $\delta > 0$  and increases with the matter density.  $T_{max}$  represents the maximal amount of energy transmitted to an electron during a collision. Equation 2.1 is simply the average energy loss (e.g. the stopping-power of a material), per distance and normalised by the density, for a particle as a function of  $\beta\gamma$ . This equation is used for speedy particles such as protons or alpha particles but not electrons. Even if their speed is sufficient, their mass is too light to be governed by the same equation. Equation 2.1 has to be slightly transformed for electrons, the next section will go into more details.

## 2.3 Behaviour of the Bethe formula versus velocity

Three main regimes can be distinguished. The first one,  $\beta\gamma < 3$ , is represented by a  $\frac{1}{v^2} \approx \frac{1}{\beta^2}$  dependence concerning *slow* velocity and *low* energetic particles. The second one is known as the minimum ionisation loss regime. The factor  $\gamma^2$  hidden in the logarithm term breaks the general decrease at a range of  $\beta\gamma \approx 3$ . The minimum value is called the *minimum ionizing particle (MIP)* and characterizes the minimum amount of energy required to ionise the matter. Most relativistic particles have mean energy loss rate close to it, they are MIPs. The last regime can be referred to a relativistic rise which is at  $\beta\gamma > 3$  and behaving as  $\sim 2\log(\beta)$  [7]. After the minimum ionisation loss  $\frac{dE}{dx}$ , Bethe formula predicts an indefinitely rise due to the radiative effects [3]. At this relativistic energy range, the transverse electromagnetic field of the particle increases meaning that more atoms of the material would be affected by its electromagnetic field. This leads to an higher ionisation energy loss. Nuclear interaction becomes not negligible. Above 1000, bremsstrahlung effect is dominant. Above  $\beta > 3$  some density correction has to be

taken into account. These density effects are due to the fact that long distance atomic electrons are excluded from the relativistic expansion of the electromagnetic field of the incident particle by a dielectric effect of the intervening atoms in the material [3]. So the curve of the Bethe formula rises less rapidly than as it was predicted by the Bethe formula without the density correction  $\delta$  (in Figure 2.1 the difference is shown with the red and green dashed lines but in any case they are logarithmic rise). They represent the influence of the correction terms. With a non-zero  $\delta$ , the increase is slower than without. At  $\beta\gamma > 1000$ , the Bremsstrahlung effect takes place. This phenomena of braking radiation concerns especially charged particles whose speed is close to the speed of light. For example, this effect is rare in the radioactivity range because of the low energised electrons of beta decays but it plays an important role in cosmic radiation and in the functioning of particle accelerators. When light and relativistic electrons enter deep in the nucleus it will start to feel the effects of its electromagnetic field ( via a nucleus field, or magnets in accelerators) and will therefore be slowed down and deflected by the Coulomb field. As Maxwell's equation shows, an electron or positron having an acceleration or deceleration will emit a photon which takes away part of its energy. As shown in Figure 2.1 left side, the electron has to brake and its trajectory changes. The first particles affected are the electrons and positrons due to their low masses.

## 2.4 The energy loss for electrons

The stopping power is different for electrons compared to heavily charged particles . The Bethe-Bloch formula does not apply correctly to electrons due to their low mass. The mass of an incident electron being the same as the one for an electron contained in an atom of matter, a single collision is sufficient to change its trajectory which then becomes sinuous <sup>[d]</sup> . In addition the Bremsstrahlung effect is not negligible for light particles. In this case, the energy lost is equal to  $\Delta E_{Brem} \simeq \frac{1}{\rho} \frac{E^4}{m^4}$  with  $\rho$  the radius of curvature,  $E$  the particle energy and  $m$  its mass. For high-energy particles this effect is not negligible [8]. High-energy electrons predominantly lose energy in matter via the Bremsstrahlung effect. The radiation length  $X_0 \frac{g}{cm^2}$  (given by Equation 2.2 [9]) represents the distance in which an high-energy electron loses all of its energy. Where  $Z$  is the atomic number and  $A$  is the mass number for a given material used:

$$X_0 = \frac{716.4 \frac{g}{cm^2} A}{Z(Z+1) \ln(\frac{287}{\sqrt{Z}})} \quad (2.2)$$

Figure 2.3 shows the energy loss per radiation length as a function of the incident electron energy in lead. The importance of the Bremsstrahlung effect is easily observable. The two ranges (below and above 7 MeV) are very distinct. For low energy ( $E_{e-} \leq 7$  MeV), the ionisation effect is taking over but varies logarithmically with the increase of the energy

---

<sup>[d]</sup> The term sinuous means that the trajectory is not a curved line but more sinusoidal and cyclic behaviour. An example of that kind of trajectory will be presented later with Figure 4.1

until higher values ( $7\text{MeV} \leq E_e$ ) where the Bremsstrahlung takes over at a rate nearly proportional to the energy.

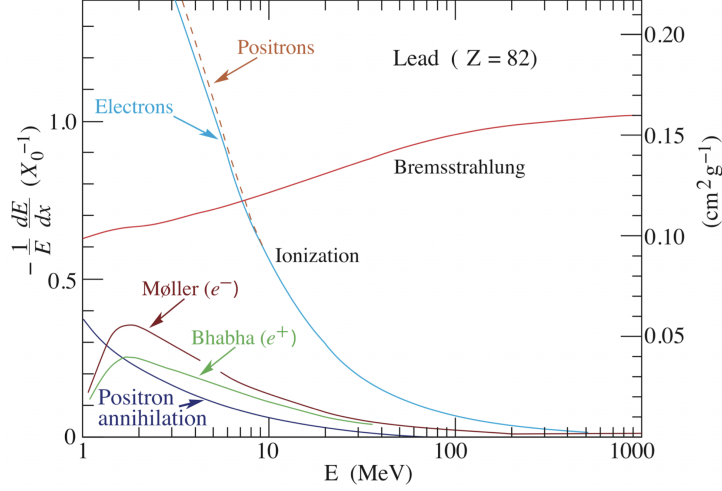


FIGURE 2.3 – Fractional energy loss per radiation length in lead as a function of electron or positron energy. Two regimes are highlighted, one below  $\approx 7$  MeV dominated by the ionization process and another above dominated by the Bremsstrahlung effect (source: PDG).

The Bethe-Bloch formula for electrons can finally be represented by Equation 2.3 [8]. Where  $\tau$  is the kinetic energy of the incident particle and  $F$  is a function differentiating electrons and positrons. The other variables have the same meaning as in Equation 2.1.

$$\left\langle \frac{dE}{dx} \right\rangle \frac{1}{X_0} = -K \frac{Z}{A} \frac{1}{\beta^2} \left[ \ln \left( \frac{m_e c^2 \tau^2 \sqrt{\tau + 1}}{\sqrt{2} I} \right) + \frac{F(\tau)}{2} - \frac{\delta}{2} \right] \quad (2.3)$$

## 2.5 Stopping power in different materials

The ionisation range of the Bethe equation is around  $0.1 \lesssim \beta\gamma \lesssim 1000$  (Figure 2.4 from the PDG) and interactions are dominated by elastic collision. It represents the mean energy loss for various particles in different materials. The higher curve is related to  $H_2$  liquid used in bubble chamber experiments, the curves below represent the  $He$  gas and successive elements such as carbon, aluminium, iron, tin and lead. Except for  $H_2$  liquid, the energy loss rate is very close in most of the materials. However, a small downward shift is observable due to the increasing  $Z$ . Figure 2.4 highlights the same minimum as Figure 2.1 at  $\beta\gamma = 3$ <sup>[e]</sup> which separates the two distinct ranges mentioned on the previous section.

Various materials can be used to brake particles (gas, liquids or solids). The main difference at high energy between a gas as  $H_2$  and other sorts of materials is due to the

<sup>[e]</sup> This value is taken from the x-axis of the graph representing  $\beta\gamma$  and not from the pulse range of the particles below the graph.

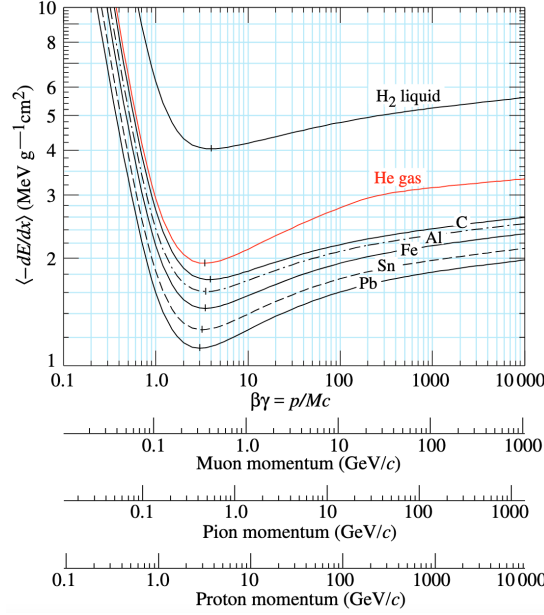


FIGURE 2.4 – Representation of the mean energy loss per unit of length divided by density in different materials as liquid hydrogen (used in bubble chamber experiments) gaseous helium, carbon, aluminium, iron, tin and lead and this for muons, pions and protons. This figure is taken in the Particle Data Group.

density-effect correction  $\delta(\beta\gamma)$ . As a particle's energy increases, its electric field extends on the trajectory axis and becomes thicker on lateral directions. Matter becomes polarised and limits the field extension resulting on an increasing  $\delta$  and a decreasing energy loss. In this situation the probability of interaction by the lateral sides of the particle is reduced. In the case of tracker detectors, two scenarios can happen. First, a particle with a  $\beta\gamma$  lower than 5000 will generate only one avalanche in the detector <sup>[f]</sup>. The Bremsstrahlung effect is negligible compared to the ionisation. In contrast, when  $\beta\gamma$  is higher than 5000, it is not the case anymore, it has to be taken into account because the particle is able to generate primary electrons <sup>[g]</sup> with a sufficient amount of energy which allow them to be sensitive to the Bremsstrahlung effect. This sensitivity will generate additional photons which will move freely in the medium until they interact with an electron of the material. The problem in this case is the fact that this photon can move "far" from the first avalanche and so create secondary avalanches distorting the data <sup>[h]</sup>. We will see later that in an ionising detector, a electric potential is used to derive the electron-hole pairs. Applied too strong, it can accelerate them and generate a secondary avalanche.

<sup>[f]</sup> As we will see later, an avalanche is an ions pair (electron-hole) production when a particle ionises a material.

<sup>[g]</sup> Primary electrons are related to a first avalanche. They are the electron-holes from ionisation.

<sup>[h]</sup> We will see later that a Strontium source is used in the measurements. The electrons generated by the Strontium source used can be seen as MIP particles and have an energy of 0.5 MeV and so they don't generate a second avalanche.



# Chapter 3

## Radioactive sources used and their decay modes

This chapter aims to describe the sources used during this thesis which are the 109-Cadmium and the 90-Strontium. Their decay modes will also be explained in order to understand why they have been selected.

### 3.1 Source $^{109}\text{Cd}$ and electron capture

Cadmium has 8 natural isotopes. Two of them are radioactive :  $^{113}\text{Cd}$  (beta decay with a half-life of  $7.7 \cdot 10^{15}$  years) and  $^{116}\text{Cd}$  (double beta decay with half-life of  $2.9 \cdot 10^{19}$  years). Three others are expected to decay but have not been observed so far in laboratory conditions:  $^{106}\text{Cd}$ ,  $^{108}\text{Cd}$  (double electron capture) and  $^{114}\text{Cd}$  (double beta decay). Three others are stable:  $^{110}\text{Cd}$ ,  $^{111}\text{Cd}$  and  $^{112}\text{Cd}$ . Other isotopes do not exist naturally, the ones with the longest half-life are:  $^{115}\text{Cd}$  (53.46 hours) and  $^{109}\text{Cd}$  (462.6 days), all the other variants have a half-life of less than 2.5 hours [10].

The isotope  $^{109}\text{Cd}$  is much used in pixel detector development [10]. Indeed, having an atomic number  $Z$  (e.g. proton number) of 48 and a mass number (protons + neutrons) of 109, it results in 61 neutrons, while the stable Cadmium general form has a mass number of 112 which leads to 64 neutrons. The  $^{109}\text{Cd}$  has a lack of neutrons. To remedy to this, it will decay by an electron capture process.

The electronic capture (EC) has the same effect as the emission of a positron by transforming one of the protons of the nucleus into a neutron resulting in a reduction of its electric charge by one. These two natural processes are used to correct the composition of a nucleus that is too rich in protons. Others decays have the same goal ( for example  $\beta$ -decay ) but from an energy point of view, EC is more economical than the emission of a positron as in  $\beta^+$ -decays. The creation of a positron requires 511 KeV which is its mass energy. The energy available for the decay in 109-Cadmium is less than that and prevents  $\beta^+$ -decays. Below this threshold, electron capture becomes the only mode to reduce excess of protons [11].

As presented on Figure 3.1, the lack of neutron (e.g. excess of protons) in the atom will lead to an absorption of an electron localised in the first electronic orbital. By conservation of the electric charge and the leptonic number, the capture of an electron by a proton results in the transformation of the proton in to a neutron with an emission of a neutrino. This process leaves an empty place in the inner layers. The atom rearranges itself to fill the free space in the inner layers which was left empty by the captured electron. This reorganization is accompanied by emissions of X-rays. If the final nucleus is in an excited state, this process can be followed by emissions of  $\gamma$  photons in order to reach a stable configuration.

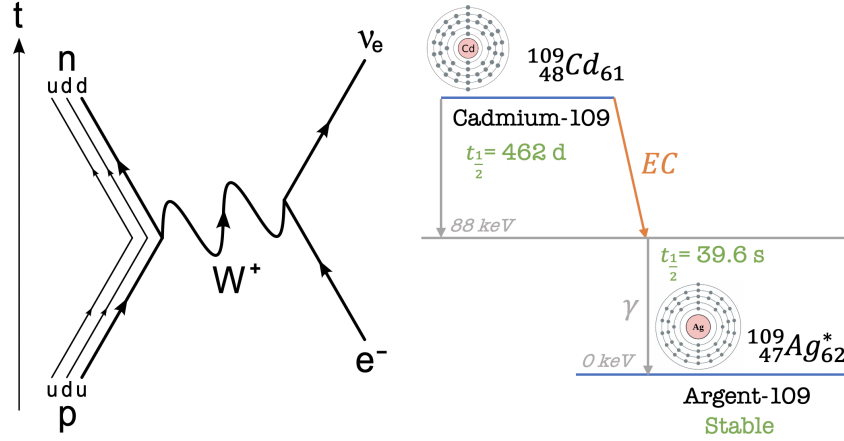


FIGURE 3.1 – This Figure represents on the left side, a diagram for an electron capture process [12] and, on the right side, the decay scheme of  $^{109}\text{Cd}$  and the meta-stable  $^{109m}\text{Ag}$  in  $^{109}\text{Ag}$ . The level energy is in KeV.

As neutrons and protons are not elementary particles, quarks are responsible for this process. Figure 3.1 shows that quarks  $u$  and  $d$  are involved. As quarks have electrical charges and weak hypercharges, the electron capture process is governed by the electroweak theory (electromagnetic and weak forces) which is mediated in this case by the  $W^+$  boson mediator. The charge lowering current  $j_\mu^-$  (vertex of the diagram in the left side of Figure 3.1) transforms a proton to a neutron and the raising current  $j_\mu^+$  (vertex of the diagram in the right side of Figure 3.1) transforms an electron to an electronic neutrino. This is following the reaction :  $u + e^- \rightarrow d + \nu_e$  and  $atom^* \rightarrow atom + \gamma$  for the following photon emission. The right side of Figure 3.1 shows the decay scheme of  $^{109}\text{Cd}$  and the meta-stable  $^{109m}\text{Ag}$  in  $^{109}\text{Ag}$ . The EC for the cadmium leads to a meta-stable state of the 109-Argent with an energy level of 88 KeV. This meta-stable state will emit gamma rays of the same energy to reach a totally stable state. The 109-Cadmium will be used during the calibration and the search of good working points because the photons  $\gamma$  emitted have always the same energy.

### 3.2 Source $^{90}\text{Sr}$ and Beta decay

Strontium is the chemical element with atomic number  $Z = 38$  and its thirty-five isotopes have a mass number  $A$  between 73 and 107. Only 4 of them are present in nature :  $^{84}\text{Sr}$ ,  $^{86}\text{Sr}$ ,  $^{87}\text{Sr}$  and  $^{88}\text{Sr}$ , which are all stable. The thirty-one others are artificially produced in a laboratory. Most of them have a half-life below 70 days and are not very useful in pixels detector development, except one :  $^{90}\text{Sr}$  with its half-life of 28.9 years and its significant beta energy emission. It has a nucleus composed of 38 protons and 52 neutrons decaying in Yttrium-90 (e.g.  $^{90}\text{Y}$ ) by  $\beta^-$  decay [13].

Beta decay is a type of radioactive decay in which a beta particle (energetic electron :  $\beta^-$ , or positron :  $\beta^+$ ) is emitted from the atomic nucleus.

As for the electron capture process, protons and neutrons are not elementary particles and so the charged  $d$  quark (electrically and by the weak charges) implying an electroweak

process. Figure 3.2 illustrates a beta minus decay summarised by the relation :  $n \rightarrow p + e^- + \bar{\nu}_e$ .

The neutrino has been introduced by Pauli because of the fact that measurements showed that  $\beta$ -particle's energy was a continuous spectrum and not a constant value as expected, indicating a decay with three bodies in the final state.

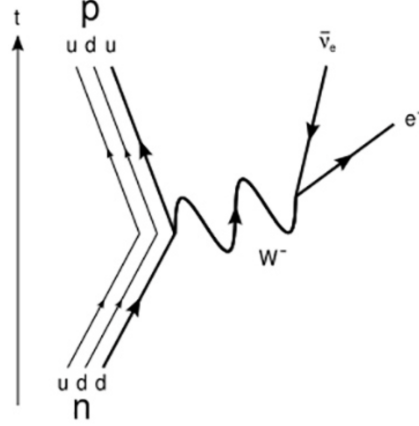


FIGURE 3.2 – A diagram representing a beta minus decay. [14].

Taking into account the fact that the kinetic energy of the recoil nucleus is sufficiently low to be negligible, all the energy from the decay is shared between the  $\beta$ -particle and the anti-neutrino. The electron energy is then spread over a spectrum from zero to a maximal energy value  $E_{max}$  which is equal to  $E_{max}^{90Sr} = 546$  KeV and  $E_{max}^{90Y} = 2.28$  MeV [15]. The left side of Figure 3.3 shows the diagram of the cascade decay of the  $^{90}Sr$  and, on the right side, the spectrum of  $^{90}Sr$  and  $^{90}Y$  which is specific to each of them. Considering the fact that  $t_{\frac{1}{2}}^{90Sr} \gg t_{\frac{1}{2}}^{90Y}$ , a constant equilibrium is present between decays from  $^{90}Sr$  and  $^{90}Y$ .

In trackers, the most interesting particles are the minimal interacting particles (MIPs) because of their low loss of energy in matter. They have a sufficiently high energy to be able to create electron-hole pairs and therefore to be detected while having a very small amount of energy lost. The electrons from the  $\beta$  decays can be considered as minimum ionizing particles when their kinetic energy is sufficiently high. In Section 2.2, it has been seen that the energy deposited by an ionizing particle passing through matter depends principally on its velocity <sup>[a]</sup>. So by high velocity, we assume that more or less  $2 \leq \beta\gamma$  <sup>[b]</sup>, which corresponds, for electrons, to a minimal amount of energy required of  $E_{min}^{electron} \approx 1$  MeV <sup>[c]</sup>. The maximal energy being at  $E_{max} = 2.28$  MeV there is an amount of electrons

<sup>[a]</sup> Figure 2.4 showed that the energy lost by a charged particle increases specially for two ranges which are the very slow and very fast particles. In between the minimum range was observed with a minimum value being  $\approx 1 - 2 \frac{MeV cm^2}{g}$  of mass stopping power corresponding, for example, to a minimal amount of energy of  $e_{min}^{muon} \approx 100$  MeV for the muon,  $e_{min}^{pion} \approx 100$  MeV for the pion and  $e_{min}^{proton} \approx 1$  GeV (values taken from the PDG for to be in the range of MIPs (e.g.  $1 \leq \beta\gamma$ ) shown in Figure 2.4.

<sup>[b]</sup> The value of 2 as been chosen to be close to the minimum ionisation of  $\beta\gamma$  but still smaller and still in the MIP range!

<sup>[c]</sup> A small approximation can be done with  $E^2 = m_e^2 C^2 + p^2 C^2 = m_e^2 C^2 + m_e^2 \gamma^2 v^2 C^4 = m_e^2 C^2 + m_e^2 \beta^2 \gamma^2 C^2$  for  $2 \leq \beta\gamma$  an energy of  $E = m_e \beta\gamma \approx 1$  MeV.

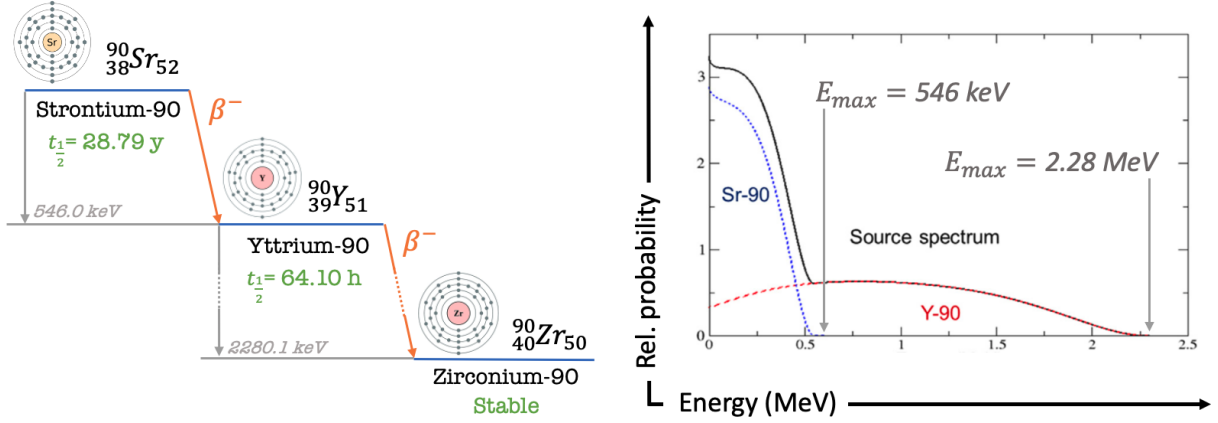


FIGURE 3.3 – On the left side, the Strontium-90 decay diagram which has two  $\beta^-$  decays.  $^{90}\text{Sr}$  decays into a unstable  $^{90}\text{Y}$  that later decays into a stable form of  $^{90}\text{Zr}$ . The  $^{90}\text{Sr}$  lifetime is much longer than the  $^{90}\text{Y}$  one. The right side shows the spectrum of the  $^{90}\text{Sr}$  and  $^{90}\text{Y}$  sources. The combined source electron energy spectrum is in black [16]. The maximal energy value for  $^{90}\text{Sr}$  is  $E_{max}^{90\text{Sr}} = 546 \text{ KeV}$  and for  $^{90}\text{Y}$  is  $E_{max}^{90\text{Y}} = 2.28 \text{ MeV}$  [15].

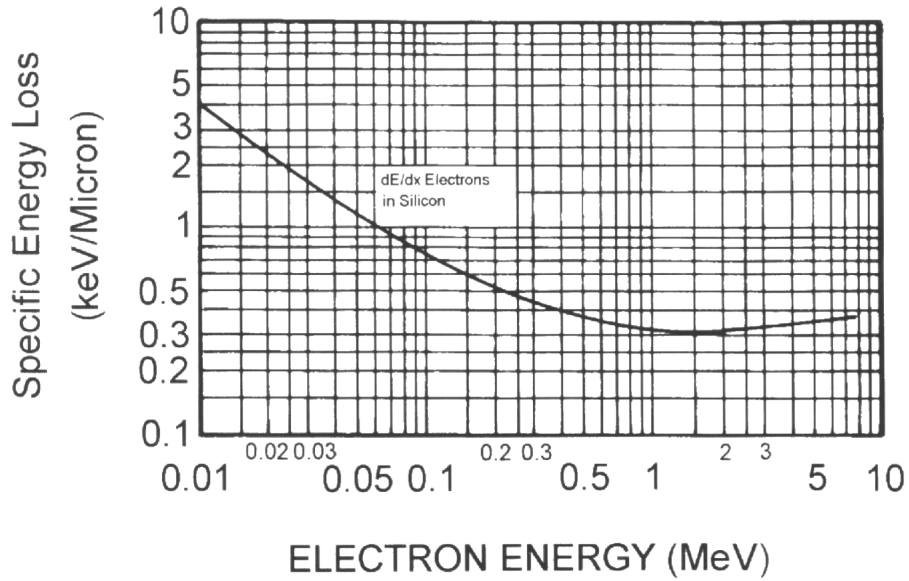


FIGURE 3.4 – Stopping power of Silicon for electrons. The minimum amount of energy deposit is around 1-2 MeV that is why, in silicon, electrons with an energy above this minimum can be considered as MIPs [17].

(between  $E = 1 \text{ MeV}$  to  $E_{max} = 2.28 \text{ MeV}$ ) usable as MIPs.

Most of the time, accelerators of elementary particles providing high energy particles are the most appropriate source of MIPs but, to test and to develop new detectors, they are not the best solution because of the short time in which they are running. That is why for development in laboratory, sources such as  $^{90}\text{Sr}$  are used as a replacement [18].

In order to properly quantify the performances of a detector, it is important to have knowledge of the amount of energy deposited by the traversing electrons. We will see

later that silicon is actually very used in particles tracking. Figure 3.4 [17] shows the stopping power for an electron in silicon. The density of the Silicon is  $2.33 \text{ g/cm}^3$ . The lower energy limit is at 0.01 MeV while the upper is at 10 MeV. The  $^{90}\text{Si}$  spectrum which in combination with the decay of the daughter nucleus  $^{90}\text{Y}$  provides a continuous electron energy spectrum extending up to the range of  $\approx 2.2 \text{ MeV}$  and Figure 3.4 shows that electrons under 2 MeV can be considered as MIPs inside Silicon with an energy loss amount of 0.3-0.4 KeV by micron traversed in silicon (values read in Figure 3.4). That is why  $^{90}\text{Si}$  is an appropriate source to use for silicon detectors under test.

# Chapter 4

## History of detectors for ionizing radiation

In particle physics, the reconstruction of particle trajectories is the goal of various developed devices. The most famous include *cloud chambers*, *bubbles chambers* and *drift chambers* that have been in some ways, the ancestors of the technology used today as the one in silicon trackers. In this chapter, an overview of the main ones will be given leading the reader to the subject of the next chapter concerning the technology used on the ATTRACT prototype which is semiconductors in pixel detectors and their operation.

### 4.1 Cloud chambers

Cloud chambers are one particularly famous detector in particle physics. The experiments using a cloud chamber highlighted the existence of particles by observing them.

Condensation trails from the ionizing particles passing through the material were visible by eye. This detector could be visualised as an airtight container in which a vapour of water or alcohol is present in a supersaturated form. When a particle passes through it, it leaves a white trace which contains thousands of water or alcohol droplets that have condensed as a result of the interaction between the particle and the medium. Depending on the length of the path as well as the density of the droplets contained in the condensed trail, particles can then be identified. The cloud chambers made it possible to observe such particles as, alpha particles, protons, electrons and muons.

The faster a particle is, the less it will interact with the saturated gas and therefore less energy will be lost. In contrast, the slower a particle is, the higher will be the number of ions created in matter. Therefore its trace will be made of many droplets. It can be linked to Bethe equation (Equation number 2.1) which shows that the energy transmitted to the saturated gas is proportional to  $z^2/v^2$  where  $z$  represents the particle's charge and  $v$  its speed.  $z^2/v^2$  is the first term on the equation without the constants.

Without an external magnetic field  $\vec{B}$ , non-relativistic electrons are the lightest particles observable in cloud chambers. They rapidly lose their energy by electrostatic shocks (braking energy / Bremsstrahlung) and have a 'zigzagging' trajectory. In contrast, with an external  $\vec{B}$ , their trajectory is curved and deviated. When an electron is highly energetic, its trajectory can be confused with the Muon's one which is a straight path where the energy loss occurs mainly by ionization.

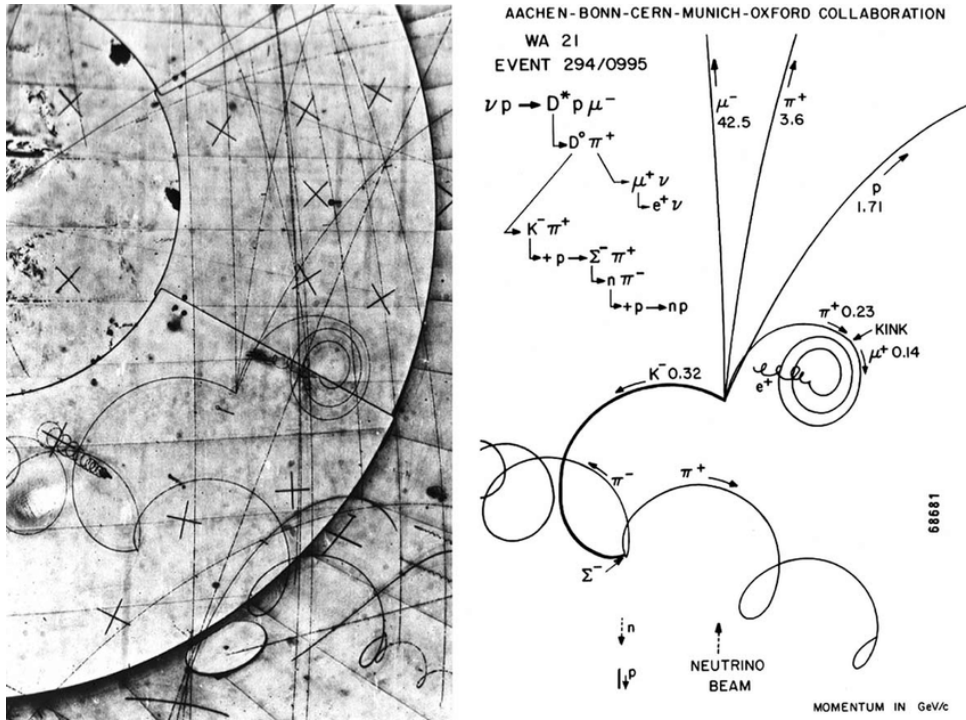


FIGURE 4.1 – Example of complete reconstruction of an event recorded with the Big European Bubble Chamber hydrogen bubble chamber at CERN in 1978 [19]. The incident particles are a neutrino and a proton of the medium. Multitudes of particles are created by this interaction. Under the high  $\vec{B}$ , charged particles have an helical trajectory and the electron resulting from the negative muon has a zigzagging trajectory.

## 4.2 Bubble chambers

The functioning of a bubble chamber is similar to that of clouds chambers, by filling it with a liquid heated to a temperature just below its boiling point. The liquid can be liquid hydrogen in a superheated and metastable state. In thermodynamic, that kind of state would be an unstable critical point which the state transformation is produced by a small perturbation.

The transition is almost instantaneously. The particle ionises the liquid and provides it with the remaining energy needed to reach its boiling point. Once reached, the particle leaves behind a trail of bubbles resulting from the evaporation of the liquid.

Most of the time, bubble chambers are placed in a magnetic field. Exposed to the Lorentz force, charged particles travel along a helical path. By studying the radius and the direction of curvature, the momentum and the charge value can be determined. As with the cloud chamber, photos were taken and then studied.

The list of discoveries made with that kind of chamber is very long. The main discoveries are, for example, the discovery of the theory of the weak neutral current (highlighted by the weak interaction theory) which has lead, several years after, to the discovery of the weak bosons ( $W^\pm$  and  $Z^0$ ). Without going into details, this discovery contributed to the proof on the unification of the electro and weak force to the electroweak force. Many

other discoveries were made such as strange particles, hadrons <sup>[a]</sup> resonances associated to subatomic particles (now known as bosons and quarks) and their excitation which led, several years later, to the discovery of quarks.

Figure 4.1 shows the result of one complete event's reconstruction photographed in the BEBC (Big European Bubble Chamber) hydrogen bubble chamber at CERN in 1978 [19]. The left side is the picture taken and the right side is the reconstructed complete event. Two different kind of trajectories can be observed. Some particles have an helical trajectory due to their non-zero charges and the effects of the magnetic field. This is the case for the meson  $K^-$  (charge:-1) and the  $\pi^+$  (charge:+1). It is interesting to see that the direction of their trajectories are not the same due to their opposite charge value. Particles that do not feel the magnetic field have a straight trajectory. In Figure 4.1, only one particle has that kind of trajectory, the  $\mu^-$ . Even if its charge is negative, and it should experience the effects of the magnetic field, this one is at too high speed. For ultra-relativistic particles, the curvature of their trajectories is therefore not necessarily visible.

### 4.3 Drift chambers

The drift chamber is the successor to the bubble chamber. This type of detectors has several advantages that the previous two do not have. Firstly, the reading processing has been completely redesigned, moving from a photographic study to a faster and more precise computerized processing. This technological advance made it possible to determine with high precision the trajectory of the particles which cross it with a very rapid reading of the output signal.

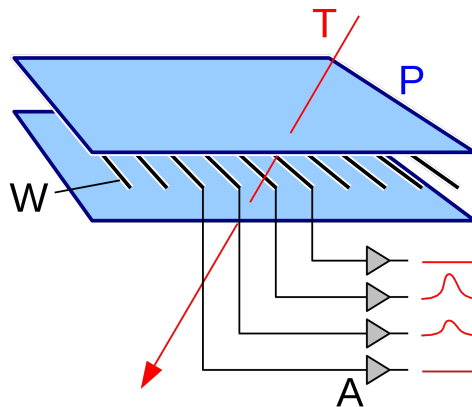


FIGURE 4.2 – Representation of a multi-wire chamber developed by the French physicist Georges Charpak in 1968 at CERN [20]. An ionisation will generate some charges which will be collected by the wires electrodes

<sup>[a]</sup> Depending on the number of quarks they contain, hardrons are divided into two families which are mesons and baryons.



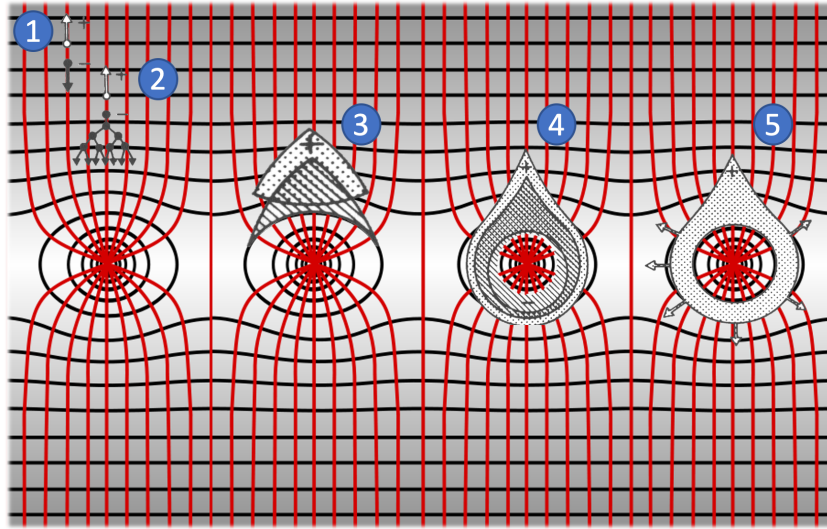


FIGURE 4.3 – When a potential difference is applied between the cathodes and anodes, an electric field is generated (red lines). This  $\vec{E}$  is perpendicular and symmetrical to the wire grid. The black lines are the equipotentials [21].

This detector is a hermetically sealed chamber containing a noble gas (as xenon or argon). Figure 4.2 is a schematic representation of the detector which is composed of planes (cathodes) and wires (anodes) in between. The wires are put on high voltage generating a potential difference between them and the cathodes creating an electric field in the chamber as shown in Figure 4.3 by the red lines going from the anodes to the cathodes. When a particle crosses the detector (as represented by the red line named T for "trajectory" in Figure 4.2), it ionises the gas generating a quantity of free electrons (positive charges) which will drift and reach the anode (the cathode). Under electric field, free charge carriers are subjected to strong acceleration and subsequently collide with other atoms of the gas leading to collision ionization in which energetic charge carriers lose energy by creating other charge carriers. This effect produces an electron avalanche as shown by step 2 in Figure 4.3. While the intensity of an electric field is  $\propto 1/r^2$ , the position of the electron approaching the anode will then influence the intensity of the acceleration by  $\vec{E}$ . The closer the electrons are, the higher will be the acceleration effect leading to an increase in the number of free electrons generated which are increasingly appear like an avalanche effect (step 3). This effect provides a significant gain to the output signal transmitted by the anode. Due to the equipotential levels (represented with the black lines in Figure 4.3), a lateral diffusion of electrons is favoured, generating close to the anode a drop-shaped avalanche encircling it (point 4). Point 5 shows the results after all the electrons are collected. It results on a positive cloud of ions left migrating to the cathodes.

To collect electron-holes in gas-filled detectors, an external electric field has to be applied and the collection of electrons will depend on its strength. Too low or null, it will not be sufficient to accelerate the electrons and the original charge carriers (the ionisation of the gas by the particle) will recombine, in this case the current is in a so-called 'recombination' region. Too high, the acceleration effects will be too strong allowing *Compton scattering*.

In the latter, a free high energetic electron will interact with an atom generating not only another electron but also a photon which is problematic. Having a null electric charge, this photon is not influenced by  $\vec{E}$  and can travel far from the position of the first avalanche. For example, traveling horizontally, the Compton scattered photon can produce a second avalanche. In the case of a multi-wire gas detector, this effect reduces the precision on the track of the incident particle ionising because several anodes become alarmed. This second region is called the '*Geiger region*'. That is why the electric field has to be moderated between these two regions in a so-called *proportional region*.

## 4.4 Semiconductor detectors

The concept of the gas filled detector explained in the previous section can be applied to a solid as well as a gas. When a charged particle loses its energy in a solid or liquid filled detector the process is similar to gas-ionisation. In most solids or liquids, the electrical charges from an avalanche are not able to travel the same distance as in a gas. The reason is simply related to the band theory. But some specific materials are exceptions such as those that are the base of a semiconductor (for example silicon or germanium) where the charges created by ionisation can travel over centimeters. The next section will explain why.

In semiconductors, the energy required to produce electron-hole pairs is very low compared to the energy required to produce paired ions in a gas ionisation. This difference will increase the resolution of the detector due to the lower height variation of the output pulse signal. Compared to gas, they have a higher density making them advantageous because high-energy charge particles can release their energy in a smaller depth. This means much thinner detectors can be made. Most of the time, semiconductor detectors have the shape of very small pixels forming a matrix. Their rapidity, high accuracy and size make them essential for tracking. At Atlas, semiconductor detectors are micro-strips forming part of the inner tracking. To get an idea, 61 m<sup>2</sup> of silicon with 6.2 million readout channels are arranged in 4088 silicon modules of  $\sim 6\text{cm} \times 12\text{cm}$  having 1744 pixels of size  $50 \times 400 \mu\text{m}^2$  by module. Each strip has a resolution of  $\sim 23\mu\text{m}$ . To have a detector with a small front area and a high resolution is the main aim in particle physics and it is what scientists are looking for. The time resolution is the key of a such pixel detector. Having a high temporal resolution means having a thinner distribution and therefore higher precision for potential future discoveries. An extremely high time resolution would result in Dirac Delta for distribution's discoveries. In particle physics, to control the time resolution of a pixel detectors, three parameters are important:

- The reading geometry - weighting field
- Charge collection noise
- Electronic noise

Each point will be explained in the following chapters while The next section will explain in more detail, the operation of a pixel.

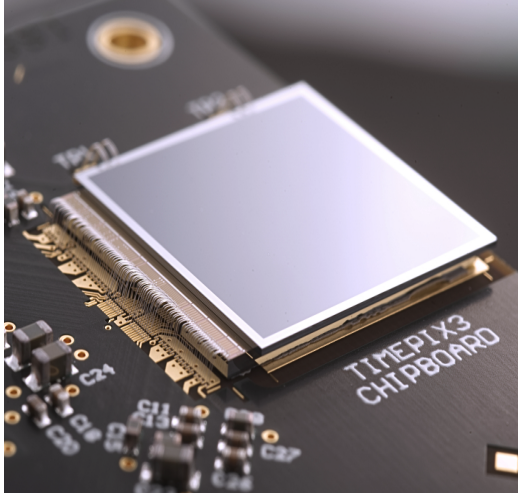


FIGURE 4.4 – Example of a pixel detector developed in the TIMEPIX project. The large glass-like square is the semiconductor sensor which is connected to a chip [22].

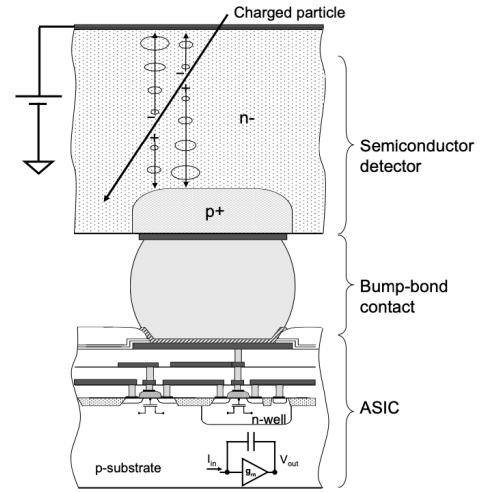


FIGURE 4.5 – A vertical cut of a hybrid type pixel. The upper part is the semiconductor sensor and the lower part the read-out electronic. Between them a bounding has been made.[23]

There are two types of pixel detectors. Those where the electronics are inside the detector. They are called *monolithical* pixel <sup>[b]</sup> and those with the read-out chip separated from the semiconductor sensor part called *hybrid* pixel. In the latter, the two parts are developed separately and then assembled by a bump-bonding process. Figure 4.4 and 4.5 show an example of hybrid semiconductor pixel detector used in the *TimePix* serie experiments for particle detection and X-ray imaging to study the human body. One of its main applications is a 3D colour radiography of a human but also more advanced operations like the Thyroid cancer diagnostics and its treatment monitoring. The pixel is able to generate for each hit, its coordinates and the arrival time for the 3D reconstruction and its energy for the colour information. In other technologies such as PET scanners, the colour is representative of the radiative activity of human tissues. For example, a tumour emits particles more energetic than a healthy tissue, these particles are captured by the sensor and allow a localisation of a possible cancer. Pixels are not only used in the medical sector but are also in many other experiments such as at CERN for bunch crossing reconstruction as well as in many more common applications such as cars driving which is the main topic of the next section.

<sup>[b]</sup> This is the type of pixel chosen for the ATTRACT prototype. That is why no presentations of monolithical pixel is done in this section, it will therefore be detailed later.

## 4.5 Some industrial pixels applications

The first pixel detector was developed in 1984 [5]. Since then, many industrial applications have emerged using pixels. Having been developed the last decades, for example, Time-Of-Flight (TOF) technology.

### TOF cameras

In reality, the TOF technology is not very new and is already implemented in several devices. Undoubtedly the best known is in obstacle detection as for example, with the *Ledar* project in the (semi-)automatic automobile world allowing a three-dimensional reproduction of the environment. The vehicle's computer system can then predict the behaviour of objects and adapt driving accordingly. This is a huge technological advancement because *Ledar* TOF-sensors can be used in classical cars as a driving assistance as well as in autonomous car development, allowing them to drive without a driver. A second example would be the Azure Kinect DC camera developed by Microsoft for a better computer visualisation (a 3D visualisation) as hands controlling or Advanced body tracking to monitor and analyse gestures and behaviour of human body. But these are not the only examples, many others exist in which TOF-sensors are embedded : drones, robotics, face recognition, smartphones, etc...

A TOF camera uses infrared light to determine depth-information. This is how bats perceive their environments.

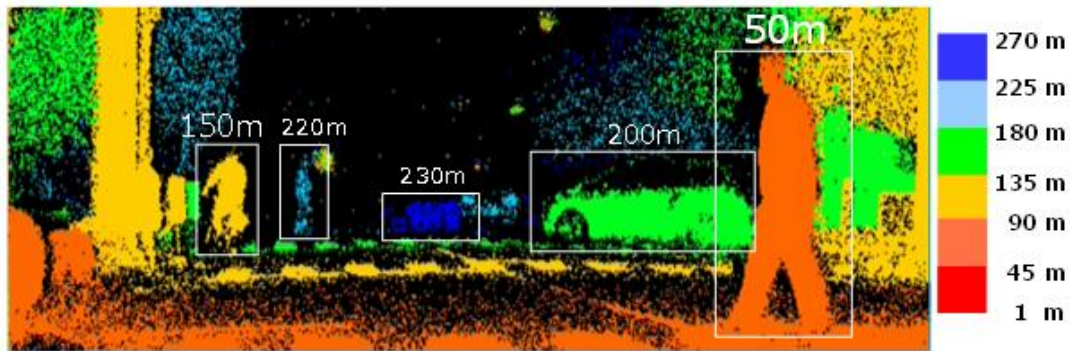


FIGURE 4.6 – *Example of a 3D reconstruction of images obtain at night with an TOF sensor to predict and avoid any obstacles on the road. The distance between the car and objects are represented with various colours [24].*

A light signal is emitted which reaches the subject and returns to the sensor. Considering the fact that the TOF of the light signals is proportional to the distance between the camera and the object analysed (it can also be a room) and the fact that not all the signals come back at the same time, the time taken to rebound is thus measured. This provides depth mapping capability. The depth is then taken into account to create three-dimensional plans. This offers a huge advantage over other technologies, such as 2D-cameras, because it can be used to accurately measure distances in an entire scene

with a single laser pulse. As the time between the impulses is very short, it is easy to understand the benefits of this technology for driving assistance in order to avoid accidents, for example.

Figure 4.6 shows an image reconstruction at night by a TOF sensor. The distance between the car and various objects is represented by a coloured scale. Since there is not only one pixel on a car, several different maps will be produced by the car. A detailed analysis of the behaviour of the objects can then be made. We here presented an overview of pixels and the following sections will provide a detailed explanation of its functioning.

# Chapter 5

## Semiconductors

During the last decades, we have all been able to observe a technological revolution centered on the size of electronic components making it possible to manufacture even smaller electronic components up to the range of the micro-meters. In parallel, the science of semiconductors has also evolved considerably. The most common application used in everyday life by millions of people would be the laptop computer with its central processing unit (CPU) and graphics processing unit (GPU) through their transistors, based on semiconductors, performing fundamental logic calculations. The list of current applications is not restricted to this industry, it also affects a variety of different scientific fields including, of course, physics, such as at CERN with its experiments. Thanks to these technological improvements, smaller detectors have emerged based on the semiconductor physics which are very used in industry as well as in science. They use a whole set of physical effects hidden behind the semiconductors theory. Some examples of semiconductors would be Silicon or Germanium which are a type of chemical element with electrical properties in between those of metals and insulators.

### 5.1 Why choose Silicon ?

From the Seventies, there has been a rapid growth in interest in semiconductors and their use in particle physics [5] for signal detection because of their fast response, the minimum charge deposit required, as well as their size. For that kind of application, silicon was the favorite for several reasons. It was, at this time, the most studied and so very well understood for its electrical properties. Another significant point is its low cost. To understand more of the details of semiconductor detectors, it is necessary to go deeper into their theory, which the topic of this chapter.

### 5.2 Semiconductors Theory

In a single atom, electron energies can only take discrete values. That is not the case in a crystalline material, as periodic lattices are made of atoms having electronic orbitals overlapping each-others. By the Pauli exclusion principle, electrons can not be two in the same energy level with the same quantum numbers. For a crystal composed of  $N$  atoms, this effect generates a small shift of the  $N$  molecular orbitals (e.g. atom's wave functions) giving way to a multitude of possible energy values. As  $N$  is a huge number, this effect leads to extremely close energy levels that can be considered as a continuous energy band. The left side of Figure 5.1 shows a schematic representation of the molecular orbital's degeneration with respect to a different number  $N$  of atoms in a crystal. Having a high number of atoms extremely close in a crystal structure will enlarge an energy band. The

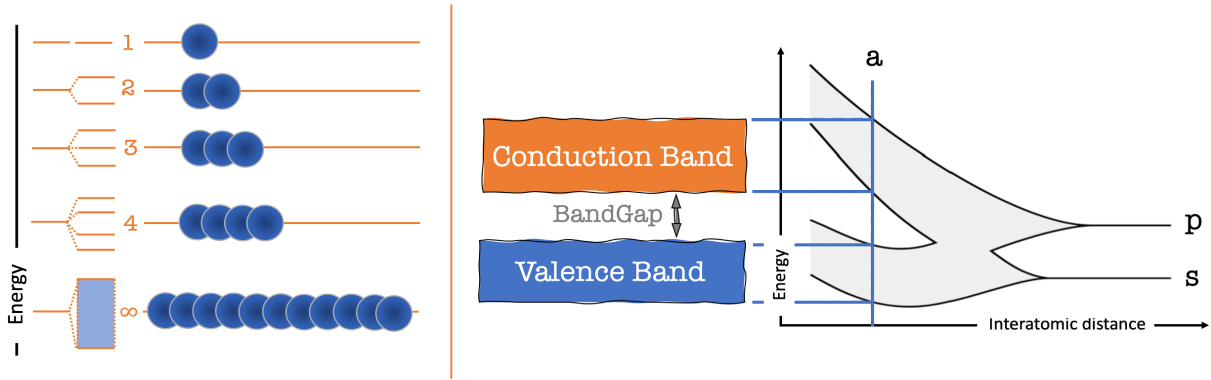


FIGURE 5.1 – *Left side : Concept representation of the formation of energy bands in a crystal. Increasing the number  $N$  of extremely close atoms will expand the energy bands [25]. Right side : Graphic representing the behaviour of the orbital levels of two electrons, located in  $s$  and  $p$  energy levels, depending on the inter-atomic distance between them [26].*

right side of the same figure shows the behaviour of the orbital levels of two electrons, located in  $s$  and  $p$  energy levels, depending on the inter-atomic distance between them. At large distances, no degeneration appears, this is due to the fact that atoms are too far to form a crystal lattice. By decreasing the inter-atomic distance, the electronic structure will be revealed only below a certain distance (of the order of the length of the chemical bonds which is represented with the letter  $a$ ) and a separation between the  $s$  and  $p$  level appears. This separation is called the 'bandgap'. At constant temperature, the distances between atoms do not change, therefore the gap remains the same. This is why, having not enough energy to jump and reach the  $p$  layer, electrons from the  $s$  band are blocked in it.

### 5.3 Band structure

Figure 5.2 is a schematic representation of the band theory in materials which are insulators, semiconductors and conductors. The valence band is localised at the last electronic orbital and is an integral part of the inter-atomic structure of a material. While in insulators there is a large gap between the conduction and the valence band, in conductors it is the opposite case, they overlap. In the valence band, electrons are bounded in the band and so linked to a specific atom in the lattice. In insulators, electrons in the valence band don't have enough energy to jump the gap. In contrast, since conductors gap is very small, the energy necessary to jump is nil and electrons are free to migrate and to move through the lattice composing the material. A potential difference applied to the conductor's extremities causes the movement of free charge carriers located, respectively, in the conduction band for the free electrons and in the valence band for the *free* holes. Semiconductors can be understood as an intermediate material state between the two others, insulators and conductors. It is the same problem, to be conductors, electrons located in the valence band have to cross the gap. One difference, the gap in semiconductors is lower than in insulators. For example, at a temperature of absolute zero degrees,



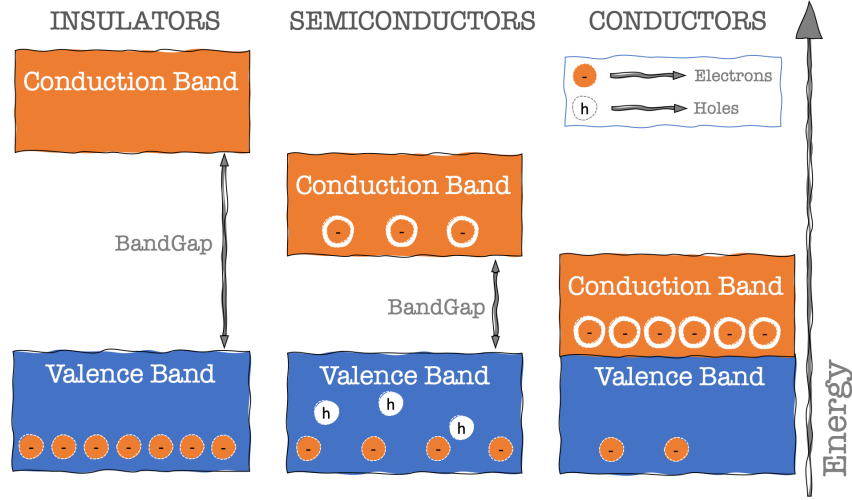


FIGURE 5.2 – *Bandgap representation for an insulator, semiconductors and conductor material.*

a semiconductor is totally insulating, while increasing the temperature will have an effect on the electrons in the valance band, gaining thermal energy. So at a higher temperature, the electrons will have enough energy to jump and the semiconductors will starts conducting current. Note that an electron jumping leaves a hole in the valance band. Holes are represented as positive charges and can also move in the valance band of the crystal by the simple fact that an electron coming from another atom fills it. This effect creates moving electron-hole pairs, if an external electric field is applied to them. Without an external electric field, they recombine between the atoms of the crystal. The Figure 5.3 shows the idea that an introduced atom of  $P^+$  ( $B^-$ ) coming from an n-doped (p-doped) <sup>[a]</sup> procedure has an extra electron (hole) that is able to be recombined with one of the Si neighbours Si atom. That is why semiconductors are specific materials where the electrical properties can be controlled. Temperature is one of the parameters that allows a control on the electron jump but this is not the only one. Indeed, the doping process can also.

## 5.4 Silicon doping

In its natural form, Silicon has in its last orbital, four single valance electrons which are shared to form the crystal lattice shown in Figure 5.3-a. A very common method used to control the conductivity of a semiconductor is the doping process which is the replacement of one atom of a Silicon crystal by another atom having a different number of valance electrons. If the atom introduced has more (less) valance electrons, it will be considered as a donor (acceptor) in electrons and the process will be called n-doped (p-

<sup>[a]</sup> N-doped (P-doped) is the ability to introduce negative (positive) charged atoms in a crystalline structure of a semiconductor.



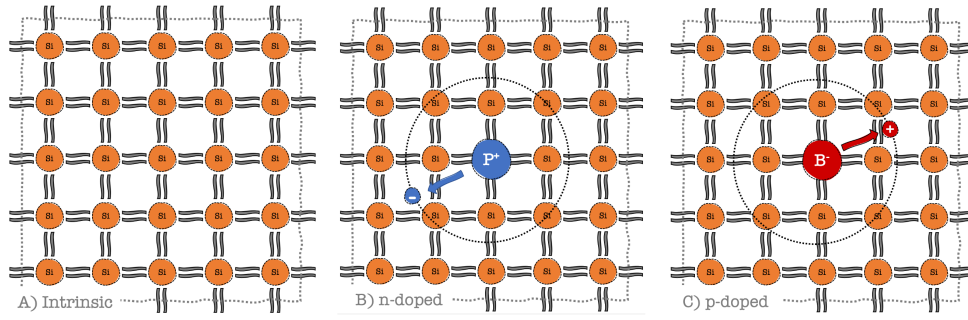


FIGURE 5.3 – Natural crystal layer for Silicon (a), an n-doped (b) and p-doped Silicon layer (c).

doped) <sup>[b]</sup>. Notice that a p-doped process is an analogy to say that holes are introduced in the crystal. Two examples used for silicon doping are the Boron which has 3 valance electrons (p-doped) and the Phosphorus with its 5 valance electrons (n-doped).

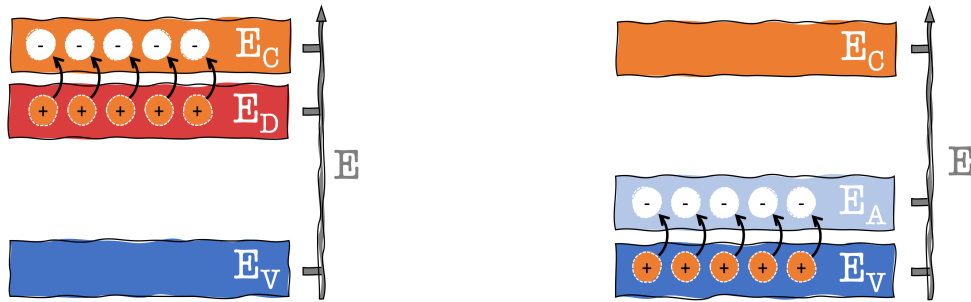


FIGURE 5.4 – Representation of a n-doped (left-side) and p-doped (right-side) substrate. Assuming that the semiconductors is insulated at very low energies, if the temperature increase, the thermal energy of the electrons will increase. If a Phosphorous atom is added, a  $E_D$  band will appears into the bandgap containing electrons having the possibility to jump. Increasing the temperature will let its electrons to reach the conduction band. In the opposite, by adding a Boron atom, holes will appear in a new  $E_A$  band leaving the possibility of the electrons in the valance band to reach them resulting on holes in the valance band that would be able to move in the crystal lattice.

Figure 5.4 shows that the doping process adds charges in the bandgap. In the case of a n-doped substrate (figure 5.4 - left side), the introduction of electrons *donor* atoms will introduce a pseudo energy level located just below the conduction band. The energy needed for an electron to pass the bandgap is generally smaller than for the not-doped semiconductors ( $E_C - E_D < E_C - E_V$ ), leaving the possibility to have an high number of electrons jumping to the conductance band. It is the opposite for a p-doped crystal (figure 5.4 - right side), the introduction of *acceptor* atoms will introduce a new energy level above the valence band. The energy to be supplied to the valence electrons to pass through this

<sup>[b]</sup> The letters n and p refer to a negative surplus and a positive missing of electrons compared to the Silicon atom which has 4 valance electrons.

acceptor level is low and the departure of the electrons causes the appearance of holes in the valence band. Holes that can be filled by an electron's neighbouring atoms and so move freely throughout the crystal. Of course, without an external electric field, the electrons which have jumped to the conduction band will end up recombining themselves with any holes present in the crystalline structure.

In an analysis of the conducting proprieties, as a function of a raise in temperature, three states of conduction can be observed : at very low temperature, intermediate temperature and at high temperature.

At very low Temperature, the doping process is not useful because no electrons have sufficient energy to jump the bandgap and the semiconductor is insulating. All the intrinsic electrons coming from the doping process exist but they are bonded to the donor atom.

At intermediate temperature <sup>[c]</sup>, by intermediate it is assumed a sufficient temperature in which only electrons from the doping process have stored enough thermal energy to be able to jump the bandgap and they will be considered as free electrons moving in the conduction band. Carrier concentration is dominated by the doping process. Without any external electric field, these free electrons will recombine with any holes present in the crystalline structure as shown in Figure 5.3-b. At this temperature, the electrons localized in the valance band of the semiconductors as well as in the acceptor band (for the p-doped case) do not have enough energy to reach the conduction band. This situation leaves free electrons coming from the donor band (for the n-doped case) and free holes in the valance band (for the p-doped process). In this configuration and under an external field, the semiconductors can be either conductor or insulator. It will depend on the negative and positive doping charges. Controlling the density of electrons (n-doped) and holes (p-doped) allows the management of the number of free charge carriers moving into the lattice.

At very high temperature, the thermally generated carriers coming from the intrinsic silicon atoms are confused with the ones from dopants. In this case, the concentrations of charge carriers are dominated by the silicon atoms.

Now it could be said that "if the temperature is able to control the conductivity of a semiconductor under an external field, why do we use the doping process ?" The answer is simple, first, having to install coolers (or heaters) to be able to control the temperature of an experiment can be very expensive and complicated to set up. Secondly, doping allows us to control the conductivity at localized areas in the semiconductors while the effect of temperature is a less localized influence. We will see in the next chapter, that the operation of a fundamental electronic component, called the transistor, is based entirely on this second reason.

## 5.5 PN-junction

Until now, it might be confusing to understand how the doping process could be used in particle detection. For this the reader has to understand the pn-junction process. When a particle passes trough a sensor, it is ionized. By ionization, a certain quantity of the

---

<sup>[c]</sup> For silicon, this temperature can simply be the room temperature.

particle's energy is given to the electrons in the crystal. As it has been explained in Chapter 4, this energy gain will allow a quantity of electrons, previously bonded in the crystal lattice, to reach the conduction band, generating an amount of charge carriers concentrations. Without an external electric field  $\vec{E}_{ext}$ , they will recombine with each other but, with an  $\vec{E}_{ext}$ , they will reach the electrodes collecting them. Now the question is how the signal generated by the interaction of a particle would be more distinguishable using the doping process <sup>[d]</sup> ?!

In semiconductor sensors, the main goal is to decrease sufficiently the amount of charge carriers to be able to see only the signal coming from the particle's ionisation. For this, there are two different ways to proceed, either by decreasing the temperature which will also decrease the density of free electrons and holes. However, this kind of cryogenic process is not very practical and implies additional costs, so when we have a huge experiment this method is not the most appropriate. Or, alternatively, to deplete the semiconductor <sup>[e]</sup> forming a PN junction by joining a p-doped and n-doped Si side.

### 5.5.1 PN-junction in thermal equilibrium

In thermal equilibrium, the two materials are initially electrically neutral. They are put in contact as shown in Figure 5.5. The left side represents the situation of the two semiconductors without contacts.

Assuming that the pink part is a p-doped region and the purple a n-doped, by thermal diffusion, electrons and holes of each material will be attracted by the opposite charges contained in the other doped type. They will be driven across the junction until they recombine together. This flow of electrons will create à border to each material, a so-called '*depletion region*' leaving behind a positive final charge border area (composed of positive ions) in the n-doped substrate and generating a negative charge in the p-doped region (composed of negative ions). The *depletion region* can be seen as an interface between n-type and p-type silicon which is completely depleted and without any charge carriers. Only fixed electrons and holes bonded to atoms in the crystal are present in this area. It becomes an intrinsic non-conductive semiconductor material. Being attracted to their opposite charge but not able to reach it, a dipole will be generated.

The initial concentration of doping charges in the two sides will move, generating an electric intrinsic field inside the depletion area. A potential called '*built-in potential*' will occur by the dipole created and increase until an equilibrium balancing the initial drift and diffusion flows of the charge carriers. This new intrinsic potential will avoid the electrons and holes to cross a potential barrier of  $\Delta E$  as shown in the right side of Figure 5.5. This potential barrier must be overcome by an external voltage source to make the junction conducting. If by chance a free charge carrier were in this zone, it would be directly attracted by the dipole and would migrate to the opposite charge side.

---

<sup>[d]</sup> The list of p-n junction applications could be long, in the case of this thesis only two applications will be presented: the case of detectors and transistors (explained in the next chapter).

<sup>[e]</sup> Forming the sensing part of our detector.

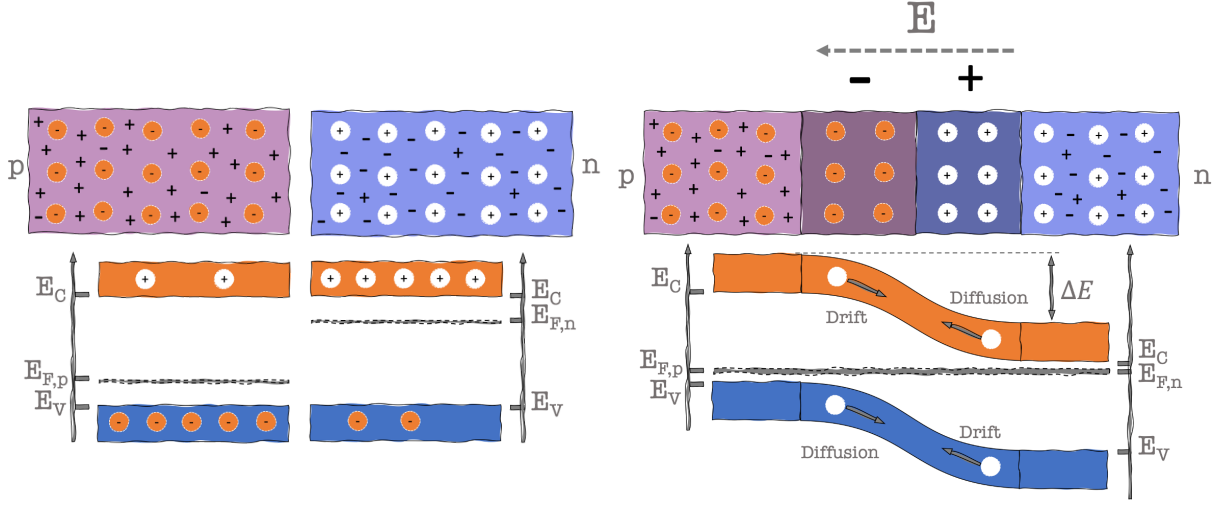


FIGURE 5.5 – Representation of the  $V_{build-in}$  when two Silicon layers are put in contact. The pink one is a p-doped Silicon and the purple a n-doped Silicon. When they are put in contact (right side), all the free charges contained in each of them will travel to the other to recombine with an opposite charge carrier. At this point, a depleted region is formed, having the same effect as a dipole acting in the opposite direction to the movement of the charge carriers movement generated by an external source, limiting the flux.

### 5.5.2 PN-junction with external current

Applying an external bias will allow it to increase or to decrease the length of the depletion region and this depends on its polarisation. Figure 5.6 illustrates, on the right side, the case if an external voltage is applied in the same direction as the  $V_{build-in}$  and, on the left side, the case if an inverted one is applied. The formula representing this process can be expressed by equation 5.1. [27].

$$W = \sqrt{\frac{2\epsilon_0\epsilon_{Si}}{e} \left( \frac{1}{N_A} + \frac{1}{N_D} \right) (V_{build-in} - V_{bias})}, \text{ with } V_{build-in} \approx \frac{kT}{e} \ln\left(\frac{N_D N_A}{n_i^2}\right) \quad (5.1)$$

$W$  represents the depletion length.  $N_A$  &  $N_D$  are, respectively, the p-type (acceptor atoms) and the n-type (donor atoms) doping concentration.  $V_{build-in}$  is the built-in voltage.  $V_{bias}$  is the external voltage.  $\epsilon_0$  and  $\epsilon_{Si}$  are the vacuum and the silicon permittivity.  $e$  is the elementary charge  $e^- \sim 1.6 * 10^{-19} C$  representing the unit of the electric charge.  $T$  is the temperature in Kelvin. Most of the time it is around room temperature.  $n_i$  is the  $e^-$  concentration and the  $h^+$  concentration in undoped semiconductor material and, in this case,  $n_i = n = p$ .  $kT/q = V_T$  is the thermal voltage at room temperature which is equivalent to  $V_T = 26$  mV.

If an inverted bias is applied ( $0 < V_{bias} < V_{build-in}$ ), it will shorten the depletion length. A special case is when  $V_{bias} > V_{build-in}$ , electrons in the conduction band (in the n-side of the junction) can migrate without effort to the conduction band of the p-side of the junction. There is no longer a barrier.

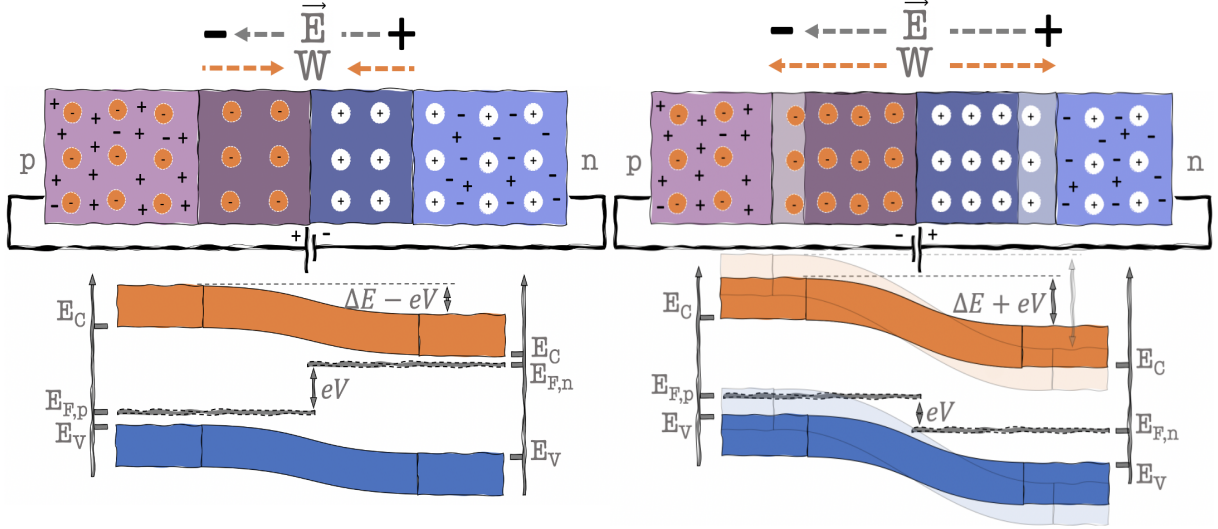


FIGURE 5.6 – Representation of the effects when an external bias  $V_{bias}$  is applied on a PN-junction. If the  $V_{bias}$  is applied in the same direction as the generator, the  $\Delta E$  is reduced, having the effect, of a reduction of the depletion region. On the other hand, if the direction is opposite, the  $\Delta E$  will increase such as the length of the depletion [28].

The second case would be the application of the external bias in the same direction as  $V_{build-in}$  which results in an increasing effect on it. Applying  $V_{bias} < 0$  to the equation 5.1 will increase the barrier having the consequence that electrons will need a higher energy to jump to the conduction band <sup>[f]</sup>.

The depletion region is free of charge carriers. For particle detection, the main goal will be to apply a  $V_{bias}$  at a sufficiently high level, to deplete all the sensor's volume, so when a particle passes through and ionises it, all electron-hole pairs created will be separated by the intrinsic electric field inside  $W$  generated by  $V_{bias}$  and each charge carrier will drift to its respective electrode. Fine tuning the length of the depleted area will enable the creation of efficient sensors.

## 5.6 Particle detection with semiconductors

Semiconductors use the same detection principle as a gas-filled ionisation chamber but the main difference is the substrate, in silicon detectors it is the semiconductor crystal. The main advantage using this technology is related to the minimal energy required to produce an electron-hole pair. This being 3.6 eV compared to the 20 eV for a gas ionisation detector [5]. It allows the use of less energy required to detect a particle's ionisation. This is very important ! Indeed, if less energy is required it is possible to detect particles which only interact very weakly with our detectors and therefore increase its sensitivity. But less

<sup>[f]</sup> As a reminder, if a charge carrier is present in the depleted regions it will be attracted to its opposite sign area forming the depleted junction. We can see it as resulting in a capacitor depleted of charge carriers where the undepleted p and n-regions are the electrodes and the depletion region is the dielectric.

energy also means a higher resolution in the electric signal and a better energy resolution could be reached (this will be explained in detail in Section 9.3). A second advantage is the optimisation of the surface. With a depletion extending to the entire area of the sensor it is possible to optimise and make the detector more effective. Another un-mentioned advantage with an entire depleted sensor is the fact that, taking into account that noise is always present in electronic devices, the signal-to-noise ratio can be lowered. Indeed, if we take for example the fluctuation of temperature, for a detector having a fixed depletion area and not total, there will always be some electrons which store sufficient energy to jump the wall junction and so generate extra noise in the output signal. Creating a larger depleted area will reduce this. The length of the depleted area is not the only parameter allowing to make efficient sensors. Indeed, as it has been mentioned in Section 4.4 that there are also the size and the geometry of the electrodes (which can be considered as pixels) which are more than important because of their influence on the *weighting field* generated inside the sensor. The next section will present the Shockley-Ramo theorem who rules that.

### 5.6.1 Shockley-Ramo theorem

The Shockley-Ramo theorem states the relationship between the current induced  $I_k$  in an electrode  $k$  of a sensor by a moving charge  $q_i$  with its drift velocity  $\vec{v}_d(t)$  and position  $\vec{R}(t)$ . The result of the theorem is written in Equation 5.2 (Rossi and al. [5]).

$$I_{ind,k} = \sum_i q_i \vec{v}_{d,i}(\vec{x}(t)) \wedge \vec{E}_w(\vec{x}(t)) \quad \text{with} \quad \vec{E}_w(\vec{r}) = \nabla w_k(\vec{r}) \quad (5.2)$$

$w_k(\vec{r})$  can be seen as a *weighting potential* (and so  $\vec{E}_w$  the *weighting field*). It describes the coupling of a charge to an electrode. This potential satisfies Laplace's equation ( $\Delta V = 0$ ) with boundaries conditions on the electrodes as  $w_k = 1$  at the electrode  $k$  and  $w_k = 0$  for all the electrodes  $j \neq k$ . This field has to be seen as a property depending only on the position and the space (size, volume and structure of the electrodes and sensor).

If a charge  $q$  moves along a certain path from its initial point  $z_0$  to the position of the readout electrode  $z_{el}$ , the induced charge  $Q_k$  on an electrode  $k$ , is written in Equation 5.3.

$$Q_k = q[w_k(z_p) - w_k(z_0)] \quad (5.3)$$

It's important to understand that the *weighting potential* is different from the *electric potential*. The electric field will determine the drift velocity and the trajectory of the charge carriers while the *weighting potential* describes how the charge motion induces a charge to an electrode  $k$ . The induced charge does not depend on the trajectory.

Figure 5.7 presents the vector field inside the depletion region. On the left side, the geometry of the sensor has been made with electrodes separated by a certain distance. On the right side, the electrodes are closer to each other and longer. The main difference between the two situations is that, in the first one, depending on where the particle pass through the sensor, the pulse in output will not be the same. This effect cause several problems. The field lines intersect themselves which means that a charge located at the

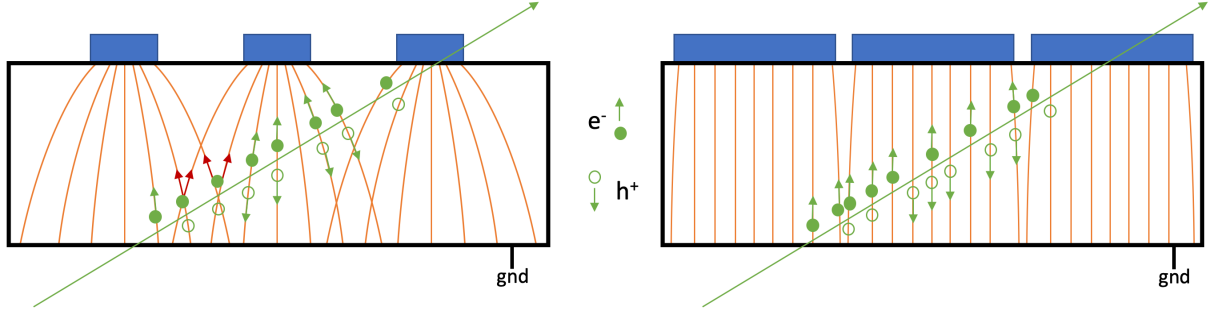


FIGURE 5.7 – Representation of the weighting field driving charges carriers to electrodes on two different configurations of pixels detectors.

lines intersection will have a certain percentage which will be directed towards one electrode and another percentage towards another, it will then be distributed over several electrodes and leading to a less precise measurement. Knowing the fact that the precision in a particle track reconstruction is the main goal the second situation is more efficient.

Equation 5.2 can be adapted to the large and close pixels of the second situation in Figure 5.7 with Equation 5.4.

$$I_{ind,k} = \frac{\vec{v}_{s,d}}{D} \sum_i q_i(t) \quad (5.4)$$

Where  $D$  represents the depth of the sensitive part in the sensor and  $\vec{v}_{s,d}$  the saturated drift velocity of the charges carriers. *Jacobini and al.* published in 1975 the results of the drift velocities for charge carriers in Si and estimate the saturation at a range of  $2 - 3 \cdot 10^4 \frac{V}{cm}$  of the field. Figure 5.8 presents in graphics form the results obtained. The left side (right side), the characterisations for the electrons (holes) at different temperatures. Decreasing the temperature has the effect of increasing the drift velocity and so the performance of our detector.

By providing an analysis of Equation 5.4, it is possible to make a simple prediction of the intrinsic sensor noise. The first term  $\frac{\vec{v}_{s,d}}{D}$  is a constant and so not a part of the noise source which comes instead from the second term  $\sum_i q_i(t)$ . Assuming that two events with the same amount of deposit charge and the same configurations <sup>[g]</sup> (as shown in Figure 5.9) are detected. In the case of the ATTRACT prototype the time of a signal is about 10 ns <sup>[h]</sup> and the thickness is 60  $\mu m$  so the noise coming from the collection charge can be ignored.

By following the points listed in Section 4.4, if the amount of noise coming from *The reading geometry - weighting field and charge collection noise* is very low, it is then

<sup>[g]</sup> The signal configurations and parameters will be explained in the section called *Electronic*. For now, the signal configuration will simply be defined by its initial raising shape and the time in which signals cross the threshold (initial time and final time). But to be more precise with the word *configuration* we should take into account the Time-Walk and say that they have the same Time-Walk.

<sup>[h]</sup> This value can be observed on the graphics presented on the data acquisition section.



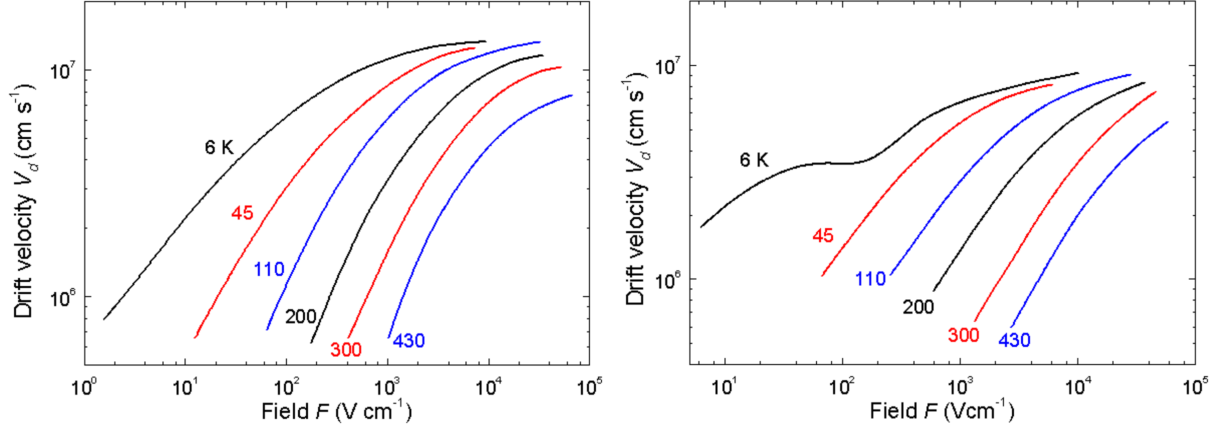


FIGURE 5.8 – Behaviour of the drift velocity of charge carriers in Silicon as function of the electric field [29]. Left side : electron. Right side : holes. At room temperature the value for saturation is close to a field value of 2-3 kV/cm. Decreasing the temperature pushes the asymptotic limit higher.

possible to reach the bar below 10 ps of temporal resolution <sup>[i]</sup>. If it is not the case, this observation implies that an extra noise source can appear called *electronic noise*. The next section discuss a general approach of electronic applied in pixel detectors, how it works and also some sources of its noise.

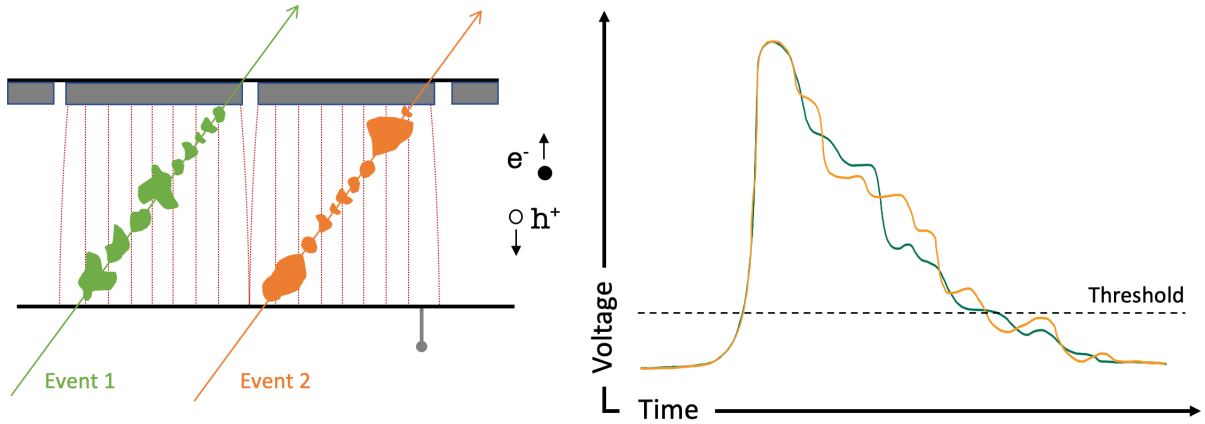


FIGURE 5.9 – Representation of two similar hits generating signals with the same amount of charge and the same configurations and this under a large electrodes generating the same weighting field. By configurations, at this level, only the time over threshold, the raising shape, the initial and final time will be taken into account to describe them. The only difference between this two signals is the behavior of the decrease and so the collecting charge.

<sup>[i]</sup> Source: discussion with Lorenzo Paolozzi, It will be shown that the results obtained with the AT-TRACT prototype are in the range of 30 ps.



# Chapter 6

## Electronics

In a pixel detector, the electronic components are critically important because they manage the output signal from the sensor part in a such way to make it readable. The read-out assembly has this function. Indeed, after an ionisation, the  $e^-$  and holes resulting will reach their respective electrodes. The resulting signal will pass through several electronic elements (transistor, amplifier, ...).

This chapter is divided in three parts. The first one concerns the operation of a diode. Its purpose is to lead the reader to understand the second section which concerns the operation of the transistors. The last section talks about Germanium doping which can be practiced on transistors in order to increase their performance while keeping the noise low.

### 6.1 Diode

Diode is a semiconductor polarised dipole in common use because of its current conduction in only one direction. It has low resistance in one direction and an high resistance in the other. Figure 6.1 shows the symbol of a diode in an electric diagram and also a material representation of what it looks like. This small electrical component is used in any type of electronic devices. It is introduced, for example, into a circuits which contains components which need to respect the polarity and therefore do not damage them.

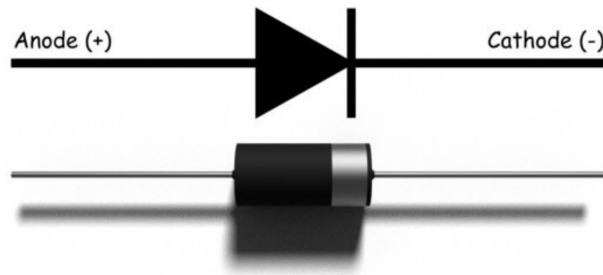


FIGURE 6.1 – *Representation of a diode symbol*[30]

Diodes are made of Silicon with each side doped with opposite charge impurity (for example Phosphorus and Boron as explained in Section 5.4) to create a  $p-n$  junction (as explained in Section 5.5.2) which generates a barrier having a voltage  $V_{build-in}$ .

When an external potential is applied in the opposite same sense as the dipole inside, (e.g. the positive/negative pole of the external voltage source is connected to the negative/positive pole of the diode), the depletion area will increase. This is simply due to the fact that the electrons of the negative part of the junction are attracted by the holes generated by the positive pole of the external voltage source and vice versa. This effect

means that diodes have a reversed tension which means that if the external potential applied in parallel is higher than this one the diode will break. The depletion zone can be seen as a charged capacitor so increasing the reverse bias voltage  $V$  increases the thickness of the depletion zone and reduces the capacitance of the sensing element [5].

However if you reverse the power connection, the situation is reversed. Two situations occur which are : if the external potential is lower or higher than  $V_{build-in}$ . In the first instance, the current simply does not flow. Arriving at a certain voltage, the insulating  $p-n$  junction can no longer resist the incoming amount of moving electrons and the current then circulates through the junction. The threshold voltage (e.g.  $V_{build-in}$  is the minimum voltage for a diode to let the current pass. It should be understood that the voltage applied by the external source allows the electrons to jump above the barrier generated by the negative pole of the junction (in normal time, the electrons, being negative, are pushed back). Once electrons have jumped into the depletion zone, they are drained, by their attraction to the positive pole of the depletion zone. Like on a treadmill. Once done they flow through the external circuit.

A diode can then be used in a circuit to protect against alternating currents, or even, when (one or more) is put in series in a circuit, generates a voltage drop (like resistances). This may be of interest, if the electronic component (or more simply, a stack) which follows the diode, has a maximum voltage threshold smaller than the one generated by a generator. If diode are used in series, drops are cumulative. Diodes can also be used together to form more complex electrical components such as transistors which are the subject of the next section.

## 6.2 Bipolar Junction Transistor

The bipolar junction transistor or BJT was invented in 1948 at Bell Telephone Laboratories in New Jersey (USA) [31]. Because of their high speed, low noise and output power advantages, BJT are very common in high-frequency and analog applications. They can easily be integrated into complementary metal-oxide-semiconductors (CMOS) chips. <sup>[a]</sup> . This process is called BiCMOS technology. The word *bipolar* refers to the fact that in BJT both electrons and holes are involved in the its operation.

A BJT is made of three parts as shown in Figure 6.2 and 6.3. A heavily  $n^+$ -doped emitter <sup>[b]</sup> , a  $p$ -doped base and a  $n$ -doped collector forming together a npn-BJT. When they are put in contact two depleted regions are generated.

Without a power supply (connected to the Base) having enough voltage to overcome the potential barrier, the BJT is in an off-state. This situation is shown in the bottom of Figure 6.2 assuming that the two generators are switched-off.

---

<sup>[a]</sup> By this terminology, CMOS is not what we call the transistor, but the type, architecture, family, technology used to manufacture logic circuits.

<sup>[b]</sup> The emitter is more heavily doped than the collector. Therefore, it has a lot more carriers of negative charges which are free electrons located in the conduction band.

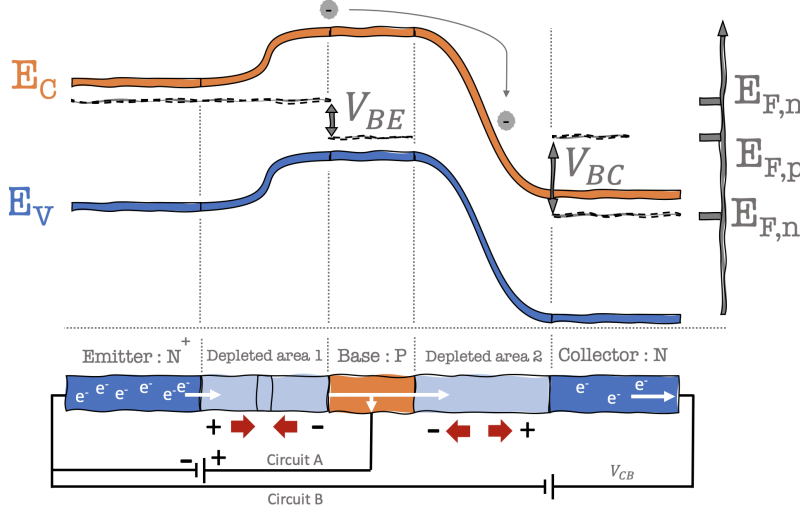


FIGURE 6.2 – Representation of the energy bands of a npn transistor. The three regions are : emitter ( $n^+$ -doped), the base ( $p$ -doped) and the collector ( $n$ -doped). In active mode, there are two electron flows: the first one is the minority electrons (circuit A) and the second is the majority electron flow (circuit B). With an  $\vec{E}_{ext}$ , the first junction (E-B) shrinks while the second one (B-C) expands. Because of  $\vec{E}_{ext}$  generate in the circuit A, the first one is easily crossed by the electrons generating an accumulation (of  $e^-$  in the base) which will force them to jump over the second one. These are then drained through it by the dipole.

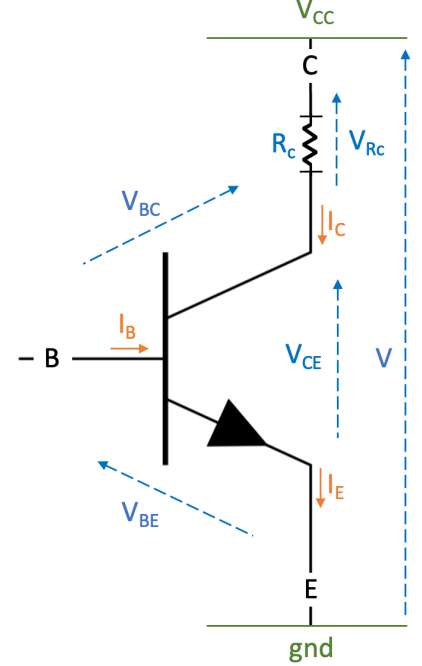


FIGURE 6.3 – Representation of an npn transistor with the various potentials generated inside the two junctions. The current flows from C to E while the  $e^-$  flows in the opposite direction.

Figure 6.2 also shows two circuits : *circuit A* and *circuit B* which are described on the following text.

### Circuit A

Circuit A is connected to a direct diode. The *Base-emitter* pn-junction is a barrier in order to make the current flow and surpass the barrier, an external potential has to be applied. This is the main aim of the minority amount of electrons flowing through the *circuit A*. If a  $V_{BE} > V_{build-in,1}$  is applied then there is cancellation of the potential barrier of the *Base-Emitter* junction. In Figure 6.2, this cancellation is represented by a narrowing of the depletion area between the Base and the Emitter with the red arrows. The whole free electrons (circuit A and B) previously located on the emitter terminal can move through the base  $n$ -doped region. Therefore the operation of a direct diode implies the circulation of charge carriers and therefore of a current  $I_B$  (this current can be seen in Figure 6.3).

### Circuit B

Initially, the base-collector junction is polarised in a reverse bias and therefore would

appear to be blocked. In other words, no free charges should be able to pass through this second barrier. In reality this is not what will happen. A great effect called the transistor effect will occur instead.

Inside the *Depleted area 2*, Two observations can be had. Firstly, an elongation of this area is observable. This is due to the fact that the *circuit B* makes the *Depleted area 1* thinner but, contrarily, due to the reversed bias effect, it makes the *Depleted area 2* larger. Secondly, this *Depleted area 2* can be seen as a dipole having an reversed electric field appearing in it. So if by chance, an electron was in it, it would be attracted by the positives signs of the dipole generated in the *depleted area B*.

So now the question is how a free electron would reach this second depleted area. In reality, the Base region is not big as it as be drawn on the bottom of Figure 6.2 and so a very low quantity of holes are present and available (doped with a low quantity of phosphorus atoms for example). This is very important because it implies that not all the free electrons coming from the emitter will recombine with a hole present in the base. This effect results in an overpopulation of electrons into the base. The electrons diffuse across the base to the edge of the reverse-biased base-collector junction and get swept into the collector by the electric force (as shown with the small gray electron in Figure 6.2). This produces a collector current named  $I_C$  <sup>[c]</sup> in Figure 6.3. This collector current  $I_C$  is independent of  $V_{BC}$  as long as it is a reverse bias.  $I_C$  is determined by the rate of electron injection from the emitter into the base and so determined by  $V_{BE}$ .

We understand that the pn-Junction between the Base and the Collector is not working in a traditional way because of the transistor effect. The base controls the *more or less large* opening of the collector.

### 6.2.0.1 The different operating regimes of the transistor

Depending on  $V_{CE}$ , transistors can be in two different working regimes:

- **Linear regime** ( $V_{CE} > \sim 0.5V$ ): in which the transistor has the possibility of having an infinity of states (not at the same time). The flow of the current can take several intensities. In this case, the dependency of  $I_C$  on  $I_B$  will be linear by a constant factor called *Beta*. This is also in this region where the *transistor effect* works. As has be explained in the previous section, the *Base Emitter* junction is open and flowing while the *Base-Collector* is closed.
- **Saturation regime** ( $V_{CE} < \sim 0.5V$ ): In this regime, the transistor can be in two states. The first one is being in a *saturated* state. It is the state where the current flows through the transistor. The second state is *blocked* when the current is no longer flowing. In this case, the linearity between  $I_C$  and  $I_B$  is no longer respected. The *Base-Emitter* and *Base-Collector* junctions are open and flowing.

In the case of the logic system, we need a transistor under saturation regime (e.g. *on* or *off* states). In the case of an amplifier, we need linear type transistors which are able to react to weak currents (currents which would be below the threshold of the transistor at

<sup>[c]</sup> Remember that electrons are going in the opposite current direction.

saturation mode).

To have  $I_C > 0$  and a flowing current in the transistor, a base current must be applied as  $I_B \geq I_C/\beta$  and  $\beta$  is called the current gain of the transistor. The next section will show that it is very important to take into account this parameter because of its great sensitivity to the variations of temperature and to the radiations.

### 6.3 The current gain $\beta$

As has been explained previously, there are two possible scenarios for electrons crossing the *Depleted area 1* and arriving into the base. Firstly they can recombine with the holes already present in the base. The base is very thin, has few holes and in addition, there is the potential field  $V_{EC}$  (from the transistor effect) which is able to accelerate them to the collector. The majority of free electrons coming from the emitter will travel to the collector (assuming that the amount of electrons following this is  $\alpha$ ). By a small calculation using Ohm's law and Kirchhoff's Law, we can illustrate the relations below (where in equation 6.2,  $V_{CC}$  represents the low voltage power supply : LVPS):

$$I_E = I_C + I_B = \alpha I_E + (1 - \alpha)I_E \quad (6.1)$$

$$V_{CC} = V_{BE} + V_{BC} \quad \text{with} \quad V_{BE} < V_{BC} \quad (6.2)$$

The amount of electrons following the *circuit B* (Figure 6.2) will be defined as a part  $\alpha I_E$  of the current  $I_E$ , while the electrons reaching the collector and following *circuit A* is defined as a part  $(1 - \alpha)I_E$ . Another small amount of current has to be taken into account, the amount of current flowing from the base to the collector named  $I_{CB0}$ . Following to Equation 6.6, the linear regime can be found. The gain constant  $\beta$  is expressed in Equation 6.7.

$$I_C = \alpha I_E + I_{CB0} = \alpha(I_C + I_B) + I_{CB0} \quad (6.3)$$

$$\Rightarrow (1 - \alpha)I_C = \alpha I_B + I_{CB0} \quad (6.4)$$

$$\Rightarrow I_C = \frac{\alpha}{1 - \alpha} I_B + \frac{I_{CB0}}{1 - \alpha} \quad (6.5)$$

$$\Rightarrow I_C = \frac{\alpha}{1 - \alpha} I_B = \beta I_B \quad (6.6)$$

At room temperature the current  $I_{CB0}$  is negligible so  $\beta = \frac{\alpha}{1 - \alpha}$ . The current gain parameter of a transistor is define in engineering as :

$$\beta = \frac{\text{collector current}}{\text{base current}} \quad (6.7)$$

While  $0 < \alpha < 1$ , but by the transistor effect  $\alpha$  would rather tend to be close to 1. Thus by Equation 6.6, it is deduced that the amount  $\alpha I_E > (1 - \alpha)I_E$  and so  $I_C > I_B$ .

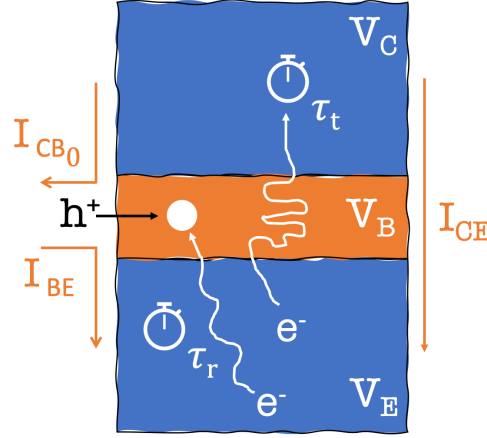


FIGURE 6.4 – Representation of a transistor with the recombination time of the holes introduced into the base and the transit time of an electron following from the emitter to the collector. The coefficient  $\beta$  is defined as the ratio between them.

The physical approach of this parameter  $\beta$  is by transforming the Equation 6.7 using a temporal approach with  $\tau_t$  and  $\tau_r$  (instead of currents) as represented in Figure 6.4. As electrons travelling from the emitter to the collector will take a certain time  $\tau_t$  to cross the two depleted junctions, if there are a lot of holes in the base,  $\tau_t$  will be longer while the time  $\tau_r$  during which a hole added in the base remains, before recombining with an electron coming from the emitter, will be shorter and vice-versa.  $\beta$  can be expressed in terms of these two times :

$$\beta = \frac{\tau_{recombination}}{\tau_{transit}} = \frac{\tau_r}{\tau_t} \quad (6.8)$$

The best scenario would be that an electron traveling with a shorter time from the emitter to the collector while the holes into the base remain longer. That means a high percentage  $\alpha$  and so a high gain value. Figure 6.4 represents a transistor with its collector, its base and its emitter part.  $V_{CE}$  is applied between the collector edge and the emitter edge.  $V_{BE}$  is the potential between the base and the emitter and  $V_{CB_0}$  the potential generated by eventual electrons present in the base feeling the transistor effect (the one supposed to follow Circuit A).  $\tau_t$  is defined as the electron's time of transit from the emitter to the collector and  $\tau_r$  is called the recombination time.

For example, if  $\tau_t = 10$  ms and  $\tau_r = 2$  ms so  $\beta = 0.2$  having as a consequence a decreasing gain factor. On the other hand, if  $\tau_t = 2$  ms and  $\tau_r = 10$  ms,  $\beta$  will takes the value of 5 and so  $I_C$  will be 5 times  $I_B$ . The condition  $\tau_r > \tau_t$  is needed.

## 6.4 Noise sources

As it has been well proven <sup>[d]</sup>, the absolute electric system without noise does not exist except if nothing happens. But in this case, no electric field circulates and no experiment can be realised. Here is why, as soon as an electron is in motion, or more generally, a current flows in a conductor, a noise appears. The electronic noise has multiple sources. Several kind of noise sources can be distinguished, firstly the irreducible noise sources (called White noise), which are the thermal noise and the shot noise, and secondly the reducible noise sources which are the excess noise sources such as the Flicker noise.

The white noise is considered as the sum illustrated on Equation 6.9 while the total noise is presented in equation 6.10.

$$\sigma_W = \sigma_{th} + \sigma_{sh} \quad (6.9)$$

$$\sigma_{tot} = \sigma_W + \sigma_{Fl} \quad (6.10)$$

### 6.4.1 The thermal noise

The thermal noise is generated by the stirring of the charge carriers passing through a conductor and is a consequence of their Brownian motion. It is present in all passive resisting elements.

In 1906, Einstein predicted that the movement of free electrons in materials could lead to the appearance of a fluctuating electromotive force across any resistance that is in thermal equilibrium [32]. This thermal noise is identical for all types of resistors of the same value and is independent of manufacture. It is therefore not reducible.

The thermal noise ( $\sigma_{th}$ ) can be modelled as a voltage source ( $\sigma_{th,V}$ ) and as a current source ( $\sigma_{th,I}$ ) depending on whether a resistor is connected in parallel or in series. Equation 6.11 shows their explicit form [33].

$$\sigma_{th,V} = \sqrt{RK_BTBW} \quad \sigma_{th,I} = \sqrt{\frac{K_BTBW}{R}} \quad (6.11)$$

$K_B$  is the Boltzmann constant which commonly equals to  $\sim 1.38 * 10^{-23} \frac{J}{K}$ .  $T$  represents the temperature.  $BW$  is the bandwidth (a difference of frequencies :  $\Delta f$ ) and  $R$  is simply the resistance value in  $\Omega$  units.

Squared, they can be seen as the variance of the voltage applied per Hertz unit of Bandwidth. This implies a strong dependency on the bandwidth (scale) used for the measurements. The smaller is the bandwidth, the lower will be the thermal noise.

This notion can be applied to conductive wires, resistances but also to more complexes structures such as transistors, etc...

---

<sup>[d]</sup> A general approach on experimental physics is assumed.

### 6.4.2 The shot noise

The Shot noise is associated to the flow of a current. It has been named like this after the name of W. Schottky, who revealed it. It results whenever charges are crossing a potential barrier (like the p-n junction explained previously) and resulting on a purely random event. This noise is independent of the temperature.

Without going into detail, this little explanation is a good illustration of this source of noise : each time a charge carrier crosses a potential barrier with a transit time  $t_t$ , an elementary current pulse is generated. If several electrons cross at the same time, it will bring on a combined impulsions and therefore be more intense. However, the number of electrons crossing the potential barrier is not the same for all  $t_t$ , it fluctuates. An instantaneous value of the resulting current will fluctuate around its average value. This fluctuation is the source of the shot noise.

### 6.4.3 Flicker Noise

While the two previous noises were independent on the frequency of the signal, this is not the case for the Flicker noise. The Flicker noise is proportional to  $\frac{1}{f}$ . This proportionality makes it very pronounced at low frequencies. Low-frequency noise is a term representing the sources of background which are in excess, detectable at low frequency. Since the list of the low frequencies noise sources is not exhaustive, only the main source (Flicker noise) is described here.

The Flicker noise is due to the defects and impurities present in the crystal lattice of the material which can be seen as traps. These traps will randomly release or capture the charge carriers flow involving a large number of generation and recombination processes. This effect generates a fluctuation of the material's resistivity (seen another way : the mobility) depending on the position.

The Flicker noise is present in all electronic devices and is proportional to the amount of the current flow in it and it can be observed in systems like vacuum tubes, diodes, transistors, etc...[34].

A simple illustration of this noise would be to see the electrons moving as cars in a traffic jam. When the flow of electrons arrives close to a barrier, an accordion effect can appear causing a slowdown. So to be able to see the effects of the Flicker noise, a certain amount of current has to be flowing through the device.

## 6.5 Noise Characteristics and Equivalent noise charge

Since the noise sources have amplitudes that are randomly generated in time, they follow a Gaussian distribution density function. The Shot and the thermal noises have Gaussian distributions but the others mentioned on the previous section, do not. So the variance  $\delta = \sigma^2$  is the average mean-square about the average value. That is followed by the fact that the Gaussian standard deviation of the noise can be characterised as a standard deviation which will be called the root mean square (referring to  $RMS = \sigma = \sqrt{\delta}$ ). That means the noise can have amplitude reaching very high values but the probability



of this happening is very small. An effective limit is  $\pm 3\sigma$  representing 99.7%. Figure 6.5 represents the probability of the noise's amplitude related to the rms value [35].

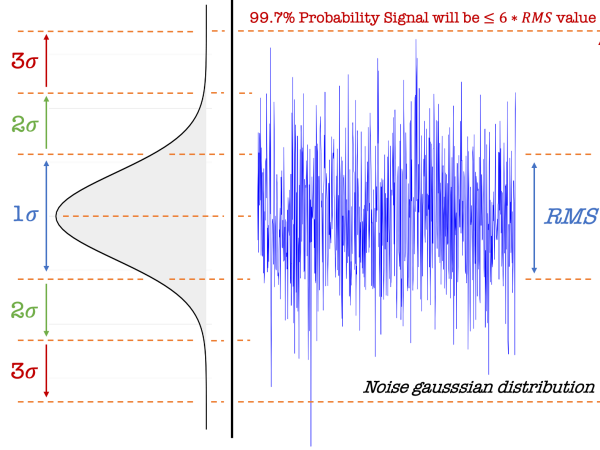


FIGURE 6.5 – Representation of the white noise distribution following a Gaussian distribution, most of the noise's amplitude are contained into a  $3\sigma$  range. The RMS value represents the root mean-square (standard deviation) of the noise distribution. [35]

In measurements, the noise has always been a preoccupation for those who design electronics because of the fact that it is a crucial specification for the performance of an electronic system. In particle physics, we use detectors delivering a charge for a given energy deposit, that is why it is interesting to refer the electronic noise to a charge on the input (of an amplifier for example) known as the Equivalent noise charge (ENC). A general definition of ENC would be the noise charge which produces an output of the same magnitude as an impulse signal of equal charge[36]. It is defined as :

$$(ENC)^2 = \left( \frac{\text{noise output voltage (rms)}}{\text{signal of output voltage for an input charge of one electron}} \right)^2 \quad (6.12)$$

$$= (ENC_{Parallel})^2 + (ENC_{Serie})^2 + (ENC_{\frac{1}{f}})^2$$

$$ENC = \sqrt{k_1\tau_n + k_2\frac{C_{tot}^2}{\tau_n} + k_3C_{tot}^2} \quad (6.13)$$

The first term is the physical noise *currents* due to either a current or a resistance in parallel with the detector. The second term is the physical noise *voltage* for a current or a resistance in series with the detector. The third term is due to the series  $1/f$  noise.

The terms  $k_1\tau_n$ ,  $k_2/\tau_n$  and  $k_3$  are the noise integrals (over the time) <sup>[e]</sup> for the parallel (current) white noise, for the series (voltage) white noise and for the  $1/f$  noise respectively.  $C_{tot}$  is the total input capacitance (detector and amplifier) and  $\tau_n$  is the integration time.

<sup>[e]</sup> For more information, the reader can refer to the reference number [36].

For a  $\tau_n = 200$  ns, the parallel component,  $ENC_{Parallel} * \tau_n$ , is negligible. For a BJT, the  $ENC_{1/f}$  can also be ignored [36] so the only factor remaining is the  $ENC_{Serie}$  term which is  $\propto \sqrt{k'_1 R_B + k'_2 / \beta}$  [37] and depends on such parameters as the temperature  $T$  and the geometry of the amplifier because the  $R_B$  is simply the base resistance. Indeed, the resistive effects depend on the geometry (sphere, rectangular parallelepiped, etc.) of the device.

Sine  $ENC_{Serie} \propto \sqrt{k'_1 R_B + k'_2 / \beta}$ , the main goal to reduce  $ENC_{serie}$ , is to reduce the  $R_B$  and increase the gain  $\beta$ . A good way to increase  $\beta$  is to increase the transit time  $t_\tau$  of electrons from the emitter to the collector (as presented in Equation 6.8). A solution to increase  $t_\tau$  would be to make the base thinner but it would increase  $R_B$ . An equilibrium between  $R_B$  and  $\beta$  is necessary. Another solution is to use Heterojunction bipolar transistors (HBT-SiGe). Instead of having an electron diffusion from the emitter to the base (as in the BJT), Germanium atoms can be added into the base to obtain an electron drift in order to increase the transit time  $\tau_t$ . The next section will show that this solution increases the gain  $\beta$ .

## 6.6 Heterojunction bipolar transistor - SiGe

The first heterojunction structure was proposed by William Shockley in 1948 [38] stipulating that a traditional Bipolar-Junction-Transistor could have improved performance in terms of the flow of minority carriers (electrons on the P side and holes on the N side) if either the emitter, or the base, or the collector had a different forbidden bandgap due to the introduction of differing semiconductors such as Germanium. It is so-called a heterojunction bipolar transistor (HBT) <sup>[f]</sup>. In the case of the HBT-SiGe, only Ge atoms will be introduced into the base. To understand the distinctions between the HBT-SiGe and the BJT, it is necessary to enter into the bands structures theory for each of them. Indeed, the difference in terms of performance is hidden in it. The main goal of using the HBT-SiGe doping process is to improve the performance of the BJT by modifying the Si structure band for a better electron flow. In this part, a presentation of the crystalline and electrical properties of a silicon-Germanium alloy will be given in order to highlight the interests of the incorporation of Germanium into a BJT.

### 6.6.1 Crystalline structure and bandgap of SiGe

The reason that Ge is chosen for this process is due to the fact that it has the same crystalline structure as Silicon which is a face centered cubic structure (FCCS) and when they are combined together the same crystalline structure remains [39]. Figure 6.6 represents the FCCS [38], the grey spheres represent the Si atoms while the blue ones the Ge atoms. They are therefore completely mixable and all the compositions of the alloy  $Si_{1-x}Ge_x$

<sup>[f]</sup> For the remainder of the document, the acronym HBT-SiGe will be used for a heterojunction bipolar transistor doped with germanium and the acronym BJT for a bipolar junction transistor made of Silicon.

can be obtained [40] ( $X$  represents the number of Si atoms deducted and the number of Ge added).

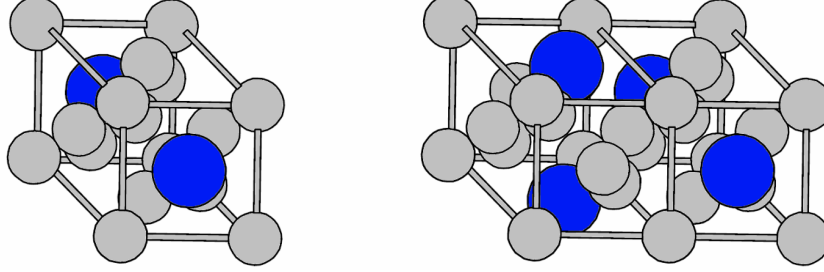


FIGURE 6.6 – Examples of a SiGe mesh with the Si atoms in grey while the Ge atoms are in blue. In this example a number  $X=2$  of Ge atoms are added to the  $Si_{1-X}Ge_X$  alloy. The main structure of Si and Ge as well as SiGe are the face centred cubic structure mesh represented by the grey lines[38].

There is still a difference: the lattice constants which are 5.65 Å for the Ge and 5.29 Å for Si [39]. The schematic representation of the lattice structures of the Si is presented in 6.7-(a). For a reasonable doping % of Ge, this difference of lattice constant between them will force the SiGe lattice to grow with a horizontal compressive stress of a layer while the vertically axis increases. This is called a pseudo-morphic growth as shown in 6.7-(c). Due to this constraint, the SiGe layer has must not be too thick (until a critical limit  $h_c$ ) - strongly dependent on the % of Ge introduced into Si layers - otherwise it relaxes and creates dislocations in the interface as shown in 6.7-(b) which strongly degrade the electrical performances of the alloy [41].

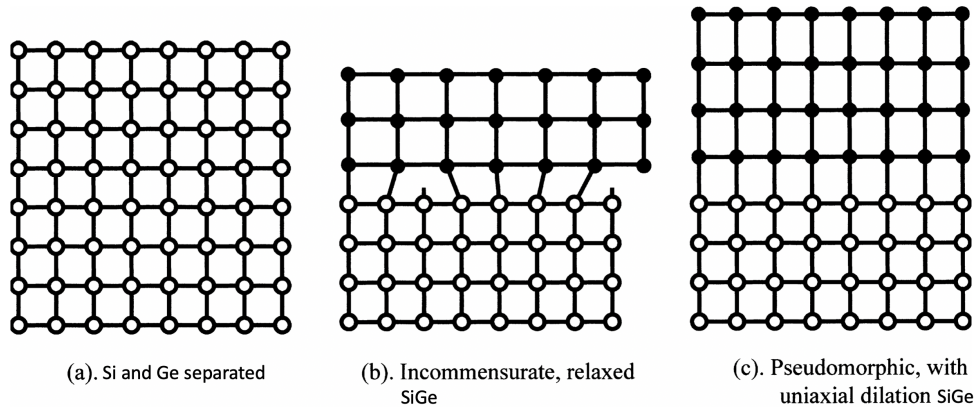


FIGURE 6.7 – Representation of a lattice of Si (a), a relaxed (b) and pseudomorphic structure (c) [41] when Si is Ge-doped. The thickness of the lattice has to be under a critical value  $h_c$  to stay as a pseudomorphic structure of keep the electrical performances of SiGe. Above  $h_c$ , the performances decrease which is no longer optimal for the transistor due to the breaking.

The width of the bandgap of the SiGe  $\Delta_{g, SiGe}$  is a non-linear relation strongly dependant on the quantity of Ge introduced in the Si lattice as presented on Figure 6.8. The  $E_{g, Si} \approx 1.12$  eV while the  $E_{g, Ge} \approx 0.66$  eV at 296 K. Two distinct behaviours can be observed, the first one, lower than  $\approx 15\%$  of Si and the other one greater. In the first one, SiGe will be Ge-like (meaning that the behaviour of the energetic bands of SiGe will be similar the Germanium ones) and the in second one, Si-like.

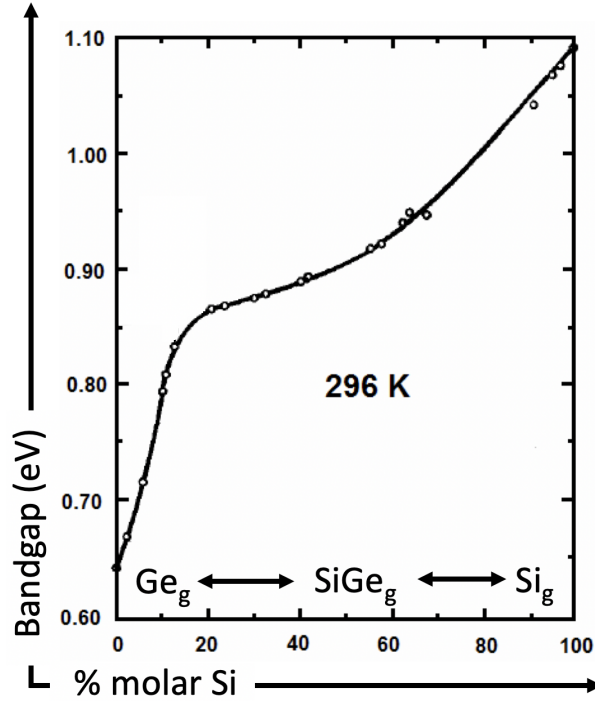


FIGURE 6.8 – Representation of the size  $\Delta E_{g, SiGe}$  of the bandgap of the SiGe in term of the molar % of Si [38]. Two regimes can be observed (above and below 15%). In the first one the SiGe alloy will be Ge-like while Si-like in the second. Theoretically, the electrical performance of SiGe increases with the increase of the % of Ge. However, above 30%, the crystalline SiGe lattice can break up, which has the opposite effect. Therefore, a equilibrium must be found.

In the next chapter the reader will see that theoretically it is favorable to have a high amount of Ge % because of the fact that a lower bandgap promotes the jump and so the flow of electrons in the HBT but in reality it is difficult to control thin and pseudo-morphic layers with more than 30% without the risk of the appearance of defects and dislocations. A risk which will increase with the increase in the percentage of Ge in SiGe because it increases the thickness of the heterostructure and therefore the probability of the appearance of dislocations and therefore of a relaxed SiGe [38].

### 6.6.2 Energy Bands in HBT-SiGe

As explained in Section 6.2, the BJT is a junction using the injection of minority charge carriers in the base, in order to control the current of majority charge carriers from the

emitter to the collector. Figure 6.2, showed that the bandgaps  $\Delta E_{gap,Si}$  are the same for the three regions and is equal to  $\approx 1.2$  eV for the silicon at room temperature [42]. Due to the introduction of Germanium in the Silicon, the band structure of a HBT differ from the BJT one. The doping in Ge has several consequences. The most significant is the reduction of the bandgap. This is every 1%-molar more of Ge in Si in the order of 7.5 meV [38]. A schematic representation of the situation is shown on the bottom of Figure 6.9. The introduction of Ge into the base impacts the conduction band which is reduced on the base-collector side. The majority electrons coming from the base see a lower potential barrier to cross the base towards the collector while the holes see the same barrier resulting in an improvement of the current gain compared to the BJT. The top of figure 6.9 shows the energy bands diagram of a HBT-SiGe while the bottom shows a profile of the gradual Ge concentration into the base. The base current  $I_{BE}$  (presented in Figure 6.4) remains unchanged because of the fact that the injection of holes from the base to the emitter is determined by  $V_{BE}$  forming the heterojunction base-emitter. As shown in Figure 6.2,  $V_{BE}$  is determined by the difference level of the valance bands of the emitter and base.

Lowering the potential barrier in the conduction band allows an increase in efficiency in terms of electrons injection through the base-emitter junction as well as an increase in the base-collector current  $I_{BC}$  and therefore a current gain of the transistor. Moreover, the transit time  $\tau_t$  explained in Section 6.3 is reduced and so, by equation 6.8, the current gain  $\beta$  increases (e.g. equation 6.7, the base current  $I_B$  is constant while the collector current  $I_C$  increases and  $\beta$  increases). The increase of the base doping  $p^+$  compared to a BJT makes it possible to reduce the base resistance  $R_b$  (shown in Figure 7.5) as well as the low frequency noise level [38].

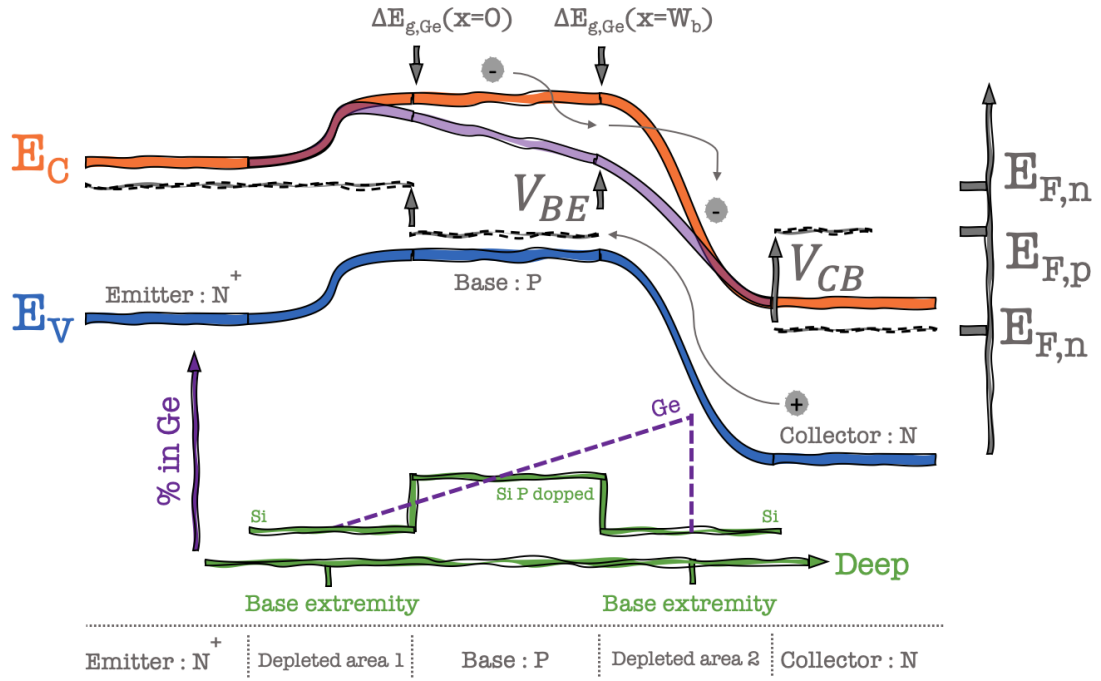


FIGURE 6.9 – Bottom: schematic representation of the two Si junctions with in the middle the concentration of the Si p-doped. The dashed line represents the increase of the concentration of Ge inside the Si forming the SiGe. The deep containing the maximum of Ge is found at the base-collector junction. Top: Diagram representing the energy bands of a HBT-SiGe. The purple line represent the decrease of the conduction band respect to the gradual increase of the Ge concentration. The  $\Delta E$  of the SiGe bandgap is in between the one of Si and Ge.

# Chapter 7

## The prototype (ATTRACT project)

Figure 7.1 presents the main board on which the ATTRACT prototype <sup>[a]</sup> (in the center) has been set up. The green silicon card has electric printed circuits connecting the pixel detector to several inputs and outputs. Starting from the bottom, the copper connections are the analog outputs of the pixels studied which are connected to low-loss coaxial cables. These are used as a transmission line for routing the signal to the oscilloscope in order to minimize the dispersion of the signal in frequency. The left side has two connectors. A back cable which is connected to the high voltage (HV) generator and a multicoloured wire which is connected to the low voltage power supply (LVPS) generator (as defined in Section 6.3). On the right side a General Purpose Input/Output (GPIO) port is connected to a Field-Programmable Gate Array (FPGA) which is simply an integrated circuit designed to be configured after manufacture. The FPGA used is an *Altera cyclone V* [43].

In the center of Figure 7.1, the ATTRACT prototype is glued and then bonded onto the green main board. Figure 7.2 is a close-up of it while Figure 7.3 is a computerized representation putting forward its pixel matrices structure. The ATTRACT prototype chip is divided into 5 different pixels matrices, named  $Q1$  to  $Q4$  and  $A$ , which are, respectively, the double Threshold matrix ( $Q1$ ), the Postamp matrix ( $Q2$ ), the Active matrix ( $Q3$ ), the Standard matrix ( $Q4$ ) and the Analogue matrix ( $A$ ). Since only the analogue matrix is used for this thesis, the other ones will not be explained. The pixel shape used is the hexagonal one.

The monolithic ATTRACT prototype integrates a front-end electronic circuit composed of a HBT-based preamplifier and two drivers. For the measurements presented in this document, the output from the sensing part was sent through them and then directly readout by an oscilloscope.

The HBT-based preamplifier has programmable bias component (a pseudo-resistance) operating with a supply current in the range between  $10\ \mu\text{A}$  and  $200\ \mu\text{A}$ . The output of the preamplifier was sent out from the chip using two drivers allowing the measurement of the signal. In this prototype, the measurement of the signal characterisation of the output of the amplifier was not possible. This section creates an overview of the characteristics of the chip as well as the integrated electronic circuit.

---

<sup>[a]</sup> By abuse of language, we will call the prototype the "ATTRACT prototype" but this simply refers to the name of the project.



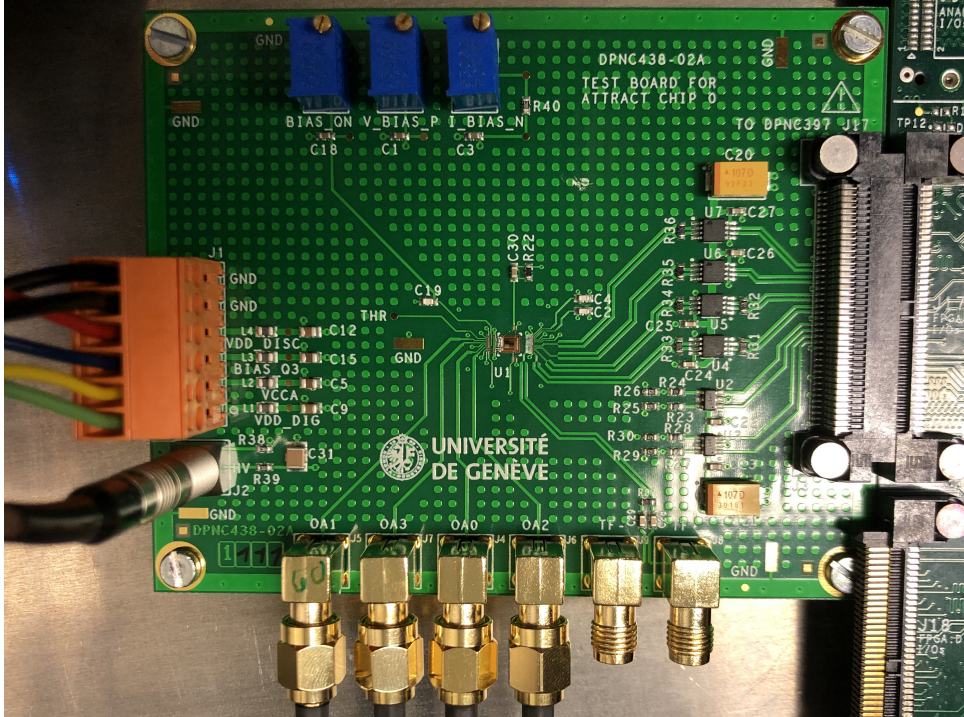


FIGURE 7.1 – Presentation of the board on which is wire bounded the ATTRACT prototype. Several input/output connections are visible, such as, the copper ones which are low-loss coaxial cables transmitting the output signal from the pixels to the oscilloscope. The other board connected on the right side of the figure is the FPGA board. This is a picture taken during the measurements.

## 7.1 Characteristic form of the chip

Two types of manufacturing of pixel detectors exist : the *Hybrid Pixel Detector* (as the one in the *TimePix* presented in Figure 4.5) and the *Monolithic Pixel Detector*. The first one is very flexible because the electronic and the sensor parts are manufactured separately and after bonded together making its development simpler but at the expense of a higher price<sup>[b]</sup>. *Monolithic Pixel Detector* is a cheaper alternative. It allows the possibility of building both electronics and sensor in the same technological process. Thus avoiding many manipulations related to the bonding used in the *Hybrid pixels* and also reducing the capacitance of each pixel and so obtain a very low-noise performance[5].

A standard sensor part of a pixel detector has been presented in Figure 5.7. The ATTRACT prototype is a monolithic pixels detector realized on a thin layer of p-doped silicon in which some SiGe-electronics (explained in Section 6.6) and charges collectors (which are the pixels) are incorporated. The situation is presented on the top-left of the Figure 7.4. A pn-junction is realized between the n-doped pixels and the p-type epitaxy

<sup>[b]</sup> For example if the electronic part costs 10, the sensor part will cost 20 and the bonding will be between 80 and 100. The bonding is about 3 times the price of the electronic and sensor parts combined.



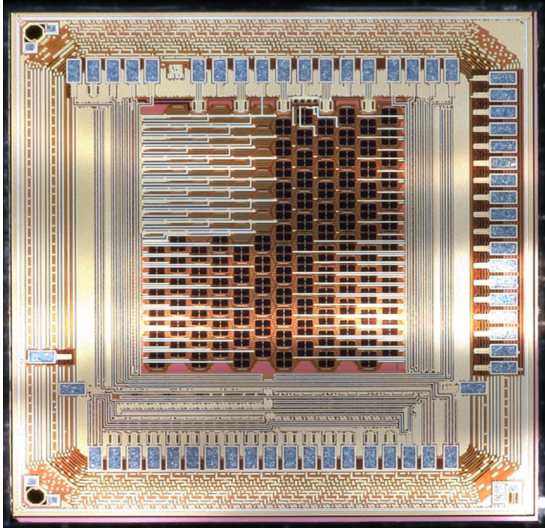


FIGURE 7.2 – Picture of the sensing part of the ATTRACT prototype as it can be seen through a microscope. The pixel shape used is the hexagonal one.

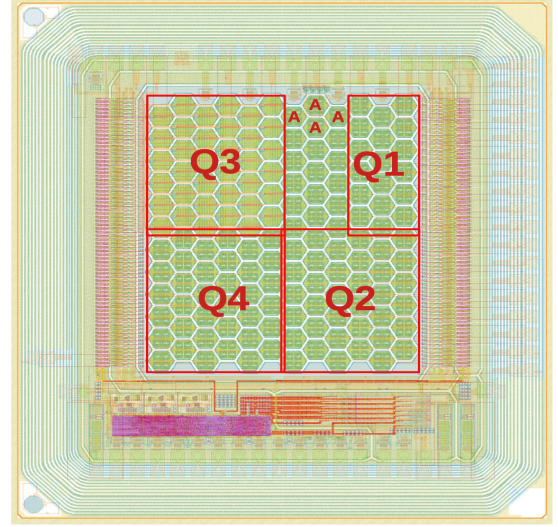


FIGURE 7.3 – Computerized representation of the pixels area divided in 5 distinct parts (Q1 to Q4 and A). A is the analogue matrix used during the measurements.

which results in a depletion layer  $\vec{W}$  in between. This one is partial even on the very thin epitaxy layer and so the collected amount of charges is small. The charge collection is made on the pixels (which are diodes) from the epitaxial layer and happens through drift and diffusion of the carriers. The pn-junction is the central point of silicon sensors. It creates an electric field which counteracts the diffusion characterized by the *build-in* voltage  $V_{build-in}$  in the space charge region. An external high voltage (HV) is used to modify the depletion length (as presented in Section 5.5). An ionizing particle passing through the detector liberates a signal charge which is collected by the field and detected by the electrodes (the pixel area). The build-in field collects the signal charge but also suppresses the leakage current, which is an important noise source [5].

While a small pixel size is the prime requirement to achieve a high spatial resolution, its exact geometries can be different. There are two types: square and hexagonal (presented on the left size of Figure 7.4). Both have their own particularities, however, a hexagonal geometry has the advantage that at most three pixels touch in each corner. The deposited signal charge is therefore shared between three pixels only and so more charge is left per pixel as compared to the squares form [5]. In the case of a hexagonal pixel, the amount of current will be less dense on corners than for a square pixel. This is due to the opening angle which is 120 degrees for a hexagonal pixel and 90 degrees for a square pixel. This geometry avoid a too high current in the corners and prevents a premature breakdown ensuring a stability and a uniformity of the electric field distribution across the whole junction area.

To achieve to a high spatial resolution, a second argument as to be mentioned. Indeed, the size of pixels should be minimised leading to an inter pixel spacing reduced to the strict minimum but, as the sensor is a pn-junction, the point of maximal electrical field is in the

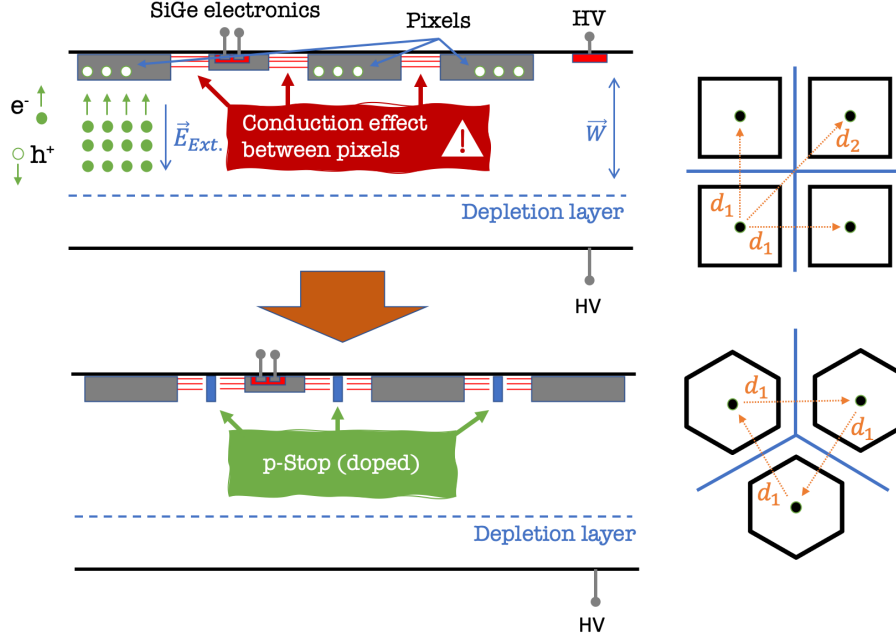


FIGURE 7.4 – On the left side: Schematic representation of the monolithic pixel detector with its depleted region  $\vec{W}$ , the pixels and the SiGe electronics are presented with the grey rectangles on the top. Some p-Stop doped areas have been introduced between the pixels in order to suppress conduction effect in between. Right side: representation of two kind of pixels geometry. On the top, the squared one and on the bottom the hexagonal one. The distance between the electrodes (represented with black centered points) is smaller in hexagonal geometry which allow a better optimization of the surface.

lateral border of the pn-junction leading, on corner to the conduction effect mentioned previously, because of the fact that the substrate is at a potential HV (which can goes to 160 V) value while the the pixels are at a potential value of 1.8 V. This difference can leads to this conduction effect but also, depending on the electric field, to the breakdown. To avoid this, a p-doped material (such as boron for example) is added in order to block the conduction in between and to cancel the *cross-talk* effect. This p-doped material is called a p-stop and it is at a potential of -30 V. On the surface, a stable difference of 30 V is made between the hexagonal pixels and the p-stop to reduce the current in corners and avoid breakdowns. The right panel of Figure 7.4 represents the two kinds of pixel shapes. All inter pixel areas contain a p-doped substrate. The left side of 7.4 shows a typical cross-section of a monolith silicon pixel detector containing p-stop between pixels. Concerning the thickness length of the sensing part, the chip studied has a sensor of 60  $\mu\text{m}$  depth. In Section 3.2, it was stated that an electron passing through a silicon sensor loses 0.3-0.4 KeV by micrometer so in that case, the energy lost by a particle would be 60 times that range which is equal to 18-24 KeV<sup>[c]</sup> for this thickness. The electrons emitted by the  $^{90}\text{Sr}$  cross the chip. Note that this is representing a situation with a total depletion length, however, the ATTRACT prototype has a 20-30  $\mu\text{m}$  depleted region.

<sup>[c]</sup> These values represent the energy particle and not the amount of energy measured in the experiment.

## 7.2 Stabilisation of a transistor by reaction of the collector

When a transistor operates for an extended period, its amplification parameter  $\beta$  is affected by external factors, such as the increase of the temperature inside it and by radiation. In the first case,  $\beta$  increases, while in the second, it decreases.

The effects of the temperature on  $\beta$  can be understood by using the relations  $I_C = \alpha I_E$  and  $I_B = (1 - \alpha)I_E$  presented in Section 6.3 leading to the equation 7.1 [44].

$$I_C = \beta I_B = \frac{\beta}{1 + \beta} I_E \Rightarrow \beta = \frac{1}{\frac{I_E}{I_C} - 1} \quad \text{with} \quad I_E \propto e^{\frac{V_{BE}}{V_T}} \quad V_T = \frac{K_B T}{q} \quad (7.1)$$

So when  $T \nearrow$ ,  $I_E \searrow$  and so  $\beta \nearrow$  (leading to  $I_C \nearrow$ ). Another point related to the last item in parenthesis has to be taken into account. The fact that the higher the collector current, the higher will be the energy dissipated in the form of heat, increasing the internal temperature. It is easy to understand that a loop is created which can lead to the destruction of the transistor. However, the opposite is true for radiation, have a lowering effect on  $\beta$  and decreasing the gain of the transistor. Bipolar transistors are mostly affected by the buildup of charge and the displacement damage generated by defects in the semiconductor lattice. These have accumulated due to the exposure to high-energy particles, mostly as a result of the decrease of the minority-carrier lifetime in the transistor base. In Section 6.3,  $\beta$  was defined as the remaining time  $\tau_r$  of a hole in the base, over the travelling time  $\tau_r$  for an electron from the emitter to the collector [45] [46] ( $\tau_r \searrow$  so  $\beta \searrow$ ).

To operate, a amplification transistor has to be in its linear regime. This means, to keep the *Base - Emitter* junction open (forward biasing) and the *Base - Collector* closed (reversed biasing) in the way to maintain the *transistor effect* as explained in Section 6.2. If the transistor switches to its saturated regime, it implies an opening of the junction *Base - Collector* which is not good, due to the fact that the relation  $I_C = \beta I_B$  is no longer verified. In this case, the transistor can not amplify as required.

While  $\beta$  has a very high influence on  $I_C$ , a way to suppress the fluctuations of  $\beta$ , is to make the polarisation of the transistor automatic by reaction of the collector. It can be seen as an automatic regulation of  $\beta$  with a new resistance  $R_b$  added between  $R_c$  and the electrode of the base, as presented in Figure 7.5. Since this method is cheap in components and prevents any variations of  $I_C$ , it is used in the transistors of the ATTRACT prototype.

Assuming that  $I_C$  increases (decreases) for some reasons, using Figure 7.5, the following small developments easily show how a transistor, by reaction of the collector, is stabilised <sup>[d]</sup> :

$$I_C = \beta I_B \quad \text{if} \quad \beta \nearrow (\searrow) \Rightarrow I_C \nearrow (\searrow) \quad (7.2)$$

<sup>[d]</sup> The demonstration is made with the increase of  $\beta \nearrow$  but also with its decrease  $\beta \searrow$  in parenthesis.

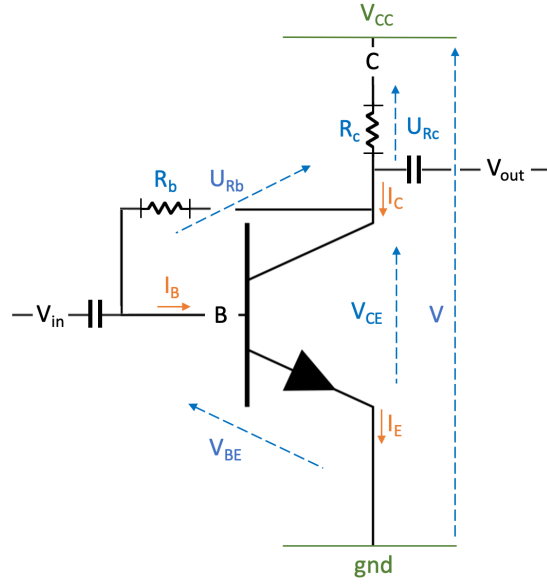


FIGURE 7.5 – Current polarisation of a npn transistor. A resistance  $R_b$  has been added between the collector and the base. This generate an automatic regulation of the increase or decrease of  $\beta$  due to the increase of the temperature and/or radiations.

$$U_{Rc} = R_C I_C \quad \text{if} \quad I_C \nearrow (\searrow) \Rightarrow U_{Rc} \nearrow (\searrow) \quad (7.3)$$

While the LVPS is equal to  $V_{CC} = U_{Rc} + V_{CE}$  and the fact that the LVPS,  $V_{CC}$ , remains constant <sup>[e]</sup>  $V_{CE}$  decreases (increases).

$$V_{CC} = U_{Rc} + V_{CE} = \text{fixed} \quad \text{if} \quad U_{Rc} \nearrow (\searrow) \Rightarrow V_{CE} \searrow (\nearrow) \quad (7.4)$$

Assuming that  $V_{BE}$  is quite stable and lower than  $V_{CE}$ :

$$U_{RB} + V_{BE} = V_{CE} \quad \text{if} \quad V_{CE} \searrow (\nearrow) \Rightarrow U_{RB} \searrow (\nearrow) \quad (7.5)$$

$$U_{RB} = R_B I_B \quad \text{if} \quad U_{RB} \searrow (\nearrow) \Rightarrow I_B \searrow (\nearrow) \quad (7.6)$$

$$I_C = \beta I_B \quad \text{if} \quad I_B \searrow (\nearrow) \Rightarrow I_C \searrow (\nearrow) \quad (7.7)$$

In other words, the system regulates itself. No saturation or sub-regime are possible anymore.

As  $I_C = \beta * I_B$  and  $I = I_B + I_C$ , by applying Kirchoff's voltage law in the input law we can calculate  $I_B$ :

<sup>[e]</sup> The LVPS,  $V_{CC}$ , is a fixed value configured outside of the chip with an external generator so it can not change.

$$V_C = V_{CC} - U_{R_c} = V_{CC} - I_C R_C = V_{CC} - \beta I_B R_C \quad (7.8)$$

Using the Figure 7.5 :

$$V_{CC} = U_{R_c} + V_{CE} = U_{R_c} + U_{R_b} + V_{BE} \quad (7.9)$$

$$V_{CE} = U_{R_b} + V_{BE} \quad (7.10)$$

$$V_{CE} - V_{BE} = U_{R_b} = R_b * I_B \quad \Rightarrow \quad I_B = \frac{V_{CE} - V_{BE}}{R_b} \quad (7.11)$$

Replacing  $I_B$  in equation 7.9 with the result of equation 7.11 the equation (7.12) below can be obtained:

$$V_{CE} = V_{CC} - \beta \frac{V_{CE} - V_{BE}}{R_b} R_C \quad (7.12)$$

Having control of the current passing through  $R_b$  (called feedback current) allows us to avoid the  $\beta$  variations but also to characterise the response of the transistors. Equations 7.11 and 7.12 show that varying the value of  $R_b$ , the current  $I_B$  (and so  $I_C$ ) can be controlled and the  $V_{CE}$  too and so the behaviour of the transistor, for example, when it is in an amplification mode.

On the ATTRACT prototype, an external current named the *feedback current* can be used to control the resistance  $R_b$ . In reality and without entering into details, this resistance is produced by using a N-MOS transistor <sup>[f]</sup> which is operated as a configurable resistor letting the current flow only above a certain value.

## 7.3 The amplifier

The output of the sensor is directly connected to a Common Emitter Amplifier transistor which is the one shown in Figure 7.5.

In amplifier mode, the transistor behaves as a current amplifier but, in the experiment, it is more convenient to manipulate voltages, to do this resistors are placed in order to convert these currents into voltages.

Using Figure 7.5,  $V_{out}$  can be calculate as a function of  $V_{in}$  and a amplification factor is deduced. Starting from the LVPS ( $V_{CC}$ ):

$$V_C = V_{CC} - U_{R_c} = V_{CC} - R_c I_c = V_{CC} - R_c \beta I_b = V_{CC} + V_{out}$$

$$V_B = V_{in} + V_{BE} = I_B h_{ie} + V_{BE}$$

The amplification factor can be now calculated:

---

<sup>[f]</sup> source: lesson and discussion with Lorenzo Paolizzi.

$$Amp = \frac{V_{out}}{V_{in}} = \frac{-R_c \beta I_b}{I_b * h_{ie}} = \frac{-R_c \beta}{h_{ie}} \quad (7.13)$$

Where  $h_{ie}$  is the input impedance. It can be assimilated to a resistor placed in parallel with the input stage which receives the signal transmitted to it. The higher this resistance is, the more it will oppose the passage of the signal and the more it will keep part of the signal. As explained in Section 6.3,  $\beta$  is the gain factor and, for the most common transistors used in amplification, it varies from 110 to 460 but in the ATTRACT model,  $\beta$  is more in a range of 10-20.

The LVPS ( $V_{cc}$ ) is injected as a constant value in the system. Each signal coming in the input of the amplification transistor will make a fluctuation of  $V_C$ . This variation will be *amplified* and so the fluctuation generates a potential difference where it generates an output signal which will have an opposite sign and a greater amplitude.

The resistance  $R_C$  is similar to a resistance  $R_B$  and is produced by using a P-MOS transistor <sup>[g]</sup> which is operated as a configurable resistor. This transistor is controlled by an input base current which is called *the preamplifier current*. Being able to control it will establish the response behaviour of the front-end.

## 7.4 Capacitors

In electric circuits, capacitors are used for many different kinds of applications, for example, to store electrical charges, to block DC components, to bypass AC components, to filter unwanted signals, to soften the electrical impulses, to obtain a uniform flow, and so on. Two main applications of capacitors are called *Coupling capacitors* and *Bypass capacitors*.

In electronics, coupling capacitors are connected in series. They are used in analogue circuits to block low frequencies signals and let the higher ones pass. They generate a direct current (DC) isolation from the voltages. In the Front-end, they are used before and after the transistor as shown in Figure 7.5 (named  $C_{in}$  and  $C_{out}$ ). Unfortunately the action of capacitor depends on the frequency of the signal passing through it, so it can affect the bandwidth of the amplifier transistor. Coupling capacitors are very useful in amplification circuits because, firstly, passing in before to reach the transistor will avoid interference with the transistor's bias voltage and so introduce some noise. Secondly, it reduces the signal by cutting it at its base, so deleting all the small "fluctuations" and lowering the noise.

Decoupling capacitors are used in parallel, as shown on Figure 7.6. In some electrical circuits, the sensibility to voltage spikes is very high. Fast voltage changes can reduce the performance of the circuit so decoupling capacitors are used to store the energy. If a signal drops, the decoupling capacitor can provide a sufficient amount of energy to maintain a

---

<sup>[g]</sup> source: lesson and discussion with Lorenzo Paolizzi.

stable voltage supply . On the other hand, if the signal rises very fast, the capacitor will absorb a certain amount of energy to keep the voltage supply stable. Another useful aspect of decoupling capacitors is that they allow direct current component (DC) to pass while alternative current (AC) component are redirected to the ground. This method is used to absorb AC noise and so produce a cleaner DC signal.

## 7.5 Drivers

As it has been previously shown, that the signal appearing as an input in the amplification transistor, will have an opposite sign and a bigger amplitude. But this signal is still not measurable on an oscilloscope. This comes about for one specific reason.

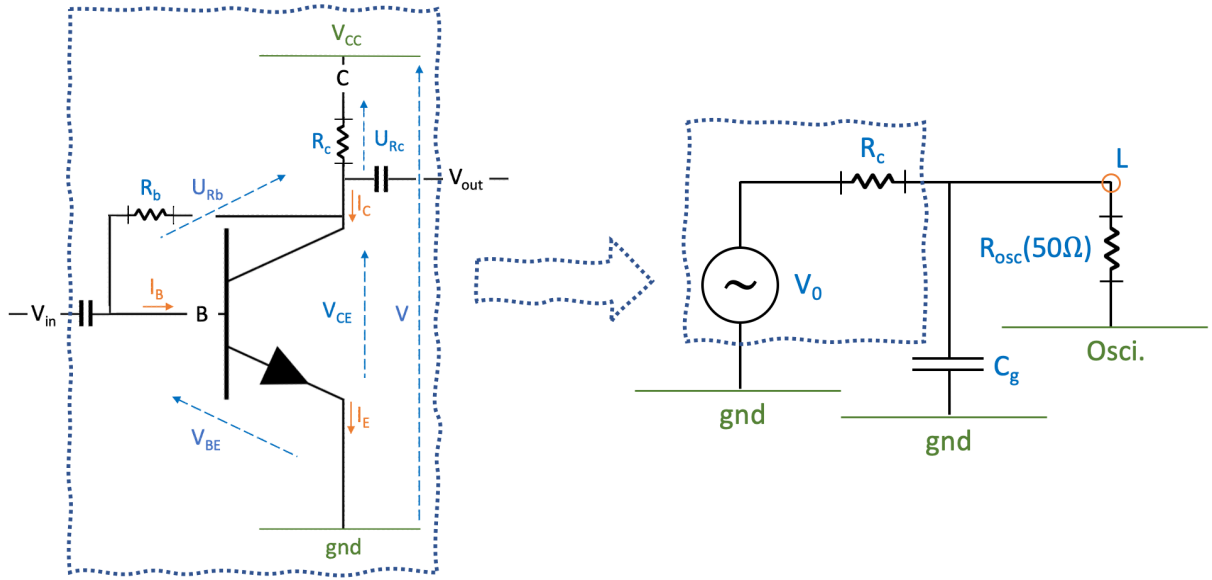


FIGURE 7.6 – *Left side: representation of the preamplifier which is the first stage of the front-end circuit. Right side: a situation representing the preamplifier directly connected to the oscilloscope. In this case, the signal will be too low to be readable. The solution will be to add two drivers.*

In Figure 7.6, the previous amplification transistor (on the left side) can be seen as a generator and the explicit resistance  $R_C$  (on the right side). On the Front-end of the ATTRACT prototype, the explicit value for  $I_C$  is in the range of  $150\mu A$  while the one for  $U_{R_c}$  is in the range of  $0.8V$  so  $R_C > \frac{0.8V}{150\mu A} \approx 5k\Omega$ .  $R_{oscilloscope}$  which represents the resistance inside the oscilloscope used to take the data and its value is  $50\Omega$ . A small calculation to obtain the potential at the point L can be done:

$$V_{Out} = U_{R_c} + U_{R_{Osc}} = R_C I_0 + R_{Osc} I_0 \quad \Rightarrow \quad I_0 = \frac{V_{Out}}{R_C + R_{Osc}} \quad (7.14)$$

$$V_{Osc} = R_{Osc} I_{Osc} = V_{Out} \frac{R_{Osc}}{R_C + R_{Osc}} \quad (7.15)$$



$$\frac{R_{Osc}}{R_C + R_{Osc}} = \frac{50}{5000 + 50} \approx 0.01 \quad (7.16)$$

As equation 7.16 shows, the input potential in the oscilloscope is equal to 1/100 times the output potential  $V_{Out}$  which is incoming from the amplification transistor. Let us say that this signal is not readable!

The idea overcome this problem, is to add a Common Collector transistor. For the chip test, the external current controlling the resistance of this new transistor is added and it is called  $I_{driver}$ .

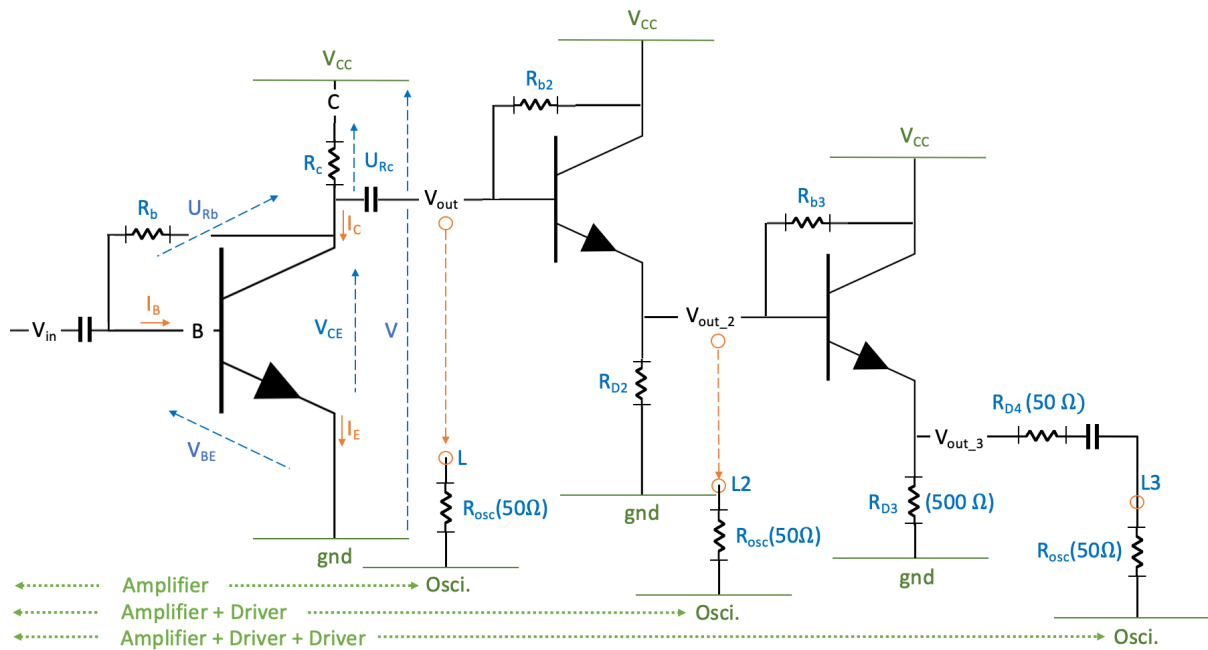


FIGURE 7.7 – Schematic representation of the front-end on the ATTRACT prototype. The incoming signal passes through three transistors (one amplifier and two drivers) to be readable on the oscilloscope.

Figure 7.7 may help in understanding this. It can be divided into three sub-circuits as described by the green arrows at the bottom. The first one, is the one called the *preamplifier* and is the same circuit as shown in Figure 7.6, on which the steps calculated, from equations 7.14 to 7.16, are applied.

Now if a driver transistor is added to the amplifier (sub-circuit Amplifier + Driver of Figure 7.7), the output signal will be enough to be readable on the oscilloscope.

## 7.6 Assembly

The measurement of the time resolution required to use a Low Gain Avalanche Diode (LGAD) detector. Its role was to provide a reference time. The LGAD was glued onto a



specially designed amplifier board which is shown in blue on Figure 7.8. The same board has a hole under the LGAD with a width of 1 mm in order to allow electrons from a  $^{90}\text{Sr}$  source to reach the second chip which is the ATTRACT prototype in a such way to measure the TOF between them.

Figure 7.8 presents the assembly of the Time resolution measurement. From the left to the right, the source  $^{90}\text{Sr}$ , the blue LGAD reference board and the green ATTRACT board.

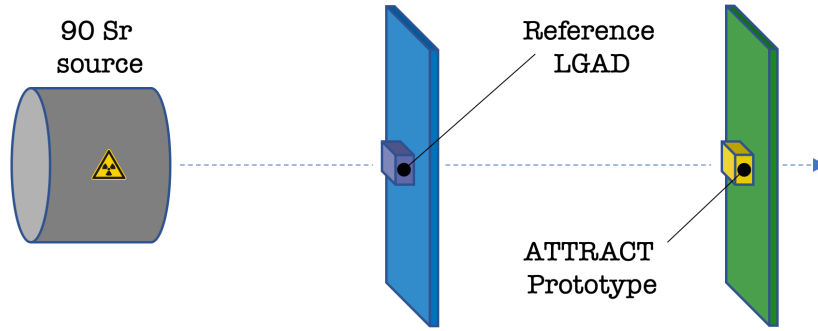


FIGURE 7.8 – Representation of the assembly configured for the time resolution data taking. From the left to the right, the  $^{90}\text{Sr}$  source in its protection, the LGAD board with a 1 mm hole on the bottom of the LGAD and the ATTRACT prototype board. The three component are aligned on a straight line.

# Chapter 8

## Experimental setup

The different experimental instruments used during the measurement are presented in Figure 8.1. From the right: the computer, the shield protection, the oscilloscope, an source controlling the LVPS and two Keithley AC current sources. The one above is used to generate the High Voltage. The computer allows set-up of the preamplifier, feedback and driver Bias <sup>[a]</sup> and also to mask or unmask pixels. The oscilloscope is a Lecroy Teledyne SDA-820ZI-B having a Bandwidths from 4 GHz to 30 GHz with a sample rate of up to 80 GS/s but set to 40 GS/s (GS/s represents Giga Sample by second).

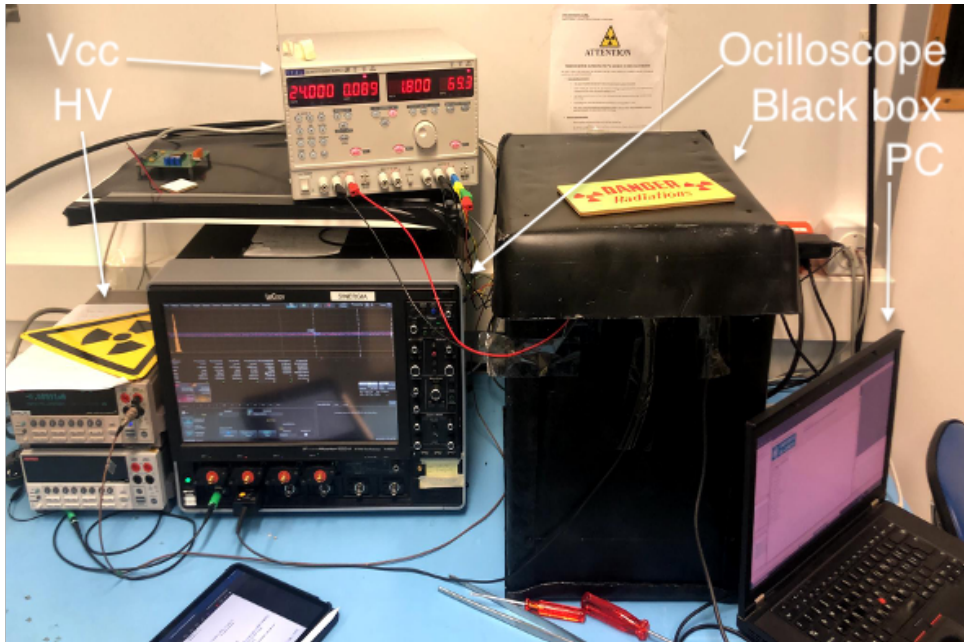


FIGURE 8.1 – Working station. From the right to the left: A computer allowing to the set-up of the FPGA and mask the pixels. A shield protection (called black box) with inside the ATTRACT prototype and the FPGA board, a Lecroy oscilloscope allowing the analysis of the shape of the output pulses and some generators, which sets-up the LVPS and the high voltage HV.

Figure 8.2 shows the components inside the shield. The right side shows the main board and its processor FPGA (e.g. a field-programmable gate array) which is an integrated circuit designed to be configured after manufacture. The left side shows three superimposed elements as explained in Section 7.6. The transparent container contains the source. As the  $^{90}\text{Sr}$  source is a beta decay, Plexiglas or plastic is sufficient to seal it. Below, the

<sup>[a]</sup> They are related to the pseudo-resistances introduced in the transistors.

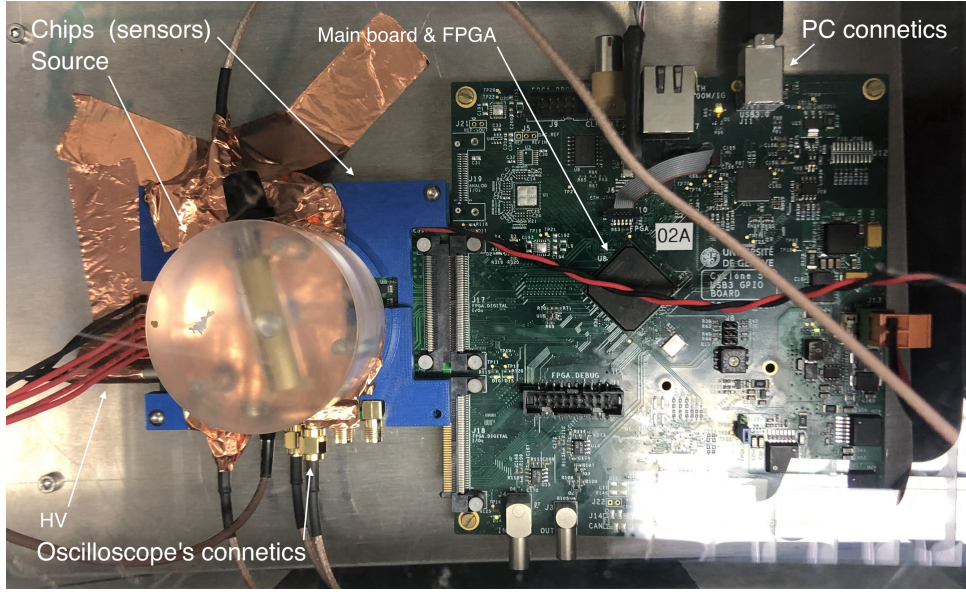


FIGURE 8.2 – *Layout of the boards inside the shield. From the right to the left: The mainboard and its FPGA, the transparent  $^{90}\text{Sr}$  source container, the blue structure fixed to the ATTRACT prototype board. An LGAD is fixed to the blue structure in between.*

blue layer is fixed to the ATTRACT prototype board. This blue structure hide an LGAD positioned between them. The visible copper bands prevent electrical overloads. As explained on the previous section, the output signals (form the LGAD and the ATTRACT prototype) are sent to the oscilloscope via coaxial cables. That kind of cable is used in order to minimize the dispersion of the signal, in frequency.

## 8.1 Unige GPIO

The solution implemented to control the ATTRACT prototype is to use a GPIO (General Purpose Input-Output) developed by the University of Geneva called the *Unige GPIO*. As mentioned on Chapter 7, the ATTRACT prototype chip is connected to the GPIO port which makes the connection to the FPGA. The FPGA used is an *Altera cyclone V*. An additional Guide User Interface (GUI) is dedicated to manage its configuration as well as the ATTRACT prototype one. A *High Speed USB 3.0 Cable - A-Male to B-Male* links the whole to the computer.

Three tabs of the GUI have been used during the whole experiment: the board tab, the SIDE0 and the SPI tabs. They are shown on Figure 8.3. The *board* tab controls the DAQ (data acquisition) start and stop, as well as sending direct parameters such as the possibility to enable the chip, send a clock or enable an external trigger. The connection and the USB parameters with the FPGA are also configured in this window. The table *Side0* is a matrix that allow the masking of pixels , 0 and 1 which represent the enabled and disabled state. In the data tracking, only the first 3 analog pixels where unmasked. The last tab *SPI*, controls the value of each DAC current needed to make the ATTRACT prototype work, such as the three currents used in the measurements which are, as a

reminder, the preamplifier DAC current <sup>[b]</sup>, the feedback DAC current and the driver DAC current.

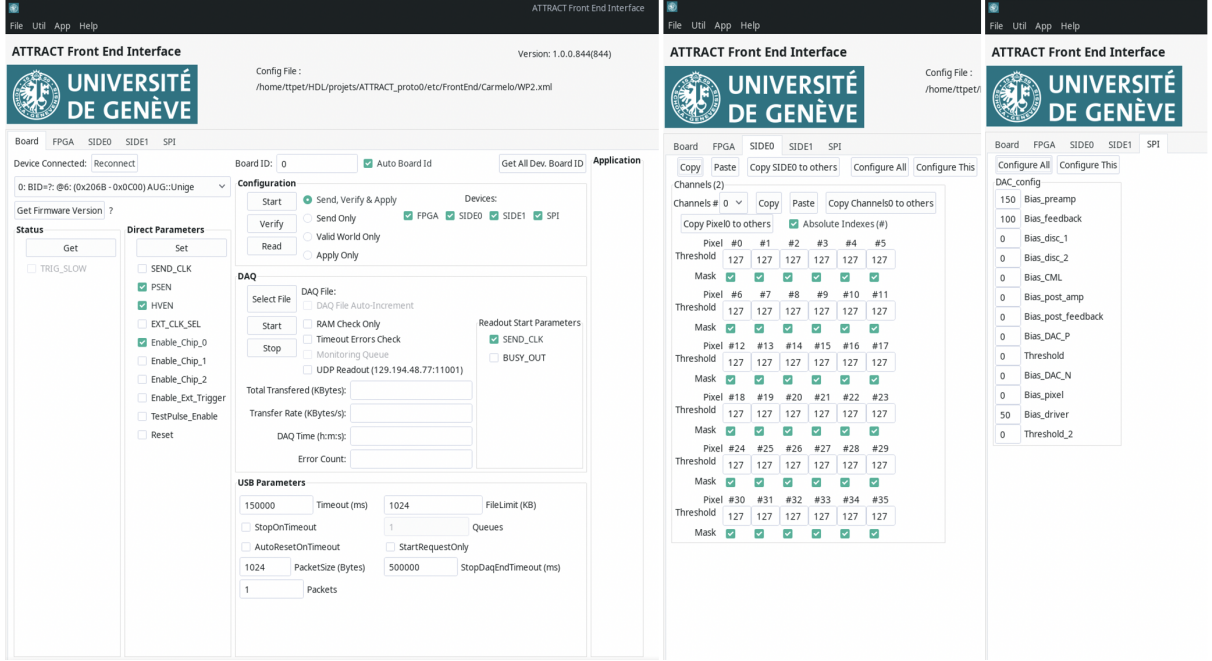


FIGURE 8.3 – Presentations of the three windows used in the GUI to configure the FPGA as well as the pixels masks. The first tab is useful for the connection, the second for the selection of the activated pixels in use while the third is where the various DAC currents are set.

## 8.2 DAC settings

A Digital to Analogue Converter (DAC) is used (via the FPGA) to control the current flow in the different elements of the chip. These currents are very precisely injected and influence the performances of the chip and this is why they have to be set to the correct values. A summary of the DAC currents relevant for this project with their setting are presented in table 8.1.

The *code* values are the ones introduced in the DAC\_config panel on the SPI tab of the GUI. Each of the three bias depends on its own *code* value (which is between 0 and 255) and the  $I_{bias}$ . The  $I_{bias}$  current depend on  $I_{PAD}$  which is the main source of current for all the bias. A value of  $I_{PAD} = 50 \mu A$  is set-up in this measurement leading to  $I_{bias} = 1 \mu A$ . As example, a value of code = 125 DAC will result on a  $I_{feedback} = 7.81 \mu A$ ,  $I_{preamp} = 125 \mu A$  and  $I_{Driver} = 250 \mu A$ . In this configuration 1 DAC for the bias\_preamplifier is equal to  $1 \mu A$ . As shown on Figure 8.3, the *code* value for the three DAC currents used can be different from each others.

<sup>[b]</sup> The preamplifier DAC current refers to the current injected in the pseudo-resistance inside the amplification transistor.

Name	parametrisation	function
bias_feedback	$I_{bias} \times \text{code} / 16$	Stabilisation of a transistors
bias_preamplifier	$I_{bias} \times \text{code}$	Amplifier <i>resistance</i>
bias_driver	$I_{bias} \times \text{code} \times 2$	Driver <i>resistance</i>
code	$\in [0, 255]$	binary instance
$I_{bias}$	$I_{PAD} / 50$	main controlling current

TABLE 8.1 – Overview of the DAC values for the front-end of the ATTRACT prototype.

### 8.3 Lecroy oscilloscope

To analyse a pulse, a *Lecroy* scope is used. Inside the scope, the input signal passes through several components before it is displayed on the screen. Figure 8.4 presents this process. From the left to the right, these components are a front-end signal conditioning circuitry whose the main job is to scale and filter the analog input signal before it goes to the analog-to-digital converter (ADC). It will also store the signal's amplitude. The ADC component and the acquisition processing catch the signal and convert it into a binary form while, depending on the trigger state, the waveform memory will or will not store in a local storage or leave it in the RAM. The last component displays the pulse on the scope's screen [47].

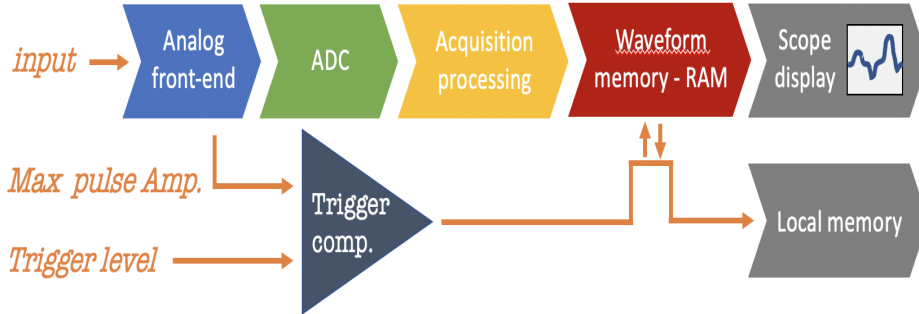


FIGURE 8.4 – Schematic representation (step by step) of the operation of the oscilloscope.

#### 8.3.1 The potential resolution

The difference between an analog signal and a digitised signal is the fact that "analog" quantity changes continuously over time while a "digital" quantity has discrete values over time. By discrete values, it is assumed that for a 8 bits ADC, the vertical scale (by vertical, the voltage axis is taken into account) is divided in  $2^8 - 1 = 255$  divisions and each of them is represented by a 0 - 1 bit state [48].

For a better understanding of this, Figure 8.5 and 8.6 represent the process with an oscilloscope having a 2-bits ADC component, the scope's vertical scale goes from 0V to a  $V_{ref}$  of 4V and the measuring signal is assumed to be in between. Figure 8.5 represents



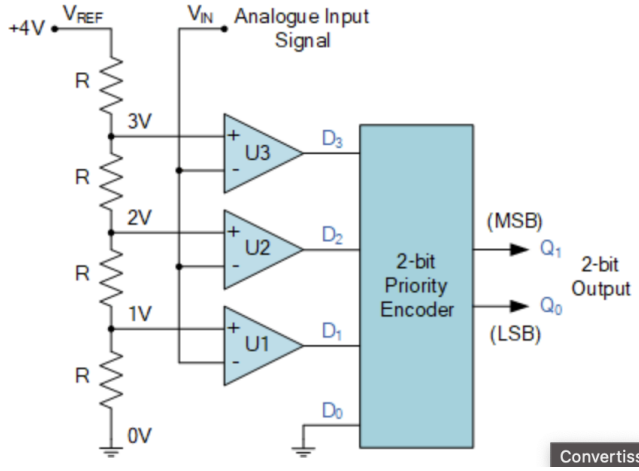


FIGURE 8.5 – Diagram representing the operation of the vertical scale signal acquisition. An input signal (assumed to be between 0 and 4V) is represented with  $V_{in}$ . Three comparators at three different levels, work in binary mode to state the amplitude of the input signal before it is encoded in a 2-bit output (for this example, but in reality  $2^8$  bits are used).

Analogue Input Voltage ( $V_{IN}$ )	Comparator Outputs				Digital Outputs	
	$D_3$	$D_2$	$D_1$	$D_0$	$Q_1$	$Q_0$
0 to 1 V	0	0	0	0	0	0
1 to 2 V	0	0	1	X	0	1
2 to 3 V	0	1	X	X	1	0
3 to 4 V	1	X	X	X	1	1

FIGURE 8.6 – Table representing the encoding as a function of the comparator outputs. Different amplitudes of the input signal are presented.

the electrical diagram which is composed of four resistances called  $R_1, R_2, R_3, R_4$  with the same Ohm value. The triangular form represents logical comparators ( $U_1, U_2$  and  $U_3$ ) and the rectangular one, a 2-bit binary encoder. A voltage input  $V_{in}$  signal is applied to one input of the comparators, while a reference voltage a  $V_{ref}$  is applied to the other. Assuming that  $R_1 = R_2 = R_3 = R_4$ , the  $V_{ref}$  input of each comparators will be  $U_1 = V_{ref}/4$ ,  $U_2 = V_{ref}/2$  and  $U_3 = 3V_{ref}/4$ . Each of them compare the two input voltages and define a logic output state which is 1 if  $V_{in} > U_i$ , otherwise 0, represented by  $D_1, D_2, D_3$  and  $D_4$ . When a signal reaches the ADC, it will be checked by the highest voltage comparator and if the signal voltage is lower than  $U_3$  it will go to the second comparator otherwise the analysis stops. Figure 8.6 represents the logical results of the comparators depending on the analog input voltage  $V_{in}$ . In this example, the encoder will encode the comparators results in a 2-bits binary sequence. Its results is also shown in the same table.

For a ADC with an output binary sequence of 8-bits,  $2^8 - 1 = 255$  comparators will be needed to process in the same way. The scope's voltage scale will be divided in 255 identical parts, having a size of  $0.0039 * V_{ref}$ .

### 8.3.2 The time resolution - sampling

A pulse is a continuous variation of  $V_{in}$  over time. An oscilloscope samples it. This means that a large number of data points are captured in one continuous record (blue squared points in Figure 8.7). Put in another way, this means that the time axis of the oscilloscope is divided in a number of identical intervals, called samples, which are caught. In the *Lecroy* oscilloscope used, the bandwidth extends up to 20 GHz (maximal

frequency until which a signal can be caught) and the sampling rate is up to 80 GSa/s<sup>[c]</sup>. A frequency of 20 GHz implies a period of  $\cong 50$  ps, to be able to see a signal having that kind of frequency, the sampling rate has to be shorter. By its 80 GSa/s rate, the *Lecroy* scope is able to go up to  $\approx 4$  samples for the highest frequency so its ADC is extremely fast with a sampling rate faster than the frequency of the incoming waveform. With a sampling rate of 80 GSa/s, the sampling interval will be about  $t_s = 12.5$  ps. The oscilloscope was configured to capture a pulse from the analog pixels 1,2 and 3 and a pulse from the LGAD with a time window of 200 ns.

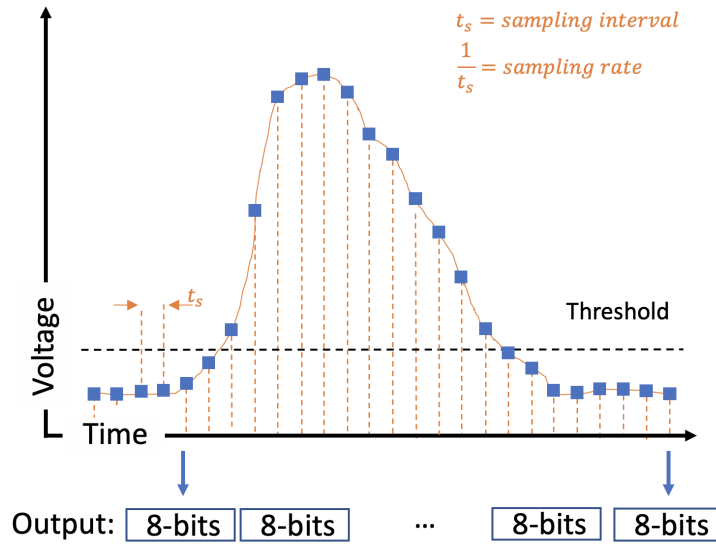


FIGURE 8.7 – Representation of the sampling process on the oscilloscope. The horizontal range used is a time window of 200 ns and a sampling of 40 GSa/s is used. All the samples are saved in a 8-bits encoding.

To summarise, the ADC converts each blue points in a 8-bits sequence and gives the result to the acquisition processing which combine the whole sequence of the pulse. If the result of the trigger comparator is positive, that means the pulse crosses the threshold and it has to be saved in a fast local memory and be display on the scope's screen<sup>[d]</sup>. In the case of this experiment, the sampling rate has been defined as 40 GSa/s<sup>[e]</sup>.

<sup>[c]</sup> These numbers come from the website of the constructor : <https://teledynelecroy.com/oscilloscope/wavemaster-sda-dda-8-zi-b-oscilloscopes/sda-820zi-b>.

<sup>[d]</sup> The scope has different display modes, the *auto* will show all the signals no matter if they are below or above the threshold, the *one-by-one* mode will allow the user to trigger only on upper signals and to change the displayed event only when he pushes the button. The last mode is the *normal* one, which is an automatic *one-by-one*.

<sup>[e]</sup> A rate of 80 GSa/s is usable only with two channels. By using four channels will reduce it twice to a rate of 40 GSa/s.

## 8.4 The LGAD

The Low Gain Avalanche Diode (LGAD) merges the best characteristics of traditional Silicon sensors with the main feature of Avalanche Photodiodes (APD), using n-in-p silicon diodes with a low and controlled internal multiplication mechanism [49]. The LGAD is used as a time reference for this measurement and has a time resolution of 50 ps RMS. A cross section of a typical LGAD is shown in Figure 8.8 [50].

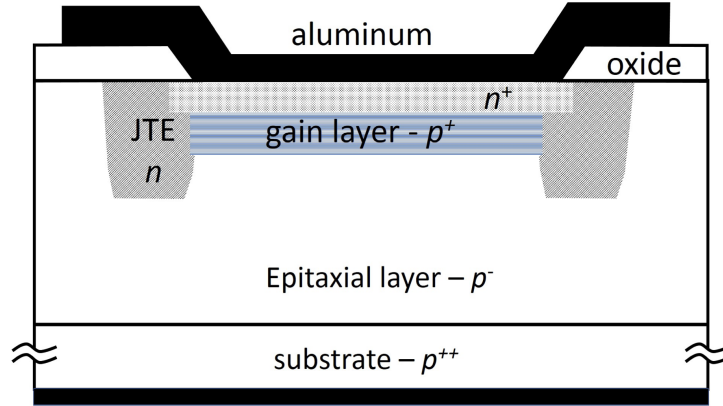


FIGURE 8.8 – Cross section of the LGAD used. A depleted region is visible between the  $n$ -doped and the  $p$ -doped interface. An additional  $p$ -doped layer is implanted just below the  $n^+$  layer which creates a gain layer. A Junction Termination Extension prevents a premature cylindrical breakdown and ensures a stability and a uniformity of the electric field distribution across the whole junction area.

The structure of the LGAD includes 4 layers. The active volume of the device is the epitaxial layer which can be a thickness of a few tens of  $\mu\text{m}$  in order to obtain a very low drift of the charge carriers. A p-n junction is created between the highly doped  $n^+$  cathode electrode and the p-doped substrate. In addition, p-doped layer is implanted just below the  $n^+$  layer which creates a gain layer. This gain layer is a doping process based on Boron, Gallium, Carbonated Boron and Carbonated Gallium to obtain a controlled multiplication mechanism <sup>[f]</sup> and allows the generated charges to undergo avalanche multiplication before being collected. A Junction Termination Extension (JTE) design made of a n-doped material overlaps the multiplication junction preventing a premature cylindrical breakdown and ensures a stability and a uniformity of the electric field distribution across the whole junction area [51].

An incident particle passing through the detector will produce electron-hole pairs which will drift towards the cathode and anode respectively. The maximum value of the electric field inside the device is located between the n-doped cathode and the p-doped multiplication electrode.  $\vec{E} \propto \sqrt{\text{p-type doping density}} \ \& \ \sqrt{\text{external bias voltage}}$  (for a bias voltage significantly higher than the built-in potential) [52]. An amplification effect of the signal is observable in the range of 10 to 20 times. The resulting current pulses are

<sup>[f]</sup> The reader can be referred to [49] to have information about the different advantages of these selections.



intrinsically fast and can compensate a limited amount of charge released by a MIP in the thin substrate. Keeping the gain value below the avalanche regime keeps the noise low and increases the signal to noise ratio. In the next chapter, the Equation 9.1 will present the time resolution due to the jitter as  $\sigma_t^{jitter} = \frac{\sigma_V}{dV/dt}$  with  $dV/dt$  the slope (V representing the voltage signal amplitude) and  $\sigma_V$  the r.m.s time resolution. To minimize  $\sigma_t$  low-noise and fast signals are needed.

# Chapter 9

## Signal processing for precise timing measurement

### 9.1 Signal characteristics

Once the signal is shaped, it will be possible to extract some information characterising its behaviour such as its amplitude, its Time-Of-Arrival ( $TOA$ ) and its Time-Over-Threshold ( $TOT$ ). Also information about the noise can be obtained such as the  $RMS$  noise (as explained in Section 6.5) and the maximal value of the noise which is represented with the *Noise limit* blue line in Figure 9.1.

If the pulse has a relatively large amplitude, it will pass through a threshold trigger level and activate the signal storage as presented in Section 8.3.

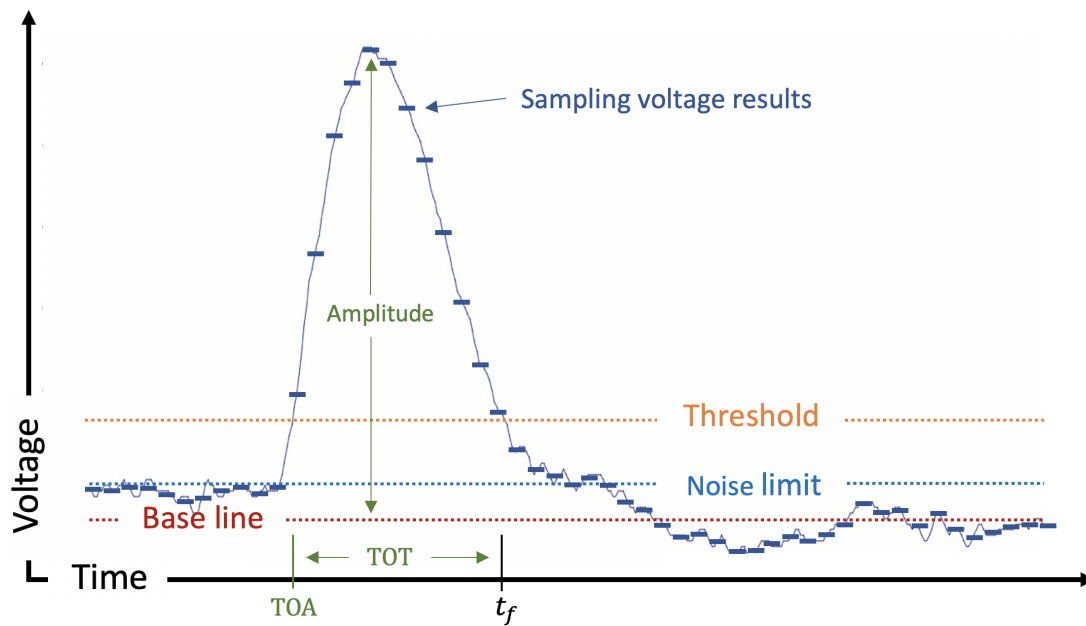


FIGURE 9.1 – Characteristics of the digital pulse of the signal created by the particle's ionisation. Some information can be obtained characterising its behaviour, such as its amplitude, its Time-Of-Arrival ( $TOA$ ) and its Time-Over-Threshold ( $TOT$ ) but also the  $RMS$  and the maximal value of the noise.

The red *Base line* represents the mean value of the noise while the orange line represents the threshold configured on the oscilloscope. The amplitude is measured from the *Base line* to the maximum value sampled.

As explained in Section 8.3.2, the oscilloscope's time window was configured at 200 ns. Since the oscilloscope's sampling is temporised,  $t = 0$  s represents the initial temporal value of the first sampling and this means that the  $TOA$  is the time value for the first sample which has a potential value over the threshold, while  $t_f$  is the final time of the sample when the pulse goes back below the threshold. The time difference between them characterises the  $TOT$ . Section 10.1 will go into further detail by presenting several other variables used in the analysis that can be deduced from the main variables described here.

## 9.2 Time-Walk and jitter

If life was perfect, noise would not exist and the arrival time would be found with extreme precision and with zero error. Unfortunately, that is not the case. A lot of pulses show a non-negligible amount of noise coming from the sensor or electronics, generating an uncertainty for the time at which the signal reaches the threshold. This makes, at the end, a statistical fluctuation which can be, for example, easily observed on the pulse of Figure 9.2. The same Figure could easily represent the coincidence between a signal coming from the ATTRACT prototype and the other one coming from the LGAD. Of course, where the  $TOF$  has been subtracted.

Most of the time, pulses having the same shape but different amplitudes will cross the threshold value at different times resulting in a difference  $\Delta t$  between them. Figure 9.2 represents this situation.

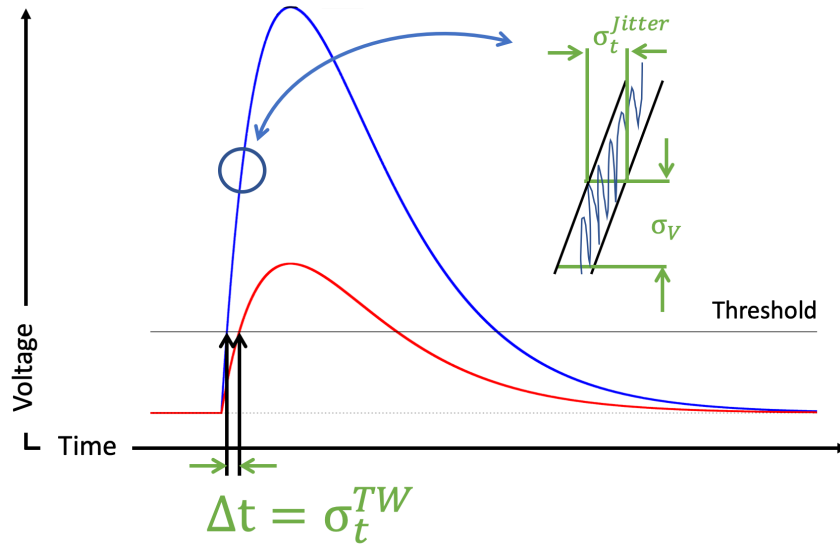


FIGURE 9.2 – Time-Walk representation for two pulses.

The Time-Walk is defined as a variation in time when a fixed threshold value is applied to signals with similar rise time but different height.

Another aspect of the noise observable in the pulse is the horizontal oscillations. This effect is called *Time Jitter* which represents a variation of the reconstructed signal time due to the noise on the amplitude. That is a real problem because if the noise on the Voltage axis is sufficiently large it will cross the threshold too early and it can cause a

false triggering (and so giving false values of TOT and TOA for example). Having a good signal over noise ratio can reduce a lot this source of noise. The mathematical expression is [53]:

$$\sigma_t^{jitter} = \frac{\sigma_V}{dv/dt} = \frac{A_{Gain}ENC}{A_{Gain}I_{ind}} = \frac{t_{rise}}{Q/ENC} = \frac{t_{rise}}{Signal/Noise} \quad (9.1)$$

Where  $\sigma_V$  is the noise related to the y-axis in each signal (vertical fluctuations).  $dv/dt$  is the slope and it can be calculated with  $(Amplitude_{80\%} - Amplitude_{20\%})/(risetime)$ .  $A_{Gain}$  represents the gain factor of a transistor. The signal to noise ratio can be obtain with the maximum of the amplitude of the pulse divided by the *RMS* noise. The first way to reduce the time jitter is to reduce the rise time, for example, using thin sensors and large gain (increasing the signal to noise ratio).

### 9.3 Resolution of a detector

As it has been explained in Section 5.6. when a particle ionizes a detector, charge carriers are generated which obey to a statistical law which contributes to a Gaussian enlargement of the total absorption peaks. In addition to this statistical component, as we have seen in Section 9.2 and 6.4 extra effects due to electronics and charge collection can induce another variation in the shape of the pulse recorded. This is a second cause of an enlargement in the initial signal. The performances of a detector can then be characterized by its temporal resolution which is represented by the full width at half maximum (FWHM) of the distribution of the difference of the *TOA* of the signals coming out from the two ships (ATTRACT prototype and LGAD) and readable on the oscilloscope.

# Chapter 10

## Analysis method

The data analysis process is divided in three parts. The first part is a conversion of the binary files saved by the oscilloscope in *Root* files. The second part is called the *pre-analysis* with the objective of finding the highest and the lowest efficiency configuration, these will be called "operating working points (WP)". A scan of the Feedback bias is made as a function of different values of the preamplifier DAC bias. Once the two WP are found, a time resolution analysis will be done in the third part, with some amplitude corrections.

### 10.1 Binary conversion

The data collection has been performed in terms of *runs*. Each time a measurement is done, a run is completed. For each of them, the oscilloscope saves the data in binary sequence called a trace file, as explained in Section 8.3. One *trace* file correspond to 200 events detected (crossing the threshold). So one run represents 20'000 events which are about 100 *traces*.

The binary conversion is a script which converts all the *trace* files of a run in one unique *Root* file. This *Root* file contains all the event's properties. The properties used for describing a pulse are listed below, with, in parenthesis, their acronyms which will be used in the rest of this thesis :

- Threshold (Thr)
- Pulse amplitude (Amp)
- Time at 20% of the amplitude (Time\_20%)
- Time at 80% of the amplitude (Time\_80%)
- Signal Time of Arrival at custom fixed threshold (TOA)
- Signal Time over Threshold at custom fixed threshold (TOT)
- Maximum background (Max\_bck)
- Root mean square background (RMS\_bck)
- Voltage value as a function of the sample (Wave\_amp)
- Time as a function of the sample (Wave\_time)

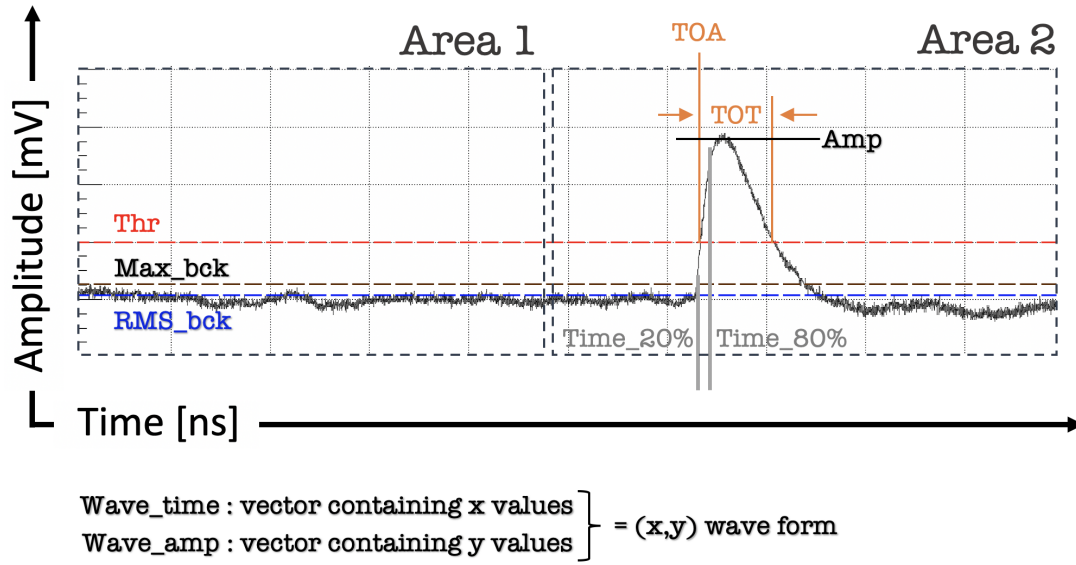


FIGURE 10.1 – An example of a signal saved by the oscilloscope. The different variables used for the analysis are shown, which are : the threshold set (*Thr*), the maximal value of the background noise (*Max\_bck*), the root mean square value (*RMS\_bck*), the time-of-arrival (*TOA*), the time-over-threshold (*TOT*), the amplitude of the pulse (*Amp*) and the times at 20% and 80% (*Time\_20%* and *Time\_80%*). The time window (of 200 ns) is divided into 2 areas. The first is used to determine the variable related to the noise, while the second, is used to determine the variables representing the impulsion of the pulse. The two "Wave\_X" variables contain the x-axis and y-axis coordinates of each points.

The last two parameters represent each pulse in terms of the time (on the x-axis) and the voltage's amplitude (on the y-axis). One example of an event is shown in Figure 10.1. The same Figure also describes each of the others parameters.

Figure 10.1 gives a first illustration of a correct event taken during the measurements. A pulse is divided in 2 Areas. The first, Area 1, is used to determine the maximum value (*Max\_bck*) and the root mean square of the background (as explained in Section 6.5). On the other hand, the second area, Area 2, is used to get the signal impulsion characteristic which are the value of the time-of-arrival (*TOA*), the time-over-threshold (*TOT*), the time when the signal is at 20% of its amplitude (*Time\_20%*) and when it is at 80% (*Time\_80%*).

## 10.2 Pre-analysis

Before starting the time resolution measurement, a scan of all the values possible for the different bias has to be done. This pre-analysis is made with the  $^{109}\text{Cd}$  source described in Section 3.1 which emits photons at constant energy of 22 keV and 25 keV which are relevant for this study. This source was used to measure the performance of the preamplifier and more generally to characterise the behavior response of the front-end. During this manipulation, a fixed value of 120V is set for the high voltage and the main goal is to set

different values for the preamplifier, driver and feedback DAC bias to obtain the behaviour of the chip response to these changes. This manipulation is very important because it allows the identification of the optimised working points for the time-resolution study. The variables studied during the pre-analysis are listed below:

- The Amplitude mV in terms of the Bias Feedback DAC.
- The rise-time ps in terms of the Bias Feedback DAC.
- The time-over-threshold ps (TOT) in terms of the Bias Feedback DAC.
- The equivalent noise charge [ $e^-$ ] (ENC) in terms of the Bias Feedback DAC.
- The ratio  $\frac{\text{Max noise}}{\text{RMS noise}}$  in terms of the Bias Feedback DAC.
- The signal-to-noise ratio in terms of the Bias Feedback DAC.

Each variable is studied in terms of the Feedback DAC bias and for different values of the preamplifier and driver DAC currents. The Feedback DAC vary from 10 DAC to 200 DAC. The preamplifier DAC takes values of 10, 20, 50, 100 and 200 DAC and the driver DAC will have two specific value of 200 DAC and 50 DAC. This manipulation will allow to define two opposite working points, one with a high and another one with a low, power consumption in such a way as to obtain the lowest and the highest resolution of the detector during the further studies of the time resolution.

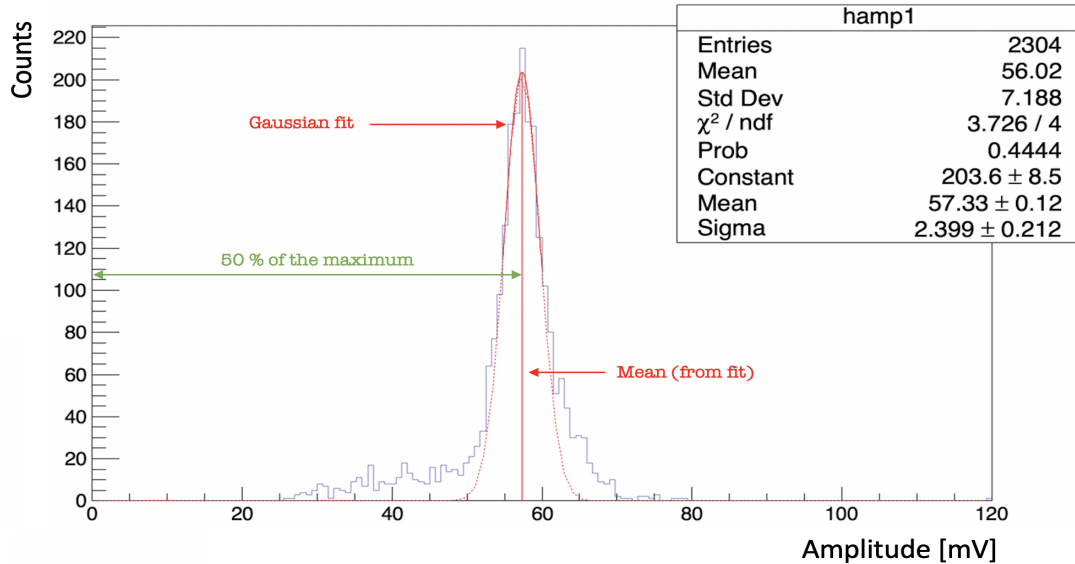


FIGURE 10.2 – An example of a statistical distribution following a Gaussian distribution for a specific configuration of the preamplifier, the feedback and the driver DAC currents. A fit at 50% of the amplitude has been made to obtain the mean of the distribution.

For each specific configuration (for the various DAC currents), a number of around 20,000 events is taken <sup>[a]</sup>.

A script has been done to make this process automatic. Once the conversion is done and the trace files are created, the script will import them and check each pulse separately. The checking is strongly related to the noise level and is explained in the next section, Section 10.3. Once a pulse is captured, the variables *Amp*, *rise – time*, *TOT*, *ENC*, *Max\_bck/RMS\_bck* and the *signal/noise* ratio are calculated. Statistically, not all the events have the same values for each variable. Pulse by pulse, histograms representing each variable is filled resulting in a statistical distribution. Figure 10.2 is an example of a result obtained for the variable *Amplitude* <sup>[b]</sup>. A Gaussian fitting is realised at 50% of the maximum of the distribution to obtain its mean. Once the mean of the distribution for each variable, at each configuration of current DAC values, has been found, the graphics listed above can be done. With these resulting plots, the two WP can then be defined for the next task, which is the time resolution analysis.

### 10.3 Events selection

As a reminder, in Section 4.4, three parameters were mentioned to have a negative and strong impact on the time resolution of a pixel detector. Since the first two (The reading geometry - weighting field and the charge collection noise) are supposed to be negligible in this experiment, only the electronic noise is present. As it has been described in Section 6.5, a *classic* noise is represented by a Gaussian distribution resulting in random oscillations <sup>[c]</sup> but it could happen that, for some reason, the noise of the output signal has a sinusoidal and cyclic behaviour before and after the signal's pulse. This effect comes from the fact that the signal noise is amplified by an intrinsic resonance of one (or more) electronic components inside the output front-end circuit shown in Figure 7.7. Figure 10.3 represents the two different situations. The signal on the left side is an ideal signal while the signal on the right side shows a cyclic amplification effect.

During the measurements, this effect happened at Bias preamp = 50 *DAC* (Bias feedback : 10, 20 , 50, 100 and 200) and Bias preamp = 100 *DAC* (Bias feedback : 10, 20 , 50, 100 and 200). The annex 14.1 shows a typical signal output for each value of bias feedback for these two values of bias preamplifier.

This effect has two important consequences. Firstly, making an analogy to the demonstration from Equation 7.2 to 7.2 related to the beta variation due to the radiation and temperature effects on the gain of a transistor. In the case of a transistor amplifying a signal, it is expected to see that the amplitude decreases as the bias feedback DAC increases but in these two series, that is not the case. Which is because the peak of the signal can be pushed up, if it is synchronised with the high peak of the sinusoidal oscillation. Secondly,

---

<sup>[a]</sup> Unfortunately not all the events are useful so in some examples or results, the reader will see that the number of entries is less.

<sup>[b]</sup> Since, the purpose of this chapter is to explain the methodology, no specific results are given here but are in the next chapter.

<sup>[c]</sup> By random, it is assumed that the noise oscillation before and after the peak has no repetitive cycles.



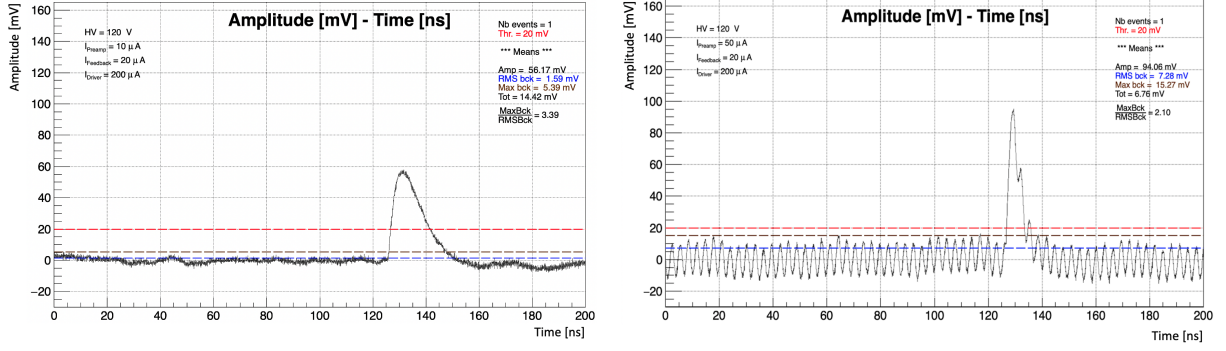


FIGURE 10.3 – Comparison between a correct signal catch and an oscillating signal. on the left side, the signal has random oscillation noise while on the right side, the signal is oscillating due to the DAC current configuration used and is very near an intrinsic resonance frequency of one (or more) electronic components which compose the output front-end circuit. The signal is amplified by it.

in Figure 10.3-left side, the oscillation effect generates typical spikes in the decrease part of the signal which has by consequence an extension in time of variables, such as  $TOA$  of  $TOT$  which can falsify the results for the measurement of the temporal resolution. It is interesting to mention that for some captured pulses, the amplitude of the oscillations was so important that the pulse was no longer distinguishable from the oscillation. To prevent this effect, one condition in the selection of the events has been used in such a way as to minimise the oscillations presented on Equation 10.1. The one below:

$$(\text{maximum background})/(\text{RMS background}) < 2.5 \quad (10.1)$$

The Condition in Equation 10.1 takes into account the ratio between the maximum of the background with the RMS background to prevent eventual oscillations. In Section 6.5, it has been shown that a 99.7% of a Gaussian noise is contained in a range of  $3\sigma$  so  $MaxNoise_{Gaus} < 3 * RMS_{Gaus}$ . The same ratio can be calculated for a sinusoidal signal noise :

$$f(x) = A * \sin\left(\frac{2\pi}{T} + \phi\right), \text{ with } T = 2\pi \text{ and } \phi = 0 \quad (10.2)$$

$$\begin{aligned} \sigma^2 &= \langle x^2 \rangle - \langle x \rangle^2 \\ &= \frac{A^2}{2\pi} \left[ \int_0^{2\pi} x^2 \sin(x) dx - \left( \int_0^{2\pi} x \sin(x) dx \right)^2 \right] \\ &= \dots \\ &= \frac{A^2}{2\pi} [2x \sin(x) - (x^2 - 2) \cos(x)]_0^{2\pi} - \frac{A^2}{2\pi} ([\sin(x) - x \cos(x)]_0^{2\pi})^2 \\ &= \frac{A^2}{2\pi} (4\pi^2 + 4\pi^2) = \frac{A^2}{2\pi} 8\pi^2 = A^2 4\pi \end{aligned} \quad (10.3)$$

By putting the result equal to 1, because it has been normalised by period which is the factor  $\frac{1}{2\pi}$ , gives the maximal amount of the amplitude. and so :

$$A = \frac{1}{\sqrt{2\pi}} \quad (10.4)$$

And so as  $\sigma = \text{RMS}$ , resulting in the condition below which is rounded to the nearest tenth:

$$\text{Max}_{\text{sinus}} < \sqrt{2\pi} \text{RMS}_{\text{sinus}} \rightarrow \frac{\text{Max}_{\text{sinus}}}{\text{RMS}_{\text{sinus}}} < 2.5 \quad (10.5)$$

That is the reason for introducing the selecting condition Equation 10.1. Introducing this condition will exclude all signal with sinusoidal behaviour.

## 10.4 Time-Walk correction

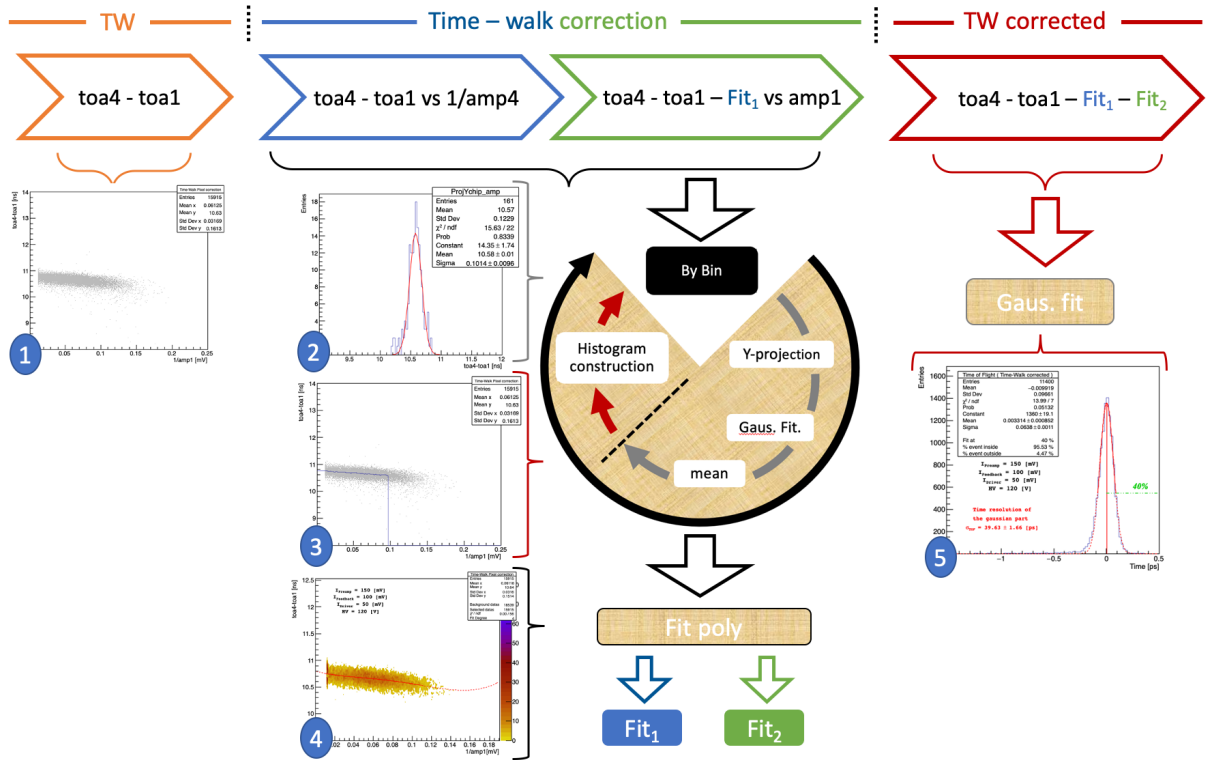


FIGURE 10.4 – A diagram representing the step-by-step procedure made in the time resolution analysis. The left side shows the starting point of the analysis with a scattered plot representing  $\text{Toa4-Toa1}$  versus  $1/\text{amp4}$ . The middle part consists of the Time-Walk correction steps resulting in two fits and the right side is the final Time-Walk, corrected and fitted with a Gaussian approximation.

The main aim of the scripts performing the data analysis is to reach the minimum level of time resolution (e.g. minimum standard deviation). As we have seen in the previous

sections, the accuracy of timing measurement is limited by the jitter (time variation due to the noise) and the Time-Walk (time variation due to the amplitude variation of the signals). While we are interested in the jitter signal, a partial correction to the Time-Walk can be done by using, firstly, the distribution of the correlations between the TOF <sup>[d]</sup> of the prototype signal Amplitude and the LGAD's signal amplitude. This is made in such a way as to focus the results on the jitter.

The analysis starts from the TOF between the ATTRACT prototype and the LGAD by subtracting the TOA of the ATTRACT chip to the TOA of the LGAD. Figure 10.4 presents a small diagram summarising step-by-step, the Time-Walk correction made. The analysis starts with a variable that we will call "toa4-toa1" as show on the left side of the figure. The next step will be to realise a scattered plot of "toa4-toa1" versus  $1/amp4$  (where  $Amp1$  represents the amplitude of the events collected with the ATTRACT prototype and  $Amp4$  the amplitude of the signals coming from the LGAD <sup>[e]</sup>). The same analysis would also have been possible with  $amp4$  instead of  $1/amp4$ . The difference results in the simplicity to achieve future fit on it (one example of a resulting scattering histogram is the number 1 in Figure 10.4). On each x-bin of this histogram, a y-projection will be carried out and a Gaussian fit applied to obtain each mean value (represented by the histogram number 2 on the same figure). In parallel, a new histogram (the blue line on the scattered histogram number 3) is built with the resulting values. At the end, a polynomial fit is realised on the complete new histogram. This fit is called  $Fit_1$ . This is the first step of the Time-Walk correction as a function of amplitude of the LGAD.

The second step of the Time-Walk correction occurs by applying the same manipulation on the scattering plot  $Toa4-Toa1-Fit_1$  versus  $Amp1$  (e.g. the amplitude events triggered on the ATTRACT chip). This histogram is represented in green in Figure 10.4. A new fit called  $Fit_2$  results at the end of this second data manipulation.

The Time-Walk correction is done after the processing of the two fits. The final Time resolution histogram (histogram 5 representing on  $Toa4-Toa1-Fit_1-Fit_2$ ) can be fitted with a Gaussian fit. The Full Width at Half of the Maximum (FWHM) gives the time resolution of the global system (ATTRACT prototype and LGAD). The LGAD's resolution value has to be subtracted from the result to obtain the time resolution of the ATTRACT prototype (which is 50 ps as mentioned in Section 8.4). In order to reduce the % of the data inside the final fit, a fit at 40% of the maximum on the Time-Walk corrected has been applied.

<sup>[d]</sup> The TOF is simply the time it took to travel from one pixel to another pixel located just after this one. It can be calculated as the time-of-arrival (TOA) of the second pixel minus the TOA of the first pixel

<sup>[e]</sup> The number 1 refers to the input channel number 1 on the oscilloscope while the number 4 the input of the channel number 4. The LGAD is in the input number 4 while the ATTRACT prototype is in the number 1.

# Chapter 11

## Results

### 11.1 Results for the events selection

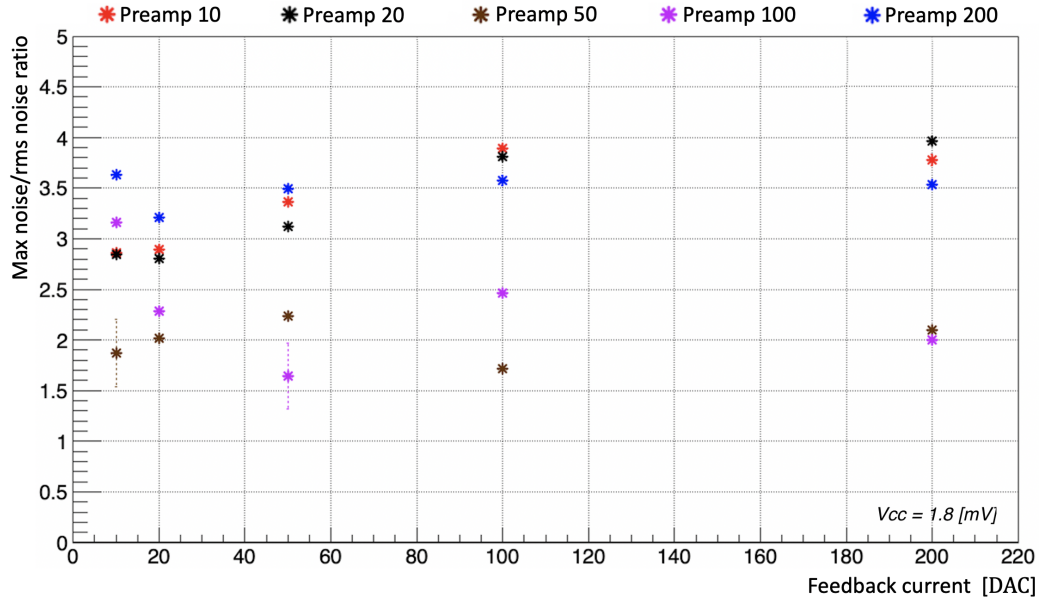


FIGURE 11.1 – Presentation of the results obtained for the ratio of the maximum of the background noise and the root mean squared noise for each configurations measured. The ratio is lower than the condition of 2.5 (presented in Section 10.3) for some points of preamplifier current at 50 DAC and at 100 DAC. These two configurations are not taken into account for the rest of the pre-analysis at feedback 20 and 50 DAC for preamplifier current at 100 DAC and for all the points of the preamplifier current of 100 DAC. Each point refers to a Gaussian distribution, the error is the standard deviation at the full width at half maximum.

The first goal was to study the behaviour of the chip as a function of some different preamplifier current values by making a scan with the feedback current in a range of 10 DAC up to 200 DAC. The values chosen are 10, 20, 50, 100, 200 DAC. This chapter presents the results obtained and lists several arguments supporting the choice of two working points with low and high power consumption. The figures from 11.1 to 11.6 show the results obtained for the different variables listed in Section 10.2 which are the ratio between the maximum of the noise over the root mean squared - *RMS* - noise, the amplitude of the voltage, the equivalent noise charge - *ENC* -, the rise time, the signal to noise ratio and the time-over-threshold. All the variables are presented as a function of the feedback DAC current.

As previously explained in Section 10.3, the background noise is a determinant for the events selection, in order to eliminate measurements showing oscillations from electronic components. Figure 11.1 shows the background noise ratio between the maximum noise and the *RMS*. For this plot the filling condition has not been taken into account in order to bring out the oscillating configurations. The same figure shows that for the low and high amplifier current values the ratio is up to 2.5 but in the intermediate values (e.g. for a preamplifier current of 50 and 100 DAC) this is not the case. It also seems to decrease as the feedback current increases. This argument is validated by observing the figures in the annex 14.1 which show a net difference between the amplitude of the noise's oscillations at low and high feedback current values.

All points less than 2.5 contain a significant amount of oscillating signals. That is why the points below this limit for the preamplifier current at 50 DAC and at 100 DAC have been removed to the furthers pre-analysis, at feedback current, equals 20 and 50 DAC, for the first one, and all the points for the second one. The higher is a point, the closer to a Gaussian noise distribution is the measurement configuration.

## 11.2 Results for the pre-analysis

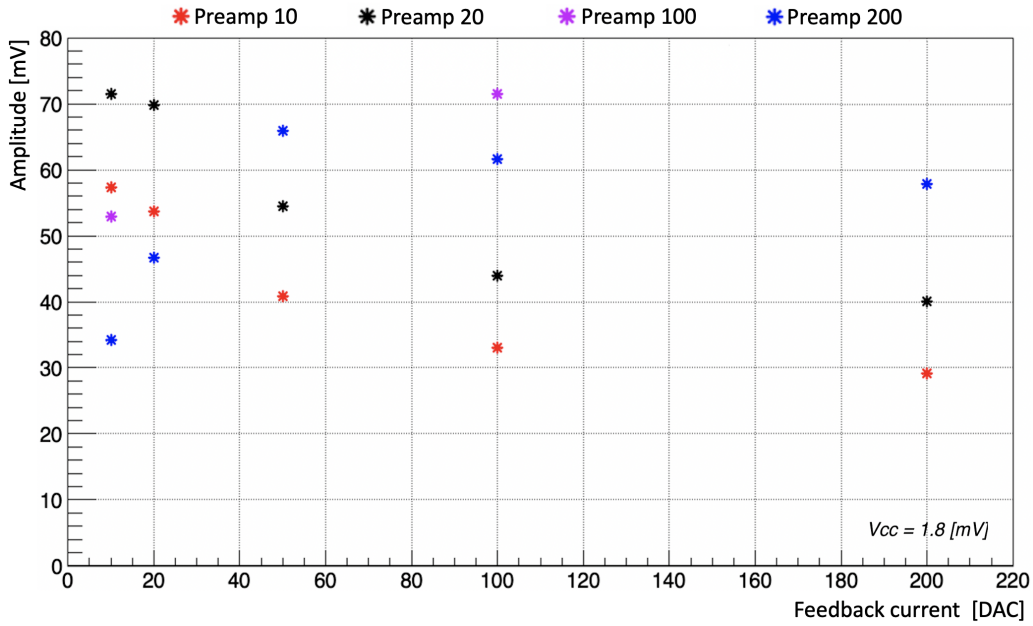


FIGURE 11.2 – *Amplitude results as a function of the feedback current and for different values of preamplifier current. Two behaviours are clearly distinguishable. For values higher than 50 DAC for the preamplifier current has a maximal range of  $\approx 50$ -100 DAC for the feedback current, but for low preamplifier current values, the maximum value is when the feedback current is small. This gives important information for the choice of a low and high power consumption working point, keeping both on high level of signal amplitude.*

The results of the mean of the signal's amplitude as a function of the feedback current

is presented in Figure 11.2. Two specific behaviours can be observed. The curves related to the preamplifier bias equal to 10 DAC and 20 DAC decrease constantly while the two others increase (preamplifier current at 100 DAC and 200DAC ). A certain value between preamplifier bias 20 DAC and 100 DAC delimits the two behaviours. This could be caused by the oscillations effect explained previously.

Ideally the amplitude should be chosen in order to be maximised. So for a working point with a high power consumption, it would have a preamplifier current higher than 100 DAC and a feedback current higher than about 50 DAC but 100 DAC would be better, because it seems to have the highest amplitude with the preamplifier current at 100 DAC. So with this resulting plot, two ranges can be defined, one for the high voltage power consumption working point, which is above a value of 50 DAC for the feedback current because the higher is the preamplifier bias, the higher will be the amplitude. While below 50 DAC for the feedback current, the situation is inverted which means that for the lower power consumption working point, the best condition will be with a feedback current lower than 50 DAC and a preamplifier current lower than 20 DAC, to still have enough signal to be triggered. The lower and higher WP should both have a maximised amplitude. While for the first one, the preamplifier should be minimized, on the second one, it should be maximized.

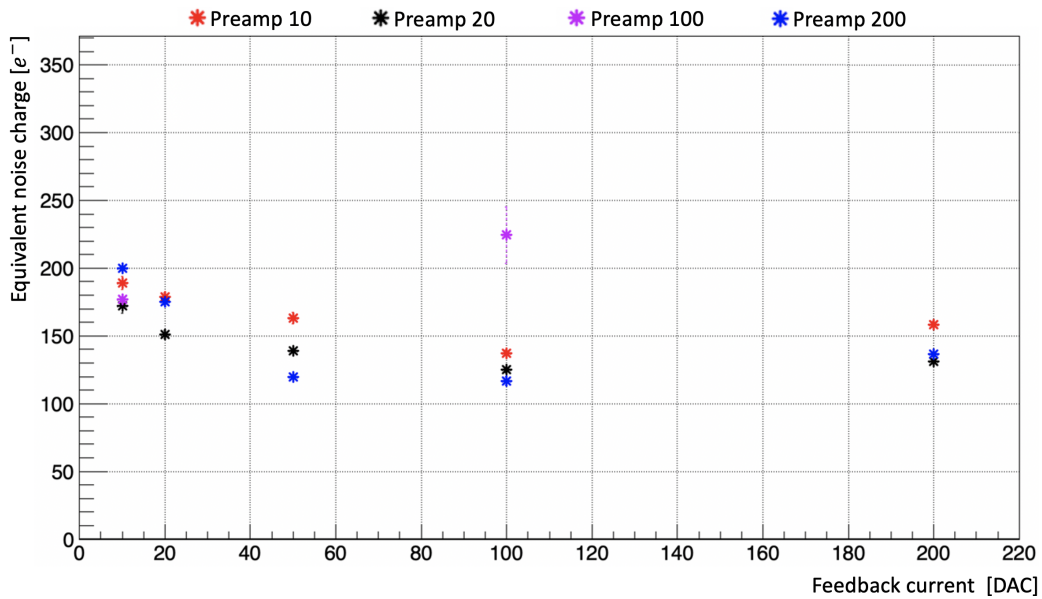


FIGURE 11.3 – The results obtained for the ENC largely have the same convex shape for all the different curves except at preamplifier current 100 DAC, this is not surprising because this point was localized around the limit of 2.5 in the figure representing the ratio between the maximal noise over the RMS noise. For the best performances, a working point should be around 100 DAC for the feedback current where the ENC is minimized for all of them (except for preamp 100 DAC).

As it has been explained in Section 6.5, ENC is a quantity used to express the noise level equivalent to one charge. It characterises the performance of an electronic system. For this study, it is assumed that a delta pulse of charge  $Q_\delta$  will produce a voltage output with



an amplitude  $\Delta V_{out}$ . The ENC will be defined as a delta of charge  $Q_{\delta ENC}$  at the input producing a  $\Delta V_{out ENC}$  at the output which is simply equal to the square root of variance of the RMS, minus the variance of the scope noise, divided by the the amplitude's signal, as shown in equation 11.1.

$$ENC(e^-) = 6250 * \frac{\sqrt{\sigma_{RMS}^2 - \sigma_{scope}^2}}{Amplitude} \quad (11.1)$$

Figure 11.3 represents the results obtained. The preamplifier current 100 DAC curve has an anomalous point at feedback 100 DAC which should be investigated. As it was at the limit of the condition selecting the events (e.g. the noise ratio equal to 2.5 as shown in Figure 11.1), the *RMS* noise in this measurement condition (preamplifier current 100 DAC and feedback current 100 DAC) is higher than the others, which is why the input charge produced at the output, has a signal amplitude equal to the *RMS* noise which is higher than the other preamplifier current value curves, at the same equal value of the feedback current (e.g. 100 DAC). The choice of future working points should minimise the ENC factor, while the signal to noise ratio should be maximised .

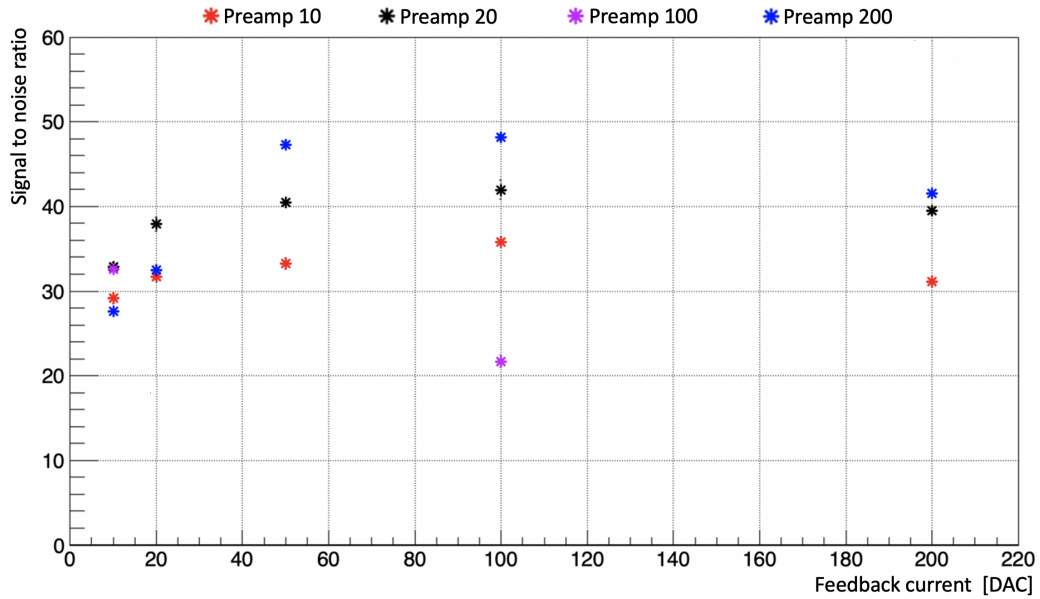


FIGURE 11.4 – This figure represents the results obtained concerning the Signal to noise ratio as a function of the feedback current for the different values studied for the preamplifier current. If the pink curve is not taken into account, it is easy to observe that the higher the preamplifier current is, the higher will be the signal to noise ratio. It seems that the global shape of the curves are concave.

Figure 11.4 shows the results of the signal to noise ratio. It makes sense that the highest curves are the ones with a the highest value for the preamplifier DAC and are shown in blue. If the pink curve is not taken into account, the higher the preamplifier current value is, the higher will be the signal to noise ratio. This makes sense because the preamplifier current controls the gain factor of the SiGe transistor in an amplification mode (which increases the gain while keeping the noise level stable and low). The same observations

can be done concerning the anomalous point with a preamplifier current value of 100 DAC at a feedback current of 100 DAC. It seems that the global shape of the colored curves are like a concave shape. The maximal signal to noise range is around the value of 100 DAC for the feedback current so the highest power consumption working point should then be around this range also.

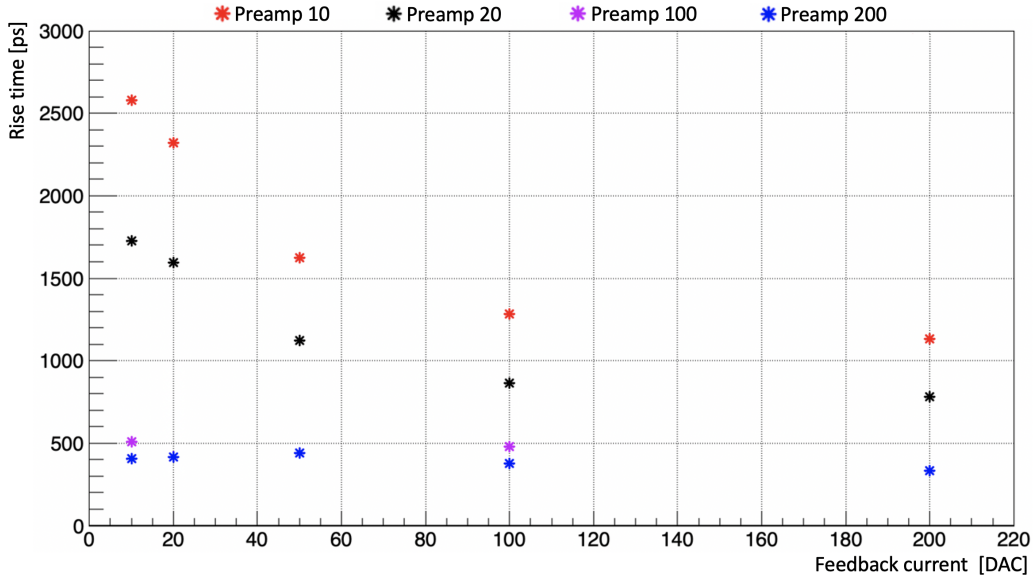


FIGURE 11.5 – *This figure represents the results obtained concerning the rise time as a function of the feedback current for the different values studied for the preamplifier current. It makes sense to see that increasing the preamplifier current decreases the rise time. For low values of the preamplifier DAC current, the increase of the feedback current accentuates the decrease in rise time while for high values no significant changes seems to be observed (curve blue at preamplifier current 200 DAC).*

The rising time has to be minimised according to the amplitude. A short rise time does not necessarily mean that the signal has a high amplitude. Indeed, the rise time is the time taken for a signal to rise from 20% to 80% of its amplitude, a small signal (or noise if the threshold is too low) can also have a very short rise time and so it can then distort the results. In Figure 11.5, the higher the preamplifier bias, the lower will be the rise time.

For the future working point chosen, the Time over threshold has also to be minimised (Shown in Figure 11.6). This is to exclude the signals which have a small amplitude and are too long in time, in favour of signals having the same shape as the one shown in Figure 10.2. A long time over threshold can mean several signal behaviours such as a waving signal, which is not representative of a real peaking signal. Keep in mind that a good signal is a high and skinny peak. To reach the best TOF measurement, the range below feedback bias 60 mV should be avoided and for the TOT an high preamplifier value should be favoured.



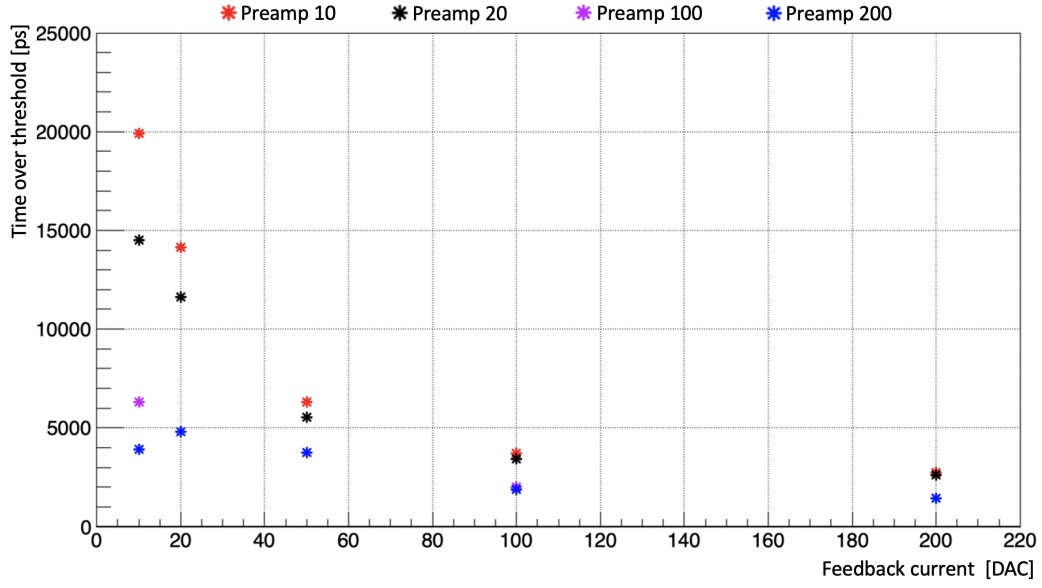


FIGURE 11.6 – This figure shows the results obtained for the TOT. The behaviour is largely similar for all the different characterisations studied. There is still a difference discernible at low values of the feedback current. The fact that the time over threshold is long at low preamplifier and feedback current, could mean that signals are long and maybe their shape is not really a peak but more like a bump ( but it can also be confused with noise).

### 11.2.1 Working points chosen

Finally, The working points (WPs) chosen are: WP1, which is a WP with a high power consumption and another, WP2, with a low power consumption, as listed below: -

- WP1:  $V_{CC} = 1.8V$ ,  $I_{Preamp} = 150$  DAC,  $I_{feedback} = 100$  DAC and  $I_{Driver} = 50$  DAC.
- WP2:  $V_{CC} = 2.0V$ ,  $I_{Preamp} = 7$  DAC,  $I_{feedback} = 10$  DAC and  $I_{Driver} = 200$  DAC.

The next step will be the time resolution analysis. For both WPs, a scan for the High-Voltage (HV) has been done, starting from 80V and followed by 100V, 120V, 140V and 160V. The  $I_{driver}$  values have been chosen in a such way that the incoming current to the oscilloscope is large enough to be read. That means for low values of  $I_{feedback}$  and  $I_{Preamp}$ , very small currents come from the pixels, they must therefore be amplified in order to send them to the oscilloscope. In the case of the Low Power consumption WP, the small values chosen for  $I_{feedback}$  and  $I_{Preamp}$  have to be compensated by a high value of  $I_{Driver}$ . That is why the  $I_{Driver}$  has been set to a value of  $I_{Driver} = 200$  DAC for the low power consumption WP. On the other hand, for high values of  $I_{feedback}$  and  $I_{Preamp}$ , the situation is reversed, it is then not necessary to define a large value for  $I_{Driver}$ , which has been set to  $I_{Driver} = 50$  DAC for the High Power consumption WP.

### 11.3 TOF - Time resolution measurement

The electrons emitted by the  $^{90}\text{Sr}$  source were used to measure the jitter on the TOF between the analogue pixel 1 ( named A in Figure 7.3 ) and the reference LGAD detector. The 4 analogue pixels were named pixel 1, pixel 2, pixel 3 and pixel 4. Pixel 1 and 3 are opposites, as are pixels 2 and 4. Four signals were analysed on the oscilloscope they are the ones from pixels 1 to 3, named channel 1 to 3 and the fourth signal studied was on channel 4, coming from the LGAD. The output of the amplifier heterojunction bipolar transistors connected to the pixel under test was read by the oscilloscope with a sampling rate of 40 GSa/s and an analogue bandwidth of 4 GHz and is explained in Section 8.3.2. The pixels 2 and 3 were operating at the lowest possible threshold that was clear of the noise. They were read by one channel of the oscilloscope and used to study the charges sharing between the pixel 1 under test and the neighbouring pixels. Pixel 4 has not been used during this study. The oscilloscope was configured to capture a pulse from pixel 1 and a pulse from the LGAD with a time window of 200 ns. At each trigger, the waveforms of pixel 1, 2, 3 and the LGAD were saved. As explained in Section 10.1, each waveform was split in two regions which are the background region and the signal region.

To keep the reference time under control, only the events with LGAD pulse amplitudes, in the interval in which the LGAD time resolution was measured to be 50 ps, were considered. The data acquisition has been made in two steps. The first one is made on the oscilloscope which triggers coincidences between the pixel 1 and the LGAD on events passing above the threshold. The second step is made analytically at the beginning of the script and explained in Section 10.4. The script selects events with more precise conditions which are listed below: -

1. The amplitude of channel 1 (e.g. pixel 1) has to be higher than channel 2 and 3 (e.g. pixel 2 and 3). This condition has been applied to avoid cross talk between pixels in the data and focuses the analysis only on pixel 1.
2. The amplitude of channel 1 (e.g. pixel 1) has to be higher than the selected threshold on channel 1. Lower events are discarded. This second condition is there to avoid the noise effects.
3. To keep the time reference under control, only the events coming from channel 4 (e.g. the LGAD) with an amplitude included in the interval in which the LGAD has a 50 ps time resolution, were retained. To respect this resolution, the amplitude range considered (of the waveforms coming from the LGAD) is between 70 mV and 110 mV, that is why another condition has been fixed on channel 4 (e.g. pixel 4) in such a way that amplitude 4 is higher than 70 mV but lower than 110 mV. This is simply the LGAD configuration.

Data was taken at different threshold and High Voltage values. The TOF values were calculated in this way:

$$TOF = TOA_{channel4} - TOA_{channel1} = TOA_{LGAD} - TOA_{pixel1} \quad (11.2)$$

Where  $t_{channel1}$  is the  $TOA$  measured by the channel 1 (pixel 1) on the ATTRACT prototype and  $t_{channel4}$  is the  $TOA$  measured by the reference LGAD. As explained in Section 10.4, the Time-Walk can be partially corrected by using the distributions correlations between the TOF and the inverse of the amplitude of waveforms coming from the pixel 1 of the ATTRACT prototype and between the TOF and the amplitude of the signals coming from the LGAD. Figure 11.7 shows an example of the results obtained for the two distribution correlations for a specific working point (WP1) at  $HV = 140$  V. The results for other values of high-voltage for both WPs are presented in Annex 14.3 for WP1 and Annex 14.2 for WP2. The right side of 11.7 is a representation of TOF versus the amplitude of channel 4 (e.g. signals from the LGAD) in which the fitted correlation from the distribution shown on the left side of the same figure has been subtracted.

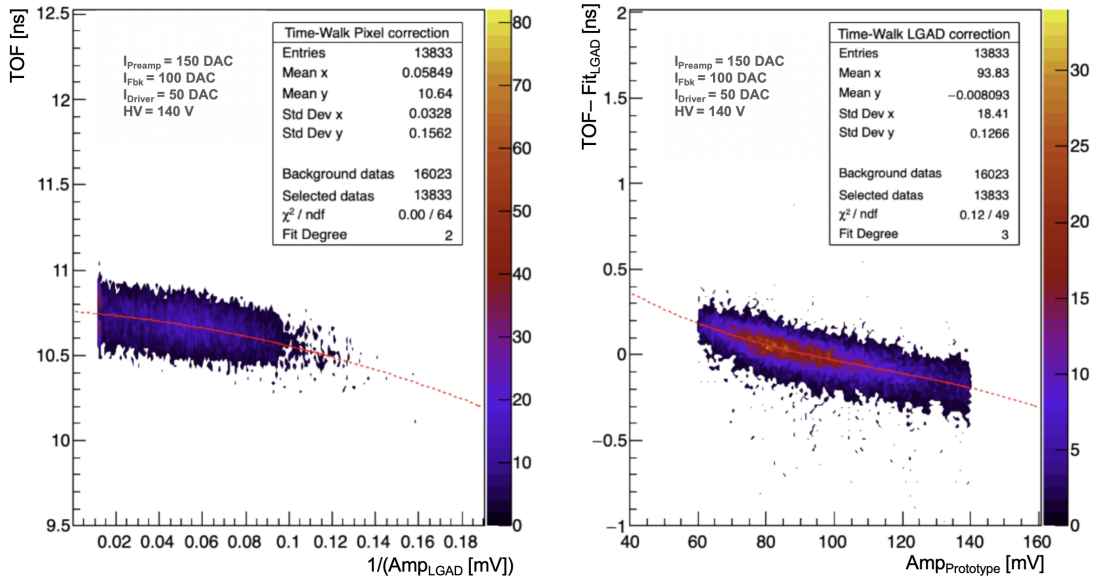


FIGURE 11.7 – The left panel shows the first Time-Walk correction with respect to  $1/\text{amp1}$  (amplitude distribution of pixel number 1) while the right panel represents the 2<sup>nd</sup> Time-Walk correction with respect to  $\text{amp4}$  (amplitude distribution of the LGAD). These results represent WP1 at  $HV = 140$  V.

The left panel of Figure 11.7 shows the correction in respect of  $1/\text{amp1}$  (referring to the amplitude distribution of channel 1) obtained for the pixel Analogue number 1. The right panel shows a second correction made respectively to amplitude 4 (related to the LGAD amplitude distribution).

The right panel of Figure 11.8 shows the TOF distribution for the same working points after the two corrections. The mean value of the distribution was close to zero due to these corrections. A non-Gaussian tail is observed for negatives TOF-corrected values. This tail is present for all threshold and HV values measured (the reader can take a look in Annex 14.2 and 14.3 which show the results obtained for all the working points analysed). This could be attributed to several possible causes, firstly, due to the electrons from the source crossing the region between two pixels and secondly, due to the electronic noise coming from the amplification. This tail is systematic and comes from the signal  $TOA$  values which are caused by signals with a shape characterised by a lower slope than

the average and therefore coming from waveforms rising slower than most signals. The electronic reason for its presence should be further investigated.

FIGURE 11.8 – *Representation of the TOF distribution after corrections with 1/amp1 and amp4. These results represent WP1 at HV = 140 V. The number of Entries on the right panel is lower than the two scattered plots presented in Figure 11.7. This is due to the fact that the third fill condition is different. For the TOF distribution to be correct, the condition on the amplitude of channel 4 has been applied. It has to be higher than 70 mV and lower than 110 mV to respect the resolution of the LGAD to 50 ps. However, for the scattered plots, this range has been enlarged to an amplitude of channel 4 higher than 60 mV and lower than 140 mV in order to obtain better fit results.*

It can be seen in Figure 11.8 that a Gaussian fit at a range of 40 % has been applied to the TOF corrected distributions to estimate the time jitter of the core of the distributions and so the time resolution of the ATTRACT prototype. Normally, when the histogram studied behaves as a normal distribution with a standard deviation  $\sigma$ , the relation between the FWHM and the standard deviation is valid. (e.g.  $FWHM = 2\sqrt{2\ln(2)} \sigma \approx 2,355 \sigma$ ). In particle physics, the resolution of a peak is defined as the width of the peak measured at half the height of the peak and is called the FWHM resolution. So to be in the range and to have results representing as much as possible of the measurements, a fit at 40% has been chosen. Of course by being careful that the 40% respects the Gaussian behaviour of the TOF-corrected distributions and also that no queue is present at an higher percentage level ( $> 40\%$ ) neither on the positive side nor on the negative side of the distribution. In any case, for all the results obtained the  $\sigma_{TOF}^{cor}$  obtained by the fit were around the FWHM of the distributions.

The time resolution of the ATTRACT prototype chip was calculated by the subtraction of the square of 50 ps time resolution contribution of the reference LGAD from the TOF-corrected values. The smallest value of Time resolution obtained with the 50 ps resolution LGAD is for the working point WP1 configured with  $I_{preamp} = 150$  mV,  $I_{feedback} = 100$  mV and  $I_{driver} = 50$  mV at a HV of 160 V and is:

$$\sigma = \sqrt{(\sigma_{TOF}^{cor})^2 - (\sigma_{LGAD})^2} = \sqrt{59.73^2 - 50^2} = (32.7 \pm 1.8)ps \quad (11.3)$$

Figure 11.9 represents the results obtained for the different preamplifier DAC currents tested (referring to the two working points) as a function of the increase of the high-voltages. In any cases, the measured time resolution is below 140 ps and improves as higher high-voltage values. The same analysis of the time resolution has been done without the amplitude corrections and the jitter was always higher with respect to the results obtained with the corrections. In all instances the non-Gaussian tails have been calculated and the results averaged are:

- **WP1** : below 10 % of the total amount of events.
- **WP2** : below 17 % of the total amount of events.

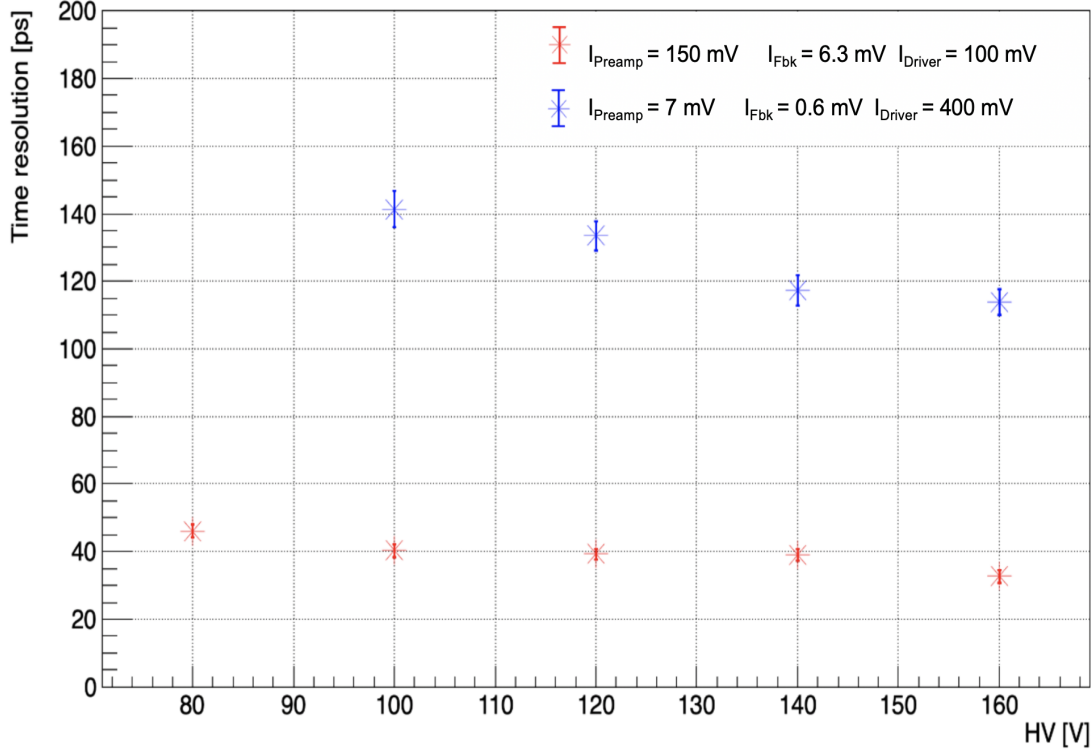


FIGURE 11.9 – *Final results obtained for the two WPs for the time resolution of the ATTRACT prototype. The red curve representing the WP1 - highest power consumption - has a behaviour almost flat while the blue curve is decreasing with the increase of the HV. The results obtained are between 33 ps and 114 ps which are very good results compared to the most of the Silicon pixel detectors in use actually. It can be seen that the LPC has a descending behavior which is due to the increase of the HV and therefore of the length of the depleted region. On the other hand, the HPC configuration seems to have no dependence on the increase in HV.*

Having a 17 % rate for the WP2 is not surprising. Indeed, this WP2 has been chosen to be the lowest power consumption working point and so, let's say, having the *worst* results. By *worst*, it means the higher TOF results but also the higher outside % rate of the Gaussian TOF distribution tail. Figure 11.9 shows the dependence of the time resolution on the high voltage for the analogue pixel number 1. An improvement of the time resolution is observed with increasing the HV. This behaviour can happen for multiple reasons:-

- When the HV increases, the depletion region increases as well and so only larger charge signals and maybe a lower capacitance reaching the electrodes leaving less noise, less tail, a more Gaussian TOF distribution and therefore better results.
- Having a higher HV implies a better uniformity of the charge carriers drift velocity as shown in Figure 5.7 and so higher performances from the sensor part of the pixel.
- Less noise coming from the Front-End.

It is interesting to see that the flat behavior of the HPC WP could indicate that beyond certain values for the currents pair  $(I_{Preamp}, I_{feedback})$ , the resolution seems to have no dependencies on HV anymore. It might be interesting to find this pair in order to find a WP that keeps this kind of time resolution result range while having reduced power consumption, so as to save power. Indeed, there is no reason in consuming more energy if the results remain the same beyond a certain value of HV. The time resolution is limited by the jitter of the preamplifier.

# Chapter 12

## Conclusion and Outlook

An overview of pixel detectors, as well as their operation, has been carried out during this thesis in order to understand a monolithic Silicon pixel prototype. The detection of the minimum ionizing particles has been measured with its 60  $\mu m$  thick p-n sensor and read out by its HBT-SiGe electronic Front-End. A measurement of its timing performance was done with a  $^{90}Sr$  source setup. The jitter coming from the collection charges as well as the weighing field as been neglected by the characteristics of the geometry of the sensor. The Time Walk as been corrected in a such way to obtain only the jitter related to the amplification process into the front-end.

The time resolution achieved with a LGAD, having a resolution of 50 ps, is equal to  $(32.7 \pm 1.8)$  ps for the best performance related to the high power consumption configuration which was set to a preamplifier current of 150  $\mu A$  <sup>[a]</sup> while a result of  $(113.8 \pm 3.7)$  ps was reached with the low power consumption configuration set to a preamplifier current of 7  $\mu A$ . The best performances were estimated around 30 ps <sup>[b]</sup> which is in accordance with the results presented on Figure 11.9. The results obtained are excellent and exceed the time resolution of all detectors in use today. They show that this kind of very thin sensors coupled with a HBT-SiGe amplifier can be used to produce Silicon Pixel detectors with low time jitter and a high resolution even at low power consumption.

Furthermore, the results obtained for the ENC show values lower than 200  $e^-$ . This result can be related to the signal to noise ratio which is higher than 30. These two results are excellent. They allow to work very efficiently with minimal ionising particles.

However, the results show that the measured time resolution contains a contribution from the electronic jitter of the front-end circuit which indicates that the sensor best performances have not yet been completely exploited. Indeed, the measurement show that the electronic noise may be the dominating factor contributing to the time resolution which can be improved in the future. An analysis of the results indicates several causes :

- The analysis: The tail on the Time-Walk corrected distributions suggest that the analysis could be improved. A projection by bin has been carried out for the fitting method. For certain points analysed, it has been observed that the method was not optimal for signals which have a delayed rise leading to *TOA* values which are under-compensated for Time-Walk, producing a non Gaussian tail. By improving the way the fit is done, for example, by doing an interpolation over the centre of each bin after the projection, could help.
- The Front-End oscillations : As it has been presented in Section 10.3, some DAC current configurations can lead to signal oscillations which are caused by an ampli-

---

<sup>[a]</sup> See Table 8.1 for more information.

<sup>[b]</sup> This value comes from simulations.

fication effect due to the resonance frequency of some electronic(s) component(s) <sup>[c]</sup> used in the readout. This effect suggests that the electronic part could have some impact on the timing performance of the ATTRACT prototype.

- The sensor : Even if the results of the high power consumption working point are almost flat in timing performance at higher high-voltage values, it could mean that an increase of the width of the depletion does not necessarily improve the results. The results obtained for the low power consumption working point improve in timing performance at higher high-voltage values, which means that the increase of the width of the depletion layer is beneficial for the best results. So this design characteristic could limit the results (but if it is the case, only at very low time-resolution for which the electronic noise would have already been sufficiently improved).
- The LGAD : The one used has a time resolution of 50 ps which is too high when the estimated results are much lower than that. Changing the LGAD for one with a lower timing resolution, would certainly help.

Some improvements concerning the analysis have already started, also a replacement of the LGAD used has been sourced. This should significantly improve the results in order to obtain even more precise resolution. The reason of the oscillations have also been identified. They depend on the frequency. The chip has the same supply line for the  $I_{Preamp}$  and the  $I_{Driver}$ . For certain frequencies, the current amplified by the driver returns to the amplifier through this supply line. A parasite feedback effect is so generated creating an amplification loop of the signal. In the new version, a separation of the power supplies for the drivers and the amplifier will be done. The time resolution results could then be improved by an increase of the amplification while with this prototype, the increase in amplification is impossible because of these oscillations.

---

<sup>[c]</sup> The (s) has been used in this sentence to take into account the different possibilities. To identify the responsible component (s) it would be necessary to go into more detail in the theory of electronics.



# Chapter 13

## Acknowledgements

The writing of my thesis would not have been possible without the huge support and help of the following peoples.

First of all, I would like to thank Prof. Giuseppe Iacobucci who welcomed me into his research group and gave me the opportunity to realise this thesis. I learned a lot, not only from a theoretical point of view but also, on a more practical side, regarding the development of physics devices.

I would like to thank also all the group for devoting me their time and answering all the questions that I had. Thank you to my supervisor, Lorenzo Paolozzi who was always there for me, spending his time giving additional lessons and explanations. Thank you for your knowledge, your availability and your patience.

I want to thank all the members of my family as well as my friends who had to put up with me during the realization of my work. A special thanks to Heather Holmes who saw this daily, as well as Theo Moretti with whom I had the chance to collaborate on data acquisition. Good humor was always present. I really enjoyed working with you!

I would like to say a special thanks to Kenneth and Shauna Holmes and Rebecka Sax who helped me battle through the typos, errors of language and so on ... without whom my thesis would have never been finished.

I will finish this acknowledgements by thanking all the possible people that I would not have mentioned who participated directly or indirectly in my thesis.

Thanks to everyone!



Carmelo Miletto

# Bibliography

- [1] Le boson de Higgs, . URL <https://home.cern/fr/science/physics/higgs-boson>.
- [2] CERN. Dark matter. URL <https://home.cern/fr/science/physics/dark-matter>.
- [3] William Frass and Dr Roman Walczak. Passage of Particles Through Matter. page 26. URL <https://www2.physics.ox.ac.uk/sites/default/files/Passage.pdf>.
- [4] Marco Delmastro. Experimental particle physics, January 2021. URL [https://indico.cern.ch/event/294651/contributions/671929/attachments/552041/760669/Delmastro\\_ESIPAP2014\\_3.pdf](https://indico.cern.ch/event/294651/contributions/671929/attachments/552041/760669/Delmastro_ESIPAP2014_3.pdf).
- [5] L. Rossi, P. Fisher, T. Rohe, and N. Wermes. *Pixel Detectors - From Fundamentals to Applications*. Springer, Berlin, 2006. ISBN 3-540-28332-3.
- [6] Eric Ford. Particle Interactions with Matter. In *Primer on Radiation Oncology Physics*, pages 63–72. CRC Press, 1 edition, May 2020. ISBN 978-0-429-48888-7. doi: 10.1201/9780429488887-7. URL <https://www.taylorfrancis.com/books/9780429950247/chapters/10.1201/9780429488887-7>.
- [7] K Kleinknecht, C Grupen, and J Ferbel. Principles of detection of particles/radiation Limitation of detectors Efficiency Position resolution Energy resolution Time resolution Impact on biological systems Radiation damage Radiation protection Radiation therapy Literature. page 33. URL [https://www.physik.uzh.ch/dam/jcr:fb1819ad-fcf7-4680-a743-6794e5c76296/empp15\\_KM\\_bethebloch.pdf](https://www.physik.uzh.ch/dam/jcr:fb1819ad-fcf7-4680-a743-6794e5c76296/empp15_KM_bethebloch.pdf).
- [8] Giuseppe Iacobucci. Cours de Particules et noyaux, 2018.
- [9] D. E. Groom and S. R. Klein. Passage of particles through matter. *The European Physical Journal C*, 15(1-4):163–173, March 2000. ISSN 1434-6044, 1434-6052. doi: 10.1007/BF02683419. URL <http://link.springer.com/10.1007/BF02683419>.
- [10] A. Martin-Garin. FICHE RADIONUCLÉIDE Cadmium 109 et environnement, October 2004. URL [https://www.irsnn.fr/FR/Larecherche/publications-documentation/fiches-radionucleides/Documents/environnement/Cadmium\\_Cd109\\_v1.pdf](https://www.irsnn.fr/FR/Larecherche/publications-documentation/fiches-radionucleides/Documents/environnement/Cadmium_Cd109_v1.pdf).
- [11] edp science. Radioactivite : La capture électronique. URL <https://www.laradioactivite.com/site/pages/lacaptureelectronique.htm>.
- [12] Capture électronique, November 2020. URL [https://en.wikipedia.org/wiki/Electron\\_capture](https://en.wikipedia.org/wiki/Electron_capture). Page Version ID: 176828504.
- [13] S. Roussel-Debet. FICHE RADIONUCLÉIDE Strontium 90 e t environnement, July 2005. URL [https://www.irsnn.fr/FR/Larecherche/publications-documentation/fiches-radionucleides/Documents/environnement/Strontium\\_2005\\_V1.pdf](https://www.irsnn.fr/FR/Larecherche/publications-documentation/fiches-radionucleides/Documents/environnement/Strontium_2005_V1.pdf).
- [14] University of guelph. Superalowed Decay | Physics, January 2021. URL <https://www.physics.uoguelph.ca/superalowed-%CE%B2-decay>.

- [15] Mark Prelas, Charles Weaver, Matthew Watermann, Eric Lukosi, Robert Schott, and Denis Wisniewski. A review of nuclear batteries. *Progress in Nuclear Energy*, 75:117–148, August 2014. doi: 10.1016/j.pnucene.2014.04.007.
- [16] Timothy Roy, Frederic Tessier, and Malcolm McEwen. A system for the measurement of electron stopping powers: proof of principle using a pure  $\alpha$ -emitting source. *Radiation Physics and Chemistry*, 149:134–141, August 2018. ISSN 0969-806X. doi: 10.1016/j.radphyschem.2018.03.006. URL <https://www.sciencedirect.com/science/article/pii/S0969806X17312070>.
- [17] Dr I Fleck. Part-I: Beta Spectroscopy. page 23.
- [18] Czech Technical University in Prague. IEAP - Institute of Experimental and Applied Physics, March 2021. URL <http://old.utef.cvut.cz/en/index.php?Ns=103&id=1000046&mt=1029>.
- [19] E. Nappi, Seguinot, and Jacques. Ring Imaging Cherenkov Detectors: The state of the art and perspectives. *ResearchGate*, 28:1–130, July 2005. doi: 10.1393/ncr/i2006-10004-6. URL [https://www.researchgate.net/profile/Jacques-Seguinot/publication/234222993\\_Ring\\_Imaging\\_Cherenkov\\_Detectors\\_The\\_state\\_of\\_the\\_art\\_and\\_perspectives/links/5508524a0cf27e990e0a31ba/Ring-Imaging-Cherenkov-Detectors-The-state-of-the-art-and-perspectives.pdf](https://www.researchgate.net/profile/Jacques-Seguinot/publication/234222993_Ring_Imaging_Cherenkov_Detectors_The_state_of_the_art_and_perspectives/links/5508524a0cf27e990e0a31ba/Ring-Imaging-Cherenkov-Detectors-The-state-of-the-art-and-perspectives.pdf).
- [20] Multiwire. From the first particle accelerators to the discovery of the Higgs boson: A brief history of CERN, July 2013. URL <http://www.thestargarden.co.uk/History-of-CERN.html>. Section: Light and Matter.
- [21] B. Degrange, J. Guillon, F. Moreau, U. Nguyen-Khac, C. De La Taille, S. Tisserant, and M. Verderi. Low energy calorimetry in a multiwire chamber filled with tetramethylsilane. *Nuclear Instruments and Methods in Physics Research Section A: Accelerators, Spectrometers, Detectors and Associated Equipment*, 311(3):539, 1992. doi: 10.1016/0168-9002(92)90652-K.
- [22] M. Campbell and J. Alozy. MEDIPIX AND TIMEPIX CHIPS: APPLICATIONS IN IMAGING AND DETECTION OF CHARGED PARTICLES., March 2021. URL <https://indico.cern.ch/event/820083/attachments/1861456/3061478/KTSeminarMC.pdf>.
- [23] Medipix and Timepix chips: Applications in Imaging and Detection of charged particles, . URL <https://indico.cern.ch/event/820083/>.
- [24] Safe Car News. Panasonic develops long-range TOF image sensor | Safe Car News. URL <https://safecarnews.com/staging/panasonic-develops-long-range-tof-image-sensor/>.
- [25] Jack Simons. 2.2: Bands of Orbitals in Solids, May 2014. URL [https://chem.libretexts.org/Bookshelves/Physical\\_and\\_Theoretical\\_Chemistry\\_Textbook\\_Maps/Book%3A\\_Advanced\\_Theoretical\\_Chemistry\\_\(Simons\)/02%3A\\_Model\\_Problems\\_That\\_Form\\_Important\\_Starting\\_Points/2.02%3A\\_Bands\\_of\\_Orbitals\\_in\\_Solids](https://chem.libretexts.org/Bookshelves/Physical_and_Theoretical_Chemistry_Textbook_Maps/Book%3A_Advanced_Theoretical_Chemistry_(Simons)/02%3A_Model_Problems_That_Form_Important_Starting_Points/2.02%3A_Bands_of_Orbitals_in_Solids). University of Utah.

- [26] Philip Moriarty. Band gap, December 2020. URL [https://en.wikipedia.org/w/index.php?title=Band\\_gap&oldid=996665139](https://en.wikipedia.org/w/index.php?title=Band_gap&oldid=996665139). Page Version ID: 996665139.
- [27] EE 105 notes handouts. berkeley.edu, March 2021. URL <https://inst.eecs.berkeley.edu/~ee105/sp08/handouts/EE105notes.pdf>.
- [28] Hu Chenming. PN and Metal–Semiconductor Junctions, February 2009. URL [https://www.chu.berkeley.edu/wp-content/uploads/2020/01/Chenming-Hu\\_ch4-1.pdf](https://www.chu.berkeley.edu/wp-content/uploads/2020/01/Chenming-Hu_ch4-1.pdf).
- [29] Jacobini et al. Electrical properties of Silicon (Si). Phys. Rev. B12, 4:2265–2284, 1975. URL <http://www.ioffe.ru/SVA/NSM/Semicond/Si/electric.html#Transport>.
- [30] Electrical4U. Diode: Definition, Symbol, and Types of Diodes | Electrical4U. URL <https://www.electrical4u.com/diode-working-principle-and-types-of-diode/>.
- [31] Posted 30 Apr 2004 | 20:05 GMT. The Lost History of the Transistor - IEEE Spectrum. URL <https://spectrum.ieee.org/tech-history/silicon-revolution/the-lost-history-of-the-transistor>.
- [32] Abdelali Rennane. Caracterisation et modelisation du bruit basse frequence des composants bipolaires et a effet de champ pour applications micro-ondes. *Université Paul Sabatier de Toulouse*, page 196, May 2005. URL <https://tel.archives-ouvertes.fr/tel-00009299/document>.
- [33] H. Nyquist. Thermal Agitation of Electric Charge in Conductors. *Physical Review*, 32 (1):110–113, July 1928. ISSN 0031-899X. doi: 10.1103/PhysRev.32.110. URL <https://link.aps.org/doi/10.1103/PhysRev.32.110>.
- [34] Krzysztof Iniewski, editor. *Circuits at the nanoscale: communications, imaging, and sensing*. CRC Press/Taylor & Francis, Boca Raton, 2009. ISBN 978-1-4200-7062-0. OCLC: ocn229467459.
- [35] Dallas Texas TexasInstruments. Noise Analysis in Operational Amplifier Circuits, 2007. URL [https://www.ti.com/lit/an/slva043b/slva043b.pdf?ts=1613023030713&ref\\_url=https%253A%252F%252Fwww.google.com%252F](https://www.ti.com/lit/an/slva043b/slva043b.pdf?ts=1613023030713&ref_url=https%253A%252F%252Fwww.google.com%252F).
- [36] Herwig Schopper, Christian W Fabjan, and Stephen Myers. *Particle physics reference library*. 2020. ISBN 978-3-030-38206-3 978-3-030-35317-9 978-3-030-34244-9. OCLC: 1178781906.
- [37] Lorenzo Paolozzi. Timing with silicon detectors. page 44, 2019. URL [https://indico.cern.ch/event/806731/contributions/3517130/attachments/1927029/3190274/2019\\_10\\_16\\_Croatia\\_VERTEX19.pdf](https://indico.cern.ch/event/806731/contributions/3517130/attachments/1927029/3190274/2019_10_16_Croatia_VERTEX19.pdf).
- [38] José Cruz NUNEZ PEREZ. Transistors Bipolaires à Hétérojonction /TBH) SiGe et SiGe:C, 2007. URL [http://csidoc.insa-lyon.fr/these/2007/nunez\\_perez/09\\_chapitre\\_1.pdf](http://csidoc.insa-lyon.fr/these/2007/nunez_perez/09_chapitre_1.pdf).
- [39] Williamson Andrew. Germanium and Silicon - The Diamond Structure, November 1996. URL <http://www.tcm.phy.cam.ac.uk/~ajw29/thesis/node35.html>.

- 
- [40] BAGHDADI Mustapha. Caractérisation et simulation d'un transistor bipolaire à hétéro-jonction (Si/SiGe) en hautes fréquences, 2017. URL <https://dl.ummto.dz/bitstream/handle/ummto/7657/BaghdadiMustapha.pdf?sequence=1>.
  - [41] John R. Arthur. Molecular beam epitaxy. *Surface Science*, 500(1):189–217, March 2002. ISSN 0039-6028. doi: 10.1016/S0039-6028(01)01525-4. URL <https://www.sciencedirect.com/science/article/pii/S0039602801015254>.
  - [42] Jeremy Low, Michael Kreider, Drew Pulsifer, Andrew Jones, and Tariq Gilani. Band Gap Energy in Silicon. *American Journal of Undergraduate Research*, 7, June 2008. doi: 10.33697/ajur.2008.010. URL [https://www.researchgate.net/publication/241884255\\_Band\\_Gap\\_Energy\\_in\\_Silicon](https://www.researchgate.net/publication/241884255_Band_Gap_Energy_in_Silicon).
  - [43] Intel Altera. Cyclone V Device Overview. page 37, May 2018. URL [https://www.intel.com/content/dam/www/programmable/us/en/pdfs/literature/hb/cyclone-v/cv\\_51001.pdf](https://www.intel.com/content/dam/www/programmable/us/en/pdfs/literature/hb/cyclone-v/cv_51001.pdf).
  - [44] Houdré Romuald. Transistor bipolaire - Dispositifs électroniques et optiques à semiconducteurs - Science et génie des matériaux, 2006. URL <https://wiki.epfl.ch/houdre/documents/DispElec/chapitre%2006%20transistor%20bipolaire.pdf>.
  - [45] F Faccio. Radiation effects in the electronics for CMS. page 46. URL [http://lhcb-elec.web.cern.ch/papers/radiation\\_tutorial.pdf](http://lhcb-elec.web.cern.ch/papers/radiation_tutorial.pdf).
  - [46] S.A. Miskiewicz, A.F. Komarov, F.F. Komarov, G.M. Zayats, and S.A. Soroka. Radiation Degradation of Bipolar Transistor Current Gain. *Acta Physica Polonica A*, 132(2):288–290, August 2017. ISSN 0587-4246, 1898-794X. doi: 10.12693/APhysPolA.132.288. URL <http://przyrbwn.icm.edu.pl/APP/PDF/132/app132z2p20.pdf>.
  - [47] Joel Woodward. What's The Difference Between Real-Time And Sampling Oscilloscopes?, April 2013. URL <https://www.electronicdesign.com/technologies/test-measurement/article/21796363/rohde-schwarz-whats-the-difference-between-realtime-and-sampling-oscilloscopes>.
  - [48] Analogue to Digital Converter (ADC) Basics, September 2020. URL <https://www.electronics-tutorials.ws/combinatoin/analogue-to-digital-converter.html>.
  - [49] V. Sola, R. Arcidiacono, M. Boscardin, N. Cartiglia, G.-F. Dalla Betta, F. Ficorella, M. Ferrero, M. Mandurrino, L. Pancheri, G. Paternoster, and A. Staiano. First FBK Production of 50\$μm Ultra-Fast Silicon Detectors. *Nuclear Instruments and Methods in Physics Research Section A: Accelerators, Spectrometers, Detectors and Associated Equipment*, 924:360–368, April 2019. ISSN 01689002. doi: 10.1016/j.nima.2018.07.060. URL <http://arxiv.org/abs/1802.03988>. arXiv: 1802.03988.
  - [50] Gabriele Giacomini, Wei Chen, Francesco Lanni, and Alessandro Tricoli. Development of a technology for the fabrication of Low-Gain Avalanche Detectors at BNL. *Nuclear Instruments and Methods in Physics Research Section A: Accelerators, Spectrometers, Detectors and Associated Equipment*, 934:52–57, August 2019. ISSN 01689002. doi: 10.1016/j.nima.2019.04.073. URL <http://arxiv.org/abs/1811.04152>. arXiv: 1811.04152.

- [51] P. Fernandez-Martinez, D. Flores, V. Greco, S. Hidalgo, G. Pellegrini, D. Quirion, M. Fernandez-Garcia, I. Vila, and G. Kramberger. Low Gain Avalanche Detectors for high energy physics. In *2015 10th Spanish Conference on Electron Devices (CDE)*, pages 1–4, Aranjuez - Madrid, Spain, February 2015. IEEE. ISBN 978-1-4799-8108-3. doi: 10.1109/CDE.2015.7087475. URL <http://ieeexplore.ieee.org/document/7087475/>.
- [52] N. Moffat, R. Bates, M. Bullough, L. Flores, D. Maneuski, L. Simon, N. Tartoni, F. Doherty, and J. Ashby. Low Gain Avalanche Detectors (LGAD) for particle physics and synchrotron applications. *Journal of Instrumentation*, 13(03):C03014–C03014, March 2018. ISSN 1748-0221. doi: 10.1088/1748-0221/13/03/C03014. URL <https://iopscience.iop.org/article/10.1088/1748-0221/13/03/C03014>.
- [53] Giuseppe Iacobucci. The path to picosecond-level time resolution with SiGe BiCMOS monolithic pixel sensors, April 2019. URL <https://indico.cern.ch/event/851182/>.

# Chapter 14

## Annexes

### 14.1 Oscillation effect results

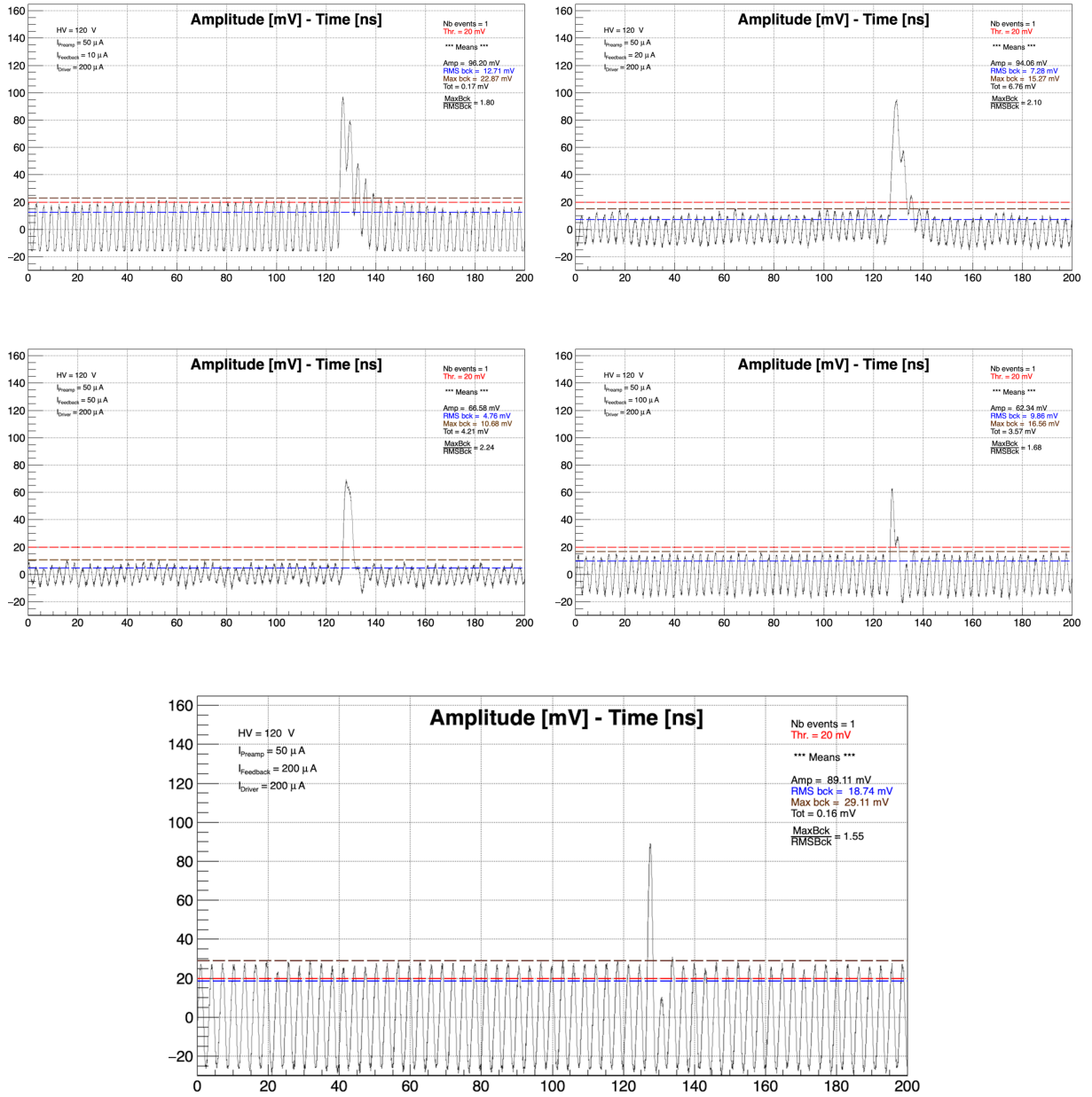


FIGURE 14.1 – Condition: Bias preamp = 50 DAC (Bias feedback : 10, 20 , 50, 100 and 200 DAC) Representations of events not selected using the condition of Equation 10.1.

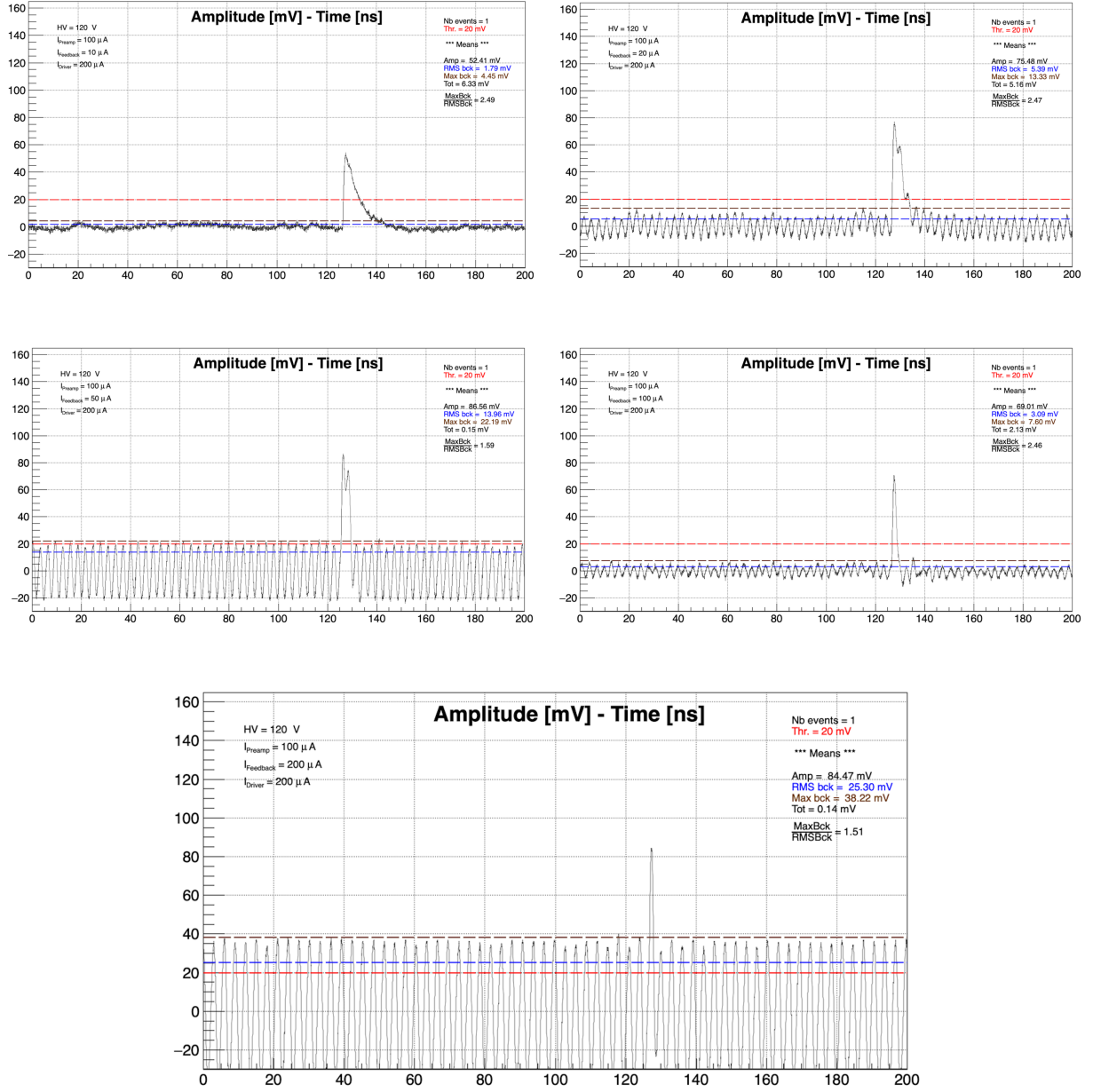
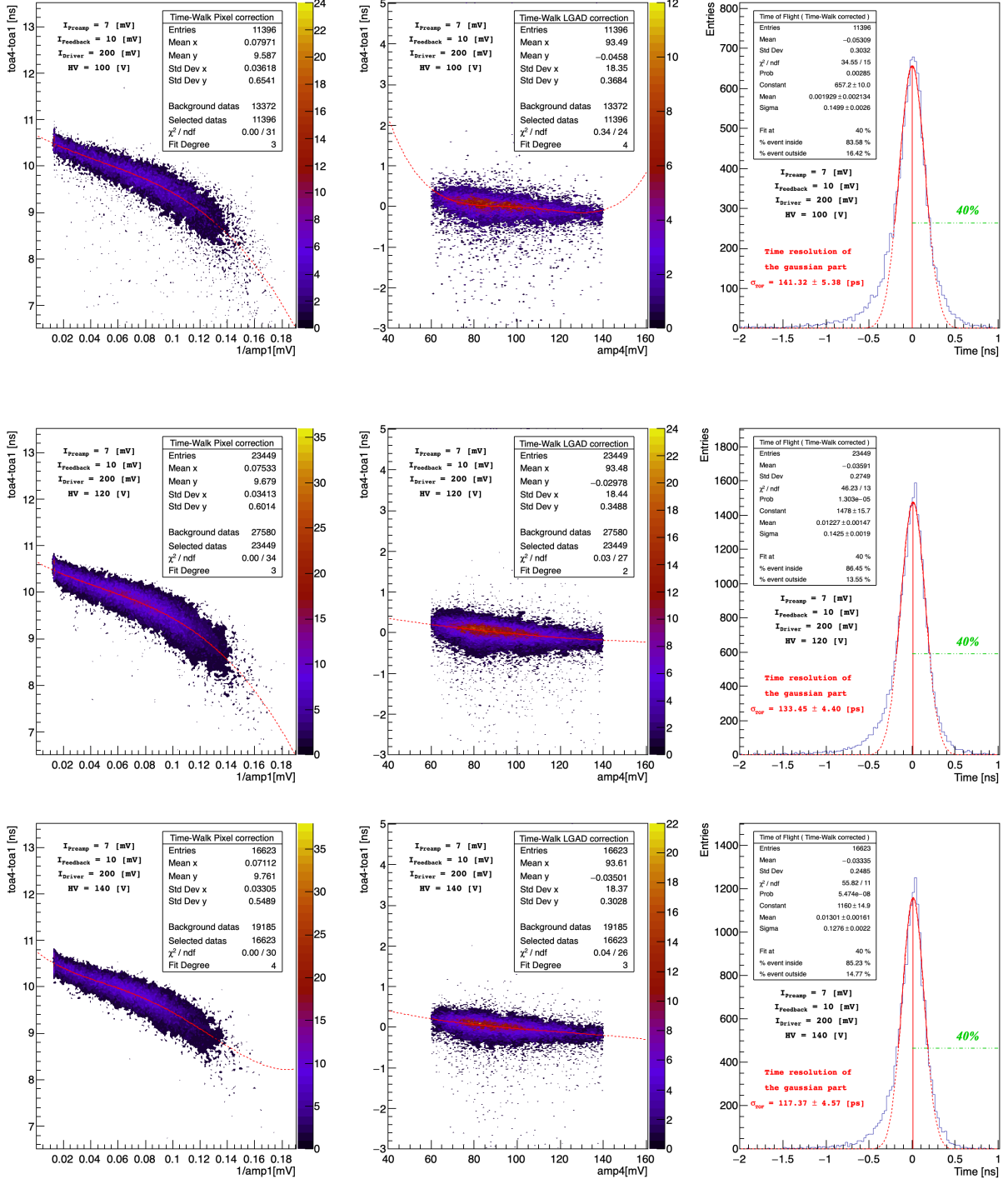
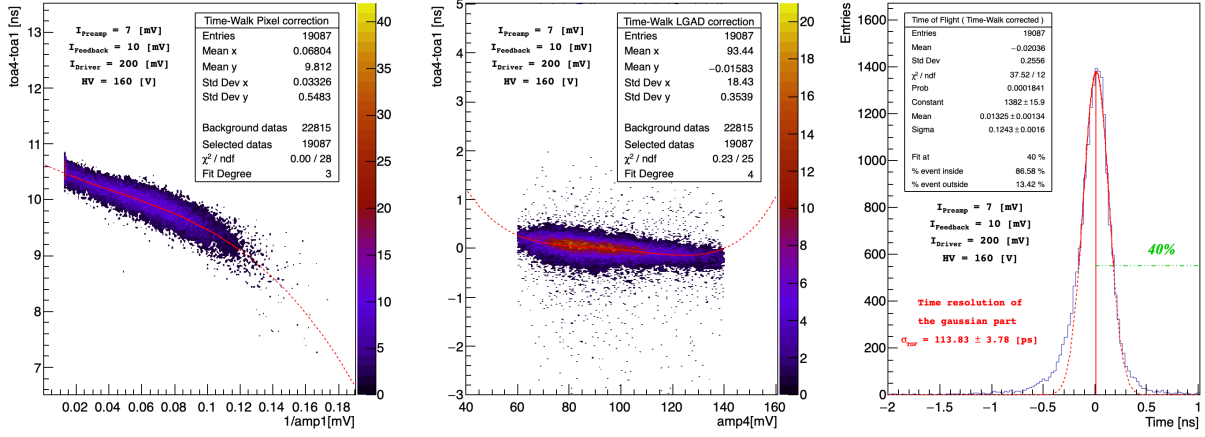


FIGURE 14.2 – Condition: Bias preamp = 100 DAC (Bias feedback : 10, 20 , 50, 100 and 200 DAC) Representations of events not selected using the condition of Equation 10.1.



14.2 TOF Results -  $I_{Preamp} = 7$  DAC



### 14.3 TOF Results - $I_{\text{Preamplifier}} = 150 \text{ DAC}$

